Summer 8-10-2023

Topological Hall Effect in Particulate Magnetic Nanostructure

Ahsan Ullah
University of Nebraska - Lincoln, aullah@huskers.unl.edu

TOPOLOGICAL HALL EFFECT IN PARTICULATE MAGNETIC NANOSTRUCTURE

by

Ahsan Ullah

A DISSERTATION

Presented to the Faculty of

The Graduate College at the University of Nebraska

In Partial Fulfillment of Requirements

For the Degree of Doctor of Philosophy

Major: Physics and Astronomy

Under the Supervision of Professor Xiaoshan Xu,

Lincoln, Nebraska

August, 2023

TOPOLOGICAL HALL EFFECT IN PARTICULATE MAGNETIC NANOSTRUCTURE

Ahsan Ullah, Ph.D.

University of Nebraska, 2023

Advisor: Xiaoshan Xu

Conduction electrons change their spin direction due to the exchange interaction with the lattice spins. Ideally, the spins of the conduction electrons follow the atomic spin adiabatically, so that spins like $\boldsymbol{S}_1$, $\boldsymbol{S}_2$, and $\boldsymbol{S}_3$ can be interpreted as time-ordered sequences $t_1 < t_2 < t_3$. Such spin sequences yield a quantum-mechanical phase factor in the wave function, $\psi \rightarrow e^{i\gamma}\psi$, where γ is known as the *Berry phase*. The corresponding spin rotation translates into a Berry curvature and an emergent magnetic field and subsequently, Hall-effect contribution known as the topological Hall-effect. This dissertation explores topological Hall-effect in particulate magnets, where noncollinear spins are stabilized by competition between different magnetic interactions. The topologically non-trivial spin textures in these nanostructures are flower states, curling states, vortex, and magnetic bubbles, which give rise to topological Hall-effect and have finite spin chirality and Skyrmion number *Q*. Topological Hall-effect is investigated in noninteracting nanoparticles, exchanges coupled centrosymmetric nanoparticles, exchanges coupled non-centrosymmetric nanoparticles which possess Dzyaloshinskii-Moriya interaction (DMI), and exchanged coupled Hard and soft magnetic films. Micromagnetic modeling, simulations, analytical calculations, and experimental methods are used to determine topological Hall-effect. In very small noninteracting nanoparticles,

the reverse magnetic fields enhance *Q* due to the flower state until the reversal occurs, whereas, for particles with a radius greater than coherence radius, the *Q* jumps to a larger value at the nucleation field representing the curling state. The comparisons of magnetization patterns between experimental and computed magnetic force microscopy (MFM) measurements show the presence of spin chirality. Magnetic and Hall-effect measurements identify topological Hall-effect in the exchange-coupled Co and CoSi-nanoparticle films. The origin of the topological Hall-effect namely, the chiral domains with domain-wall chirality quantified by an integer skyrmion number in Co and chiral spins with partial skyrmion number in CoSi. These spin structures are different from the Skyrmions due to DMI in B-20 crystals and multilayered thin films with C_{nv} symmetry. In these films THE caused by cooperative magnetization reversal in the exchange-coupled Co-nanoparticles and peripheral chiral spin textures in CoSi-nanoparticles.

Preface

The results presented in **Chapter 1** have been published in IEEE Transactions on Magnetics (**A. Ullah**, B. Balamurugan, W. Zhang, S. Valloppilly, X-Z Li, R. Pahari, L. Yue, A. Sokolov, D. J. Sellmyer, R. Skomski, IEEE Trans. Magn. **55**, 7100305 (2019)).

The results presented in **Chapter 3** have been submitted to Physics Rev. B. (**Ahsan Ullah**, Balamurugan Balasubramanian, Bibek Tiwari, Bharat Giri, David J. Sellmyer, Ralph Skomski and Xiaoshan Xu (Under Review in Physics Rev. B, Preprint: arXiv)) and published in AIP advances (**A. Ullah**, B. Balamurugan, W. Zhang, D. J. Sellmyer, and R. Skomsk, AIP Advances **9**, 125049 (2019)).

The results presented in **Chapter 4** have been published in Physics Rev. B. (**Ahsan Ullah**, Xin li, Yunlong Jin, R. Pahari, L. Yue, Xiaoshan Xu, B. Balasubramanian, David J. Sellmyer, and Ralph Skomski, Physical Review B **106**, 134430 (2022)) with a basic discussion and idea of the Topological Hall effect mentioned in Appl. Phys. Lett. (Wenyong Zhang, Balamurugan Balasubramanian, **Ahsan Ullah**, Rabindra Pahari, Xingzhong Li, Lanping Yue, Shah R. Valloppilly, Andrei Sokolov, Ralph Skomski, and David J. Sellmyer Appl. Phys. Lett. **115**, 172404 (2019)).

The results in **Chapter 5** have been published in Phys. Rev. Materials (R. Pahari, B. Balasubramanian, **A. Ullah**, P. Manchanda, H. Komuro, R. Streubel, P. Shafer, P. Dev, R. Skomski, and D. J. Sellmyer, Phys. Rev. Materials **5**, 124418 (2021)), JMMM. (X. H. Zhang, T. R. Gao, L. Fang, S. Fackler, J. A. Borchers, B. Kirby, B. B. Maranville, S. E. Lofland, A. Diaye, E. Arenholz, **A. Ullah**, J. Cui, R. Skomski, I. Takeuchi, J. Magn. Magn. Mater. 560, 169627 (2022)), and JMMM (W. Zhang, B. Balasubramanian, Y. Sun, **A. Ullah**, R. Skomski, R. Pahari, S. R. Valloppilly, X.-Zh. Li, C.-Zh. Wang, K.-M. Ho, and D. J. Sellmyer, J. Magn. Magn. Mater. 537, 168104 (2021)).

DEDICATION

To Ammy (My Mother) and Babu (My Father). Thanks for your unconditional and sincere love. May Allah always make everything easy for both of you.

ACKNOWLEDGMENTS

I am thankful beyond words to Allah almighty for this journey. I would also like to thank my parents for the sacrifices they have made, the biggest of which is the display of patience toward me and their support.

I would like to thank my advisor, Prof. Xiaoshan Xu, for his guidance, and support during my program especially after April 2022 when my previous Ph.D. advisers Prof. Ralph Skomski and Prof. David J. Sellmyer passed away. Prof. Xu managed everything very smoothly and calmly. We were able to finish the Ph.D. projects systematically from comprehensive exams, research projects, publications and finally writing this thesis. It was an honor to join his group and learn through discussions during meetings. He also provided me the opportunity to work in his lab for fabrication and encouraged me to experiment in a clean room.

I am thankful to my committee members: Prof. Abdelghani Laraoui, Prof. Alexey Kovalev, Prof. Sy-Hang Liou, and Prof. Zeng for their valuable advice and support during my Ph.D. and guidance related to the comprehensive exam and thesis. Discussion with Prof. Laraoui during the EQUATE workshop and many other events was very helpful, and he showed his full support since he joined my committee and in many different circumstances. I would like to thank Prof. Liou for his useful advice. My office is in front of his office and whenever I needed any advice I used to go to his office and discuss with him for his valuable advice. I would like to thank Prof. Kovalev, for his support by joining my committee and showing his generous support and kindness and thoughtful questions related to my research.

I would like to thank Late Prof. Ralph Skomski for advising me during my Ph.D. and helping me to gain confidence. His knowledge and tutoring carried me throughout the program. He taught me, creative and critical thinking, which will benefit me after graduation. Ralph was very supportive of me during my Ph.D. and I never had support like that. Sitting with him and talking about physics, social

issues, and other things were very insightful. I would also like to give my special thanks to Prof. David J. Sellmyer for his Guidance and encouragement during my Ph.D. His knowledge enabled me to imagine the experimental systems, which help me to computationally model the system to understand the physics involved. His professional attitude towards research, management, and enthusiasm for research was remarkable. Working with Prof. Sellmyer and Ralph was an honor for me. I would also like to thank Dr. Bala Balasubramanian who provided me lots of support both intellectually and emotionally throughout the program. I used to discuss everything with him during my Ph.D. He was like my adviser. I learned many experimental techniques from him and I learned how to act in professional life. I would say Bala is a very good addition to my life and will remain close to me as long as we are here.

I would also like to thank all the graduate students in my group, Bibek, Xin, Bharat, Detian, and Yuanyun. I benefit a lot from their presentations and our discussions all the time. I would like to thank all my colleagues in my previous group: Dr. Wenyong, Dr. Yunlong, Dr. Steve, Dr. Jim (TEM lab), Dr. Shah, Dr. Lanping, Dr. Rabindra, and Dr. Sokolov.

I would like to thank all my friends in Lincoln: John (My chess and Bike ride friends), My friend Kabosh Adam from IFOL, Mulana Hamza and Nizar from Bosnian Mosque, Salman and his roommate Hamdan, and friend from physics department: Mahmudul Hassan, Dr. Harin, Joaquin Siado (chess and bike ride friend).

Finally, grateful to my brother, sisters, and especially my nephews for their best wished. They are always my strongest supporters.

Table of Contents

Chapter 1 Introduction

The Nobel Prize in Physics was awarded for the study of the topological concept and topological phases associated with the electron band spectrum. The fascinating research in this field is usually described and explained by momentum space Berry curvature. The 2-dimensional topological phase in doped graphene, topological insulators, topological semimetals, and topological superconductors in 3d space are some examples where the fundamental concepts of topology are studied in condensed matter physics [1]. Recently the study of skyrmions in magnetic materials open a new direction for the study of topology in real space in condensed matter physics. Due to topological spin textures, the electronic spins traversing through the spin textures acquire the real space Berry phase and Berry curvature [2]. This chapter introduces the main principles of micromagnetism and its application for a description of the chiral spin texture, which gives rise to the real space Berry phase and emergent magnetic field. The fictitious magnetic field gives rise to an additional Hall effect known as the *topological Hall effect*. Study of real space Berry phase connects magnetism with real space topology in condensed matter physics. We will use micromagnets and transport properties to study these spin textures. Micromagnetic free energy which has different magnetic interactions is used to study the stabilization of magnetic spin textures.

1.1 Magnetic Interactions

In magnetic materials, magnetic interactions play an important role in stabilizing the spin texture, which is described by magnetization $\boldsymbol{M}(\mathbf{r})$ or spins $\boldsymbol{S}(\mathbf{r}) = \boldsymbol{M}(\mathbf{r})/|\boldsymbol{M}(\mathbf{r})|$. The spin textures interact with each other and with external factors in such a way that the total free energy achieves local or global minima at which the spin textures $\boldsymbol{M}(\mathbf{r})$ are

stable. The deviation from the local or global minima gives unique magnetic and transport properties. Magnetic free energy is the combination of different energies described below.

1.1.1 Exchange Interaction

In magnetic materials, the primary interaction between neighboring spin responsible for magnetic ordering is the exchange interaction. The exchange interaction between the spins of neighboring atoms is referred to as interatomic exchange [3, 4]. This exchange can be positive, favoring parallel spin alignment (ferromagnetism, FM), or negative (antiferromagnetism, AFM) giving minimum energy for antiparallel neighboring spins. The exchange interaction is usually given by the Hamiltonian formulated by Heisenberg [3]. If two atoms i and j have spin angular momentum Si and Sj , respectively, then the exchange interaction between them is given by:

$$\mathscr{H} = -\mathcal{J}\ \mathbf{S}_i \cdot \mathbf{S}_j. \tag{1}$$

Which describes the coupling between two neighboring spins $\mathbf{S}_i$ and $\mathbf{S}_j$. The vectors $\mathbf{S}_i$ are the spin angular momenta in units of Plank's constant. The value of the exchange integral due to Coulomb's interaction $\mathcal{J}$ strongly depends on interatomic distance. Its value is positive if exchange interaction tends to align spins parallel giving a ferromagnetic exchange, or negative if alignment is antiparallel giving an antiferromagnetic exchange. Usally the above for of exchange interaction Hamiltonian is used in atomic scale clculations. In atomistic scale the geometry specified by the type and position of each atom, along with a physical model for atomic interactions. The Heisenberg spin model uses the essential physics of a magnetic material at the atomic level with local spins

assign to each atom. These local spin magnetic moment are due to upaired electron at the atomic sites.

Since neighbouring spins are only allowed to vary by a small angle one can approximate: $\mathbf{S}_i = \mathbf{S}(\mathbf{r})$ and $\mathbf{S}_j = \mathbf{S}(\mathbf{r}_j) = \mathbf{S}(\mathbf{r}+\mathbf{dr}) = \mathbf{S}(\mathbf{r}) + \Delta\mathbf{r}\nabla_i\mathbf{S}(r_i)$. Where the atomic positions $r_j = j\Delta\mathbf{r}$ different distance vectors. So we canwrite:

$$\mathbf{S}_i \cdot \mathbf{S}_j = \mathbf{S}(\mathbf{r}).\ \mathbf{S}(\mathbf{r}+\mathbf{dr}) = 1 - \frac{1}{2}\left(\mathbf{S}(\mathbf{r}) - \mathbf{S}(\mathbf{r}+\mathbf{dr})\right)^2 \tag{1a}$$

$$\mathbf{S}_i \cdot \mathbf{S}_j = 1 - \frac{1}{2}\left(\Delta\mathbf{r}\nabla_i\mathbf{S}(r_i)\right)^2 \tag{1b}$$

The transformation from the discrete model to the continuum limit is described by integral instead of summation [5]. Extending this consideration to arbitrary spin directions in three dimensions yields the exchange energy [4],

$$\mathscr{E}_{ex} = \int A\,(\nabla \boldsymbol{M}/M_s)^2\,\mathrm{d}V \tag{2}$$

where the exchange stiffness $A(\boldsymbol{r})$ describes the interatomic exchange on a continuum level and includes the exchange integral and the magnitude of the spins involved. For a broad range of magnetic materials, A is of the order of 10 pJ/m for a broad range of ferro- and ferrimagnetic materials. The ∇ operator in Eq. (2) penalizes rapid changes in the magnetization directions, which are opposed by the exchange.

1.1.2 Anisotropy Energy

In a magnetic material, the energy depends on the direction of magnetization with respect to crystalline axes. This energy is called magnetic anisotropy. This energy is the origin for hysteresis and coercivity. The magnetic anisotropy is conveniently described by the magnetization angles θ and ϕ with respect to the crystal axes

$$\boldsymbol{M} = M_s\,(\sin\theta\cos\phi\,\boldsymbol{e}_x + \sin\theta\sin\phi\,\boldsymbol{e}_y + \cos\theta\,\boldsymbol{e}_z). \tag{3}$$

In most materials, $\theta = 0$ means the z- or crystallographic c-direction, whereas $\theta = 90^{o}$ and $\phi = 0$ refers to the x- or crystallographic a-axis. The origin of magnetic anisotropy is the spin-orbit interaction, whereas the orbit of an electron depends on the electric field in the crystal environment. The simplest and most widely used expression is second-order uniaxial anisotropy, described by the energy expression [4, 5],

$$\frac{E_a}{V} = K_1 \sin^2\theta \tag{4}$$

here K_1 is the first uniaxial anisotropy constant. Magnets with lowest-order uniaxial anisotropy, Eq. (4), may have easy-axis anisotropy ($K_1 > 0$) or easy-plane anisotropy ($K_1 < 0$). Easy-axis anisotropy implies energy minimum at $\theta = 0$ and $\theta = 180^{o}$. Easy plane magnetism corresponds to an energy minimum at $\theta = 90^{o}$. Equation (4) may also include higher-order terms that are not mentioned. For micromagnetics, the uniaxial anisotropy energy can also be written as [4,5]

$$\frac{E_a}{V} = -K_1 (\mathbf{n}.\mathbf{M})^2/M_s^2, \tag{5}$$

n is the unit vector along the preferential anisotropy axis. The total uniaxial anisotropy energy is the sum of the uniaxial energy of all spins and in the continuum, it is written as

$$\mathscr{E}_a = \int \left\{ - K_1 \frac{(\boldsymbol{n}.\boldsymbol{M})^2}{M_s^2} \right\} dV. \tag{5}$$

1.1.3 Zeeman Energy

Magnetic moments ***m*** interact with external magnetic fields ***H***, which is known as Zeeman interaction [4, 5],

$$\mathscr{E}_z = -\mu_o \boldsymbol{m}\cdot\boldsymbol{H} \tag{6}$$

where $\mu_o = 4\pi \times 10^{-7}$ J/A^{2}m is the vacuum permeability. The Zeeman interaction favors parallel alignment between moment and field as shown in Fig 1.1. In the micromagnetic continuum limit, the magnetic moment will be replaced by the magnetization vector in the whole volume.

$$\mathscr{E}_z = \int \{-\mu_o \boldsymbol{M}.\boldsymbol{H}\}\, dV \tag{7}$$

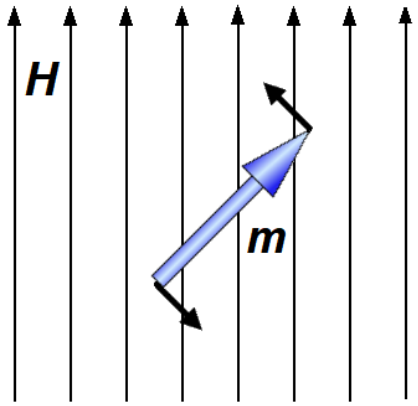

Figure 1.1 Magnetic moment: (a) Zeeman interaction $-\mu_o \boldsymbol{m}\cdot\boldsymbol{H}$ with an external magnetic field.

1.1.4 Magnetostatic self-interaction

Magnetostatic interaction between magnetic moments is based on dipolar interaction energy. The magnetostatic self-interaction field $\boldsymbol{H}_d$ at position $(\boldsymbol{r}-\boldsymbol{r}')$ can be computed using [4, 5],

$$\boldsymbol{H}_d(\boldsymbol{r}) = \frac{1}{4\pi}\int \frac{3(\boldsymbol{r}-\boldsymbol{r}')\,(\boldsymbol{r}-\boldsymbol{r}')\cdot\boldsymbol{M}(\boldsymbol{r}') - |\boldsymbol{r}-\boldsymbol{r}'|^2\boldsymbol{M}(\boldsymbol{r}')}{|\boldsymbol{r}-\boldsymbol{r}'|^5}\, dV'. \tag{8}$$

In an ellipsoid with homogenous magnetization along the symmetry axis, the self-interaction field is equal to demagnetizing field $\boldsymbol{H}_d = -D\boldsymbol{M}$. The magnetostatic self-interaction energy is given by

$$\mathscr{E}_{\mathrm{d}} = \int \left\{ -\frac{\mu_{\mathrm{o}}}{2} \boldsymbol{M}.\boldsymbol{H}_{\mathrm{d}}(\boldsymbol{M}) \right\} \mathrm{d}V. \tag{9}$$

For complicated magnets we can use $(3\boldsymbol{rr} - r^2)/r^5 = -\boldsymbol{\nabla}(\mathbf{r}/r^3)$ and $\boldsymbol{\nabla}.(a\mathbf{b}) = a\,\boldsymbol{\nabla}.\,\mathbf{b} + \boldsymbol{\nabla}a.\,\mathbf{b}$. It enables us to write eq. 8 in terms of magnetic charge density $\rho_{\mathrm{M}} = -\boldsymbol{\nabla}\bullet\mathbf{M}$. The self-interaction then assumes the form [4, 5],

$$\boldsymbol{E}_{\mathrm{ms}} = \frac{\mu_{\mathrm{o}}}{4\pi} \int \frac{\rho_{\mathrm{M}}(\mathbf{r})\, \rho_{\mathrm{M}}(\mathbf{r}')}{|\boldsymbol{r} - \boldsymbol{r}'|^5}\ \mathrm{d}V'. \tag{10}$$

Since most magnets are structurally inhomogeneous, so that $\boldsymbol{\nabla}\bullet\mathbf{M} \neq 0$ inside the magnet. This leads to relatively high energy, which can be reduced by domain wall formation. Magnetic charge at the surface also leads to relatively high magnetostatic energy. Domain formation and flux closure are very good sources to reduce this energy.

`The concept of the demagnetization field can be understood by the study of the B-field inside the magnet. The B-field and magnetic field strength are related through magnetization [5]

$$\boldsymbol{B} = \mu_{\mathrm{o}}(\boldsymbol{H} + \boldsymbol{M}). \tag{11}$$

Since the absence of magnetic monopole $\boldsymbol{\nabla}\bullet\boldsymbol{B} = 0$ gives us:

$$\boldsymbol{\nabla}.\,\boldsymbol{H} = -\boldsymbol{\nabla}\bullet\boldsymbol{M}. \tag{12}$$

Using Eq. (12) we can say that $\boldsymbol{H}$, like the electric field $\boldsymbol{E}$, arises due to the distribution of positive and negative magnetic charge ρ_{M}. To realize the demagnetization field due to the distribution of the magnetic change the boundary condition associated with B-field can be used $\boldsymbol{B}_{\perp} = \mu_{\mathrm{o}}(\boldsymbol{H} + \boldsymbol{M})$ inside and $\boldsymbol{B}_{\perp} = \mu_{\mathrm{o}}(\boldsymbol{H})$ outside. Now in the absence of an external field, we have $\boldsymbol{H}_{\mathrm{D}} = -\boldsymbol{M}$ for slabs magnetized along the out-of-plane direction, indicating the demagnetization field is opposite to the magnetization. In magnetic

materials of general shapes, the demagnetization is some fraction of magnetization i.e., $\boldsymbol{H}_D = -\mathrm{D}\boldsymbol{M}$, and in the presence of an external field the H-field is

$$\boldsymbol{H} = \boldsymbol{H}_{\text{applied}} - \mathrm{D}\boldsymbol{M}. \tag{13}$$

1.1.5 Dzyaloshinskii Moriya Interaction

The antisymmetric exchange interaction Dzyaloshinskii Moriya interaction (DMI) is given by [7, 9]

$$H_{\text{dm}} = -\boldsymbol{D}\bullet(\boldsymbol{S}_i \times \boldsymbol{S}_j). \tag{14}$$

This interaction favors the spin orthogonal to each other and in the direction of DMI vector $\boldsymbol{D}$ and produces a small magnetic moment perpendicular to the antiferromagnetic axis. The vector $\boldsymbol{D}$ must lie along the high symmetry axis [9]. Therefore, for hexagonal, rhombohedral, and tetragonal unit cells $\boldsymbol{D}$ lies along the c-axis [8]. Moriya derived the above equation by introducing SOI [9] as perturbation into Anderson's magnetic superexchange [9]. In magnetic oxides, DMI can also be defined as the perturbation in spin-orbit coupling due to the crystal field. The electrons on cation sites without inversion symmetry try to minimize the crystal field energy by slightly making a noncollinear spin texture and giving rise to finite SOI [4].

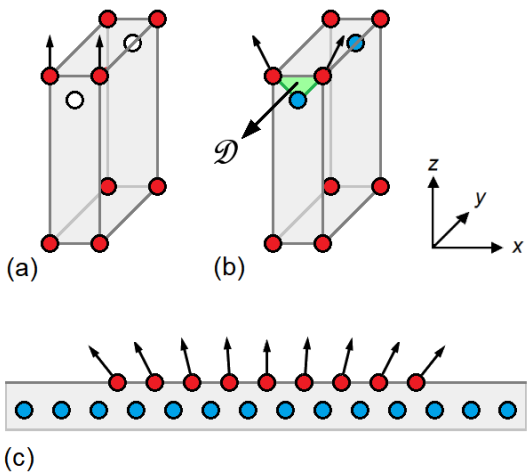

Figure 1.2. Dzyaloshinski-Moriya Interactions in (a-b) orthorhombic crystals and (c) thin films interfacial DMI. The red atoms are magnetic, whereas the blue and white atoms are nonmagnetic but have weak (white) and strong (blue) spin-orbit coupling.

1.1.6 Energy functional

The micromagnetic energy contains all contributions discussed in section 1.1.1 to 1.1.5. An often-considered micromagnetic energy functional is [3,4,10,11,12,13],

$$\mathscr{E} = \int \left\{ A\left[\nabla\left(\frac{\boldsymbol{M}}{M_s}\right)\right]^2 - K_1 \frac{(\boldsymbol{n}.\boldsymbol{M})^2}{M_s^2} - \mu_o \boldsymbol{M}.\boldsymbol{H} - \frac{\mu_o}{2}\boldsymbol{M}.\boldsymbol{H}_d(\boldsymbol{M}) \right\} dV \qquad (15)$$

where A is the exchange stiffness, $K_1(\boldsymbol{r})$ denotes the first uniaxial anisotropy constant, and $\boldsymbol{n}(\boldsymbol{r})$ is the unit vector of the local anisotropy direction.

1.2 Berry Phase in Magnetic Materials

In modern solid-state quantum mechanics, the wave functions carry a phase factor, $\psi(\boldsymbol{r}) \rightarrow \exp(i\gamma)\psi(\boldsymbol{r})$, which γ is known as the *Berry phase* [14]. This phase is negligible in many cases because the quantum-mechanical probability $\psi^* e^{-i\gamma} e^{i\gamma} \psi = \psi^* \psi$ does not depend on it γ. One example is the topological Hall effect caused by conduction electrons interacting with skyrmions. Due to interatomic exchange, the spin direction of the conduction electrons follows the local spin $\boldsymbol{S}(\boldsymbol{r})$. As we will see below, the

corresponding noncoplanar rotation of the conduction electrons translates into a quantized contribution to the Hall effect.

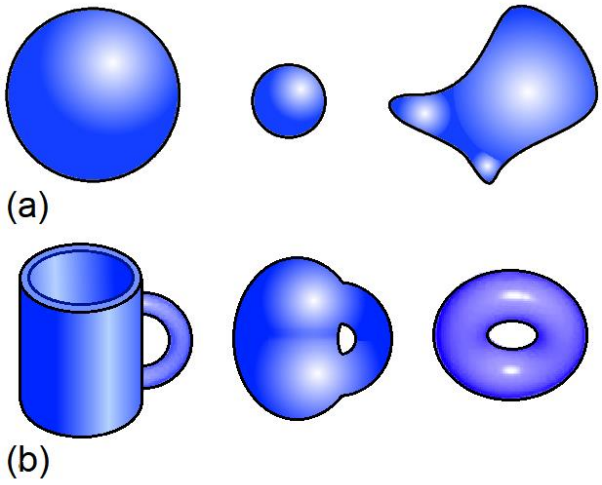

Figure 1.3. Topological protection in geometry. The three bodies in (a) are topologically equivalent, because they can continuously be transformed into each other, and the same is true for (b). In three dimensions (a-b), the topology is quantified by a surface integral over the Gaussian curvature (Gauss-Bonnet theorem), whereas the two-dimensional analog is a Fenchel-type line integral.

Figure 1.3 illustrates the idea of topology and topological protection. According to the Gauss-Bonnet theorem, the surface integral $\oint \boldsymbol{\kappa} . \mathrm{d}\boldsymbol{\mathcal{A}}$ over the Gaussian curvature $\kappa = 1/R_1R_2$ of a body without holes is equal to 4π (a). The integral does not depend on the shape or size of the body, so long as no holes are created during deformation. A trivial example is the sphere, where $\kappa = 1/R^2$ and $\oint \mathrm{d}\mathcal{A} = 4\pi$. When the particle has N holes, then Euler's formula must be used, $\int \kappa \, \mathrm{d}\mathcal{A} = 4\pi(1 - N)$, as exemplified by $N = 1$ (b). So if we get 4π, we live on a sphere, if we get 0, we live on a torus. This is an example of *topological protection*: the system with $N = 1$. The same considerations apply to two-dimensional objects, Fig. 1.3(c), except that $\kappa = 1/R$ and the Gauss-Bonnet theorem must be replaced by Fenchel's theorem, $\oint \kappa \, \mathrm{d}r = 2\pi$ [15].

1.2.1 Relation to magnetism

The following example illustrates the relationship between topology and spin structure. Consider three normalized spins $\boldsymbol{S}_1$, $\boldsymbol{S}_2$, and $\boldsymbol{S}_3$ and the triple product or ' spin chirality' [16, 17]

$$\chi_c = \boldsymbol{S}_1 \cdot (\boldsymbol{S}_2 \times \boldsymbol{S}_3). \tag{16}$$

Figure 1.4(a) shows this spin configuration as vectors normal to the surface of a fictitious magnetic particle. The triple product is proportional to the Gaussian curvature κ. When the surface is flat, then all spins are parallel, and $\chi_c = 0$.

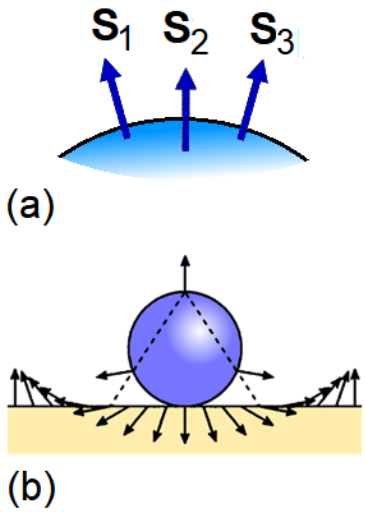

Figure 1.4. Relation between Gaussian curvature and magnetism: (a) three spins normally to an arbitrary surface and (b) projection onto a thin-film plane. The projection conserves the topology.

The example of a nanoparticle having all spins perpendicular to the surface is somewhat academic and not very relevant experimentally. However, due to topological protection, the spin structure can be almost arbitrarily deformed to match the real physical situation. Figure 1.4(b) illustrates this point for a Néel skyrmion created from a sphere with perpendicular surface magnetization. Such thin-film structures, known as

magnetic skyrmions, have been investigated intensively in recent years [2]. Skyrmions are named after Tony Skyrme, who found such structures as solutions of nonlinear field equations in elementary-particle physics [18, 19]. The concept is closely related to and partly overlaps with phenomena such as vortices, curling, and bubbles.

1.2.2 Magnetotransport in metallic magnetic nanostructures

Conduction electrons traveling through magnetic nanostructures exchange-interact with atomic spins. Ideally, the spins of the conduction electrons follow the atomic spin adiabatically, so that $\boldsymbol{S}_1$, $\boldsymbol{S}_2$, and $\boldsymbol{S}_3$ can be interpreted as time-ordered sequences $t_1 < t_2 < t_3$. As recognized by Berry in 1984, such spin sequences yield a quantum-mechanical phase factor in the wave function, $\psi \rightarrow e^{i\gamma} \psi$, which γ is known as the *Berry phase*. The change in the spin direction can be visualized as the rotation of a unit vector on a Bloch sphere, Fig. 1.5, and the Berry phase is given by the solid angle Ω enclosed by the spin rotation [14, 20]. In analogy to the Gaussian curvature, the solid angle can also be defined through integration over a curvature known as *Berry curvature*.

Physically, the Berry curvature acts as a magnetic $\boldsymbol{B}$ field adding to the external magnetic field and is referred to as an *emergent magnetic field*. In more detail, $\boldsymbol{B} = \nabla \times \boldsymbol{A}$, where the vector potential $\boldsymbol{A}$ has the character of a Berry connection $\gamma = \int \boldsymbol{A} \cdot d\boldsymbol{r}$, or in differential form $\boldsymbol{A} = \nabla\gamma$. The emergent magnetic field affects the transport of carriers (electrons or holes) and contributes, for example, to the anomalous Hall effect [20]. This contribution is commonly referred to as the *topological Hall effect* (THE).

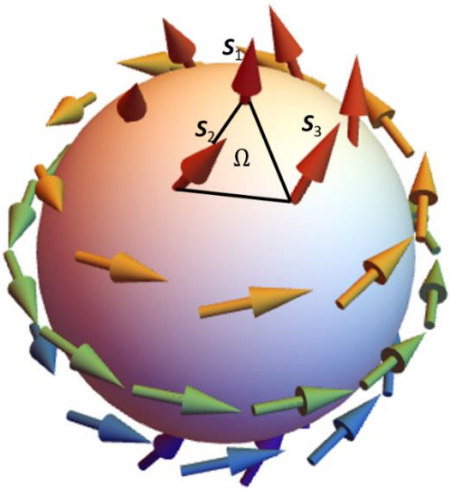

Figure 1.5. Berry phase and spin structure. The rotation of a spin on a closed path on a unit sphere creates a Berry phase that is proportional to the solid angle Ω encircled by the path. In transport measurements, the spin rotation of conduction electrons yields a contribution to the Hall effect. The rotation is realized by the adiabatic exchange interaction with noncoplanar atomic spins.

There is a simple way to rationalize that the Berry phase of the conduction electrons is equivalent to a magnetic vector potential $\boldsymbol{A} \sim \nabla\gamma$ and therefore to a magnetic field $\boldsymbol{B} = \nabla \times \boldsymbol{A}$. From basic electromagnetism, it is known that the vector potential $\boldsymbol{A}$ modifies the motion of the electrons via $\boldsymbol{p} \rightarrow \boldsymbol{p} + e\boldsymbol{A}$. The kinetic-energy operator of the electrons, $p^2/2m \sim \nabla^2$, does not contain γ and cannot, therefore, explain the emergent magnetic field. However, ∇^2 does not act on $\psi(\boldsymbol{r})$ but on $e^{i\gamma(\boldsymbol{r})}\psi(\boldsymbol{r})$, which leads to [21]

$$\nabla^2(e^{i\gamma}\psi) = e^{i\gamma}(\nabla + i\nabla\gamma)^2\psi \qquad (17)$$

The equation shows that the Berry connection (left-hand side) is equivalent to a magnetic vector potential (right-hand side).

1.2.3 Hall Experiments in Thin Films

Consider a thin film in the *x*-*y*-plane, a current I in the x-direction, and an external magnetic field $\boldsymbol{H}$ in the z-direction. The magnetic field creates a Hall voltage $U = R_{xy} I$ in the *y*-direction. The Hall resistivity ρ_{xy} is normally written as [2]

$$\rho_{xy} = R_0 H + R_s M + \rho_{THE}, \tag{18}$$

where R_0 is the coefficient of the ordinary Hall effect, R_s describes the anomalous Hall effect due to spin-orbit coupling, and ρ_{THE} is the topological Hall effect. Experimentally, it is common to treat R_0 and R_s as fitting parameters reproducing $\rho_{xy} = R_0 H + R_s M$ in high fields, where all spins are parallel and the THE is zero. Plotting $\rho_{xy} - R_0 H - R_s M$ then yields a positive or negative bump $\rho_{THE}(H)$ in low to moderate fields H [2]. The ordinary Hall effect reflects the Lorentz force acting on the electrons and is therefore proportional to the field. Traditionally the Topological Hall effect was named for the Hall effect due to skyrmions which has finite topology but the chiral sptexture with finite spin chirality $\chi_c = \boldsymbol{S}_1 \cdot (\boldsymbol{S}_2 \times \boldsymbol{S}_3)$ also gives rise to addition Hall effect and named as Topological Hall effect as mentioned in Ref. [16, 17]. The topological Hall effect due to spin chirality or incomplete skyrmion or partial skyrmion number is no quantized and need different description.

1.2.4 The Magnitude of the Topological Hall Effect

The THE is proportional to the triple product of Eq. (16) by spin chirality χ_c. A continuum version of this equation is the *skyrmion density*

$$\Phi = \frac{1}{4\pi} \boldsymbol{S} \cdot \left(\frac{\partial \boldsymbol{S}}{\partial x} \times \frac{\partial \boldsymbol{S}}{\partial y} \right). \tag{19}$$

This density is proportional to the emergent field component perpendicular to the *x*-*y* plane (normal to the film), which determines ρ_{THE} in thin films [2]. The total magnetic flux is equal to $\int B_{\mathrm{e}}\, \mathrm{d}x\, \mathrm{d}y = \mathrm{Q}\, h/e$, where h/e is the magnetic flux quantum and Q is the skyrmion number

$$Q = \int \Phi \, \mathrm{d}x\, \mathrm{d}y = \frac{1}{4\pi} \int \boldsymbol{S} \cdot \left(\frac{\partial \boldsymbol{S}}{\partial x} \times \frac{\partial \boldsymbol{S}}{\partial y} \right) \mathrm{d}x\, \mathrm{d}y \tag{20}$$

And B_{e} is the emergent magnetic field represented in terms of skyrmion density $\hbar/e\Phi$. It is well-known that fully developed skyrmions, such as that in Fig. 1.4 (b), have $Q = \pm 1$, depending on whether the magnetization in the core is up (+) or down (–).

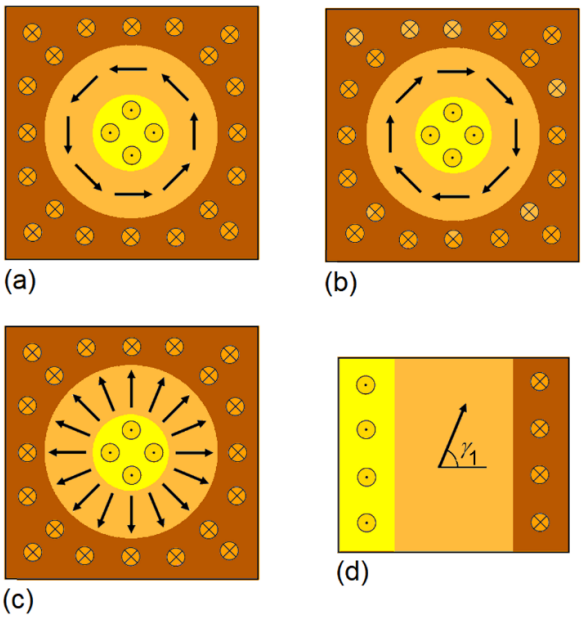

Figure 1.6. Protection of the topological Hall effect with respect to the domain-wall structure. Bloch walls of different chirality (a-b), Néel walls (c), and walls with arbitrary spin angles γ_1 yield the same THE.

Figure 1.6 shows top views on the film plane, and the yellow and brown regions show spin-up (↑) and spin-down (↓) magnetizations, respectively. Inside homogeneously magnetized regions, the triple product and therefore Φ is zero. This means that the THE

is determined by the skyrmion density Φ near the domain walls. The three configurations of Fig. 1.6(a-c) all have $Q = 1$, irrespective of whether the domain walls are of the counter-clockwise Bloch type (a), clockwise Bloch type (b), or Néel type (c). In fact, by analyzing the symmetry of Eq. (17), one can show that arbitrary magnetization angles γ_1 in the wall yield $Q = 1$. This angular independence is a particularly intriguing aspect of the topological protection of skyrmions.

Similar to Fig. 1.3 (c), domains can be distorted, enlarged, and shrunk without changing Q and the THE. Figure 1.7 shows some typical examples. The Fenchel curvature integral along any closed domain wall yields $Q = +1$ when the region inside the wall is ↑ (yellow) and $Q = -1$ when the region inside the wall is ↓ (brown). Both bigger and smaller domains yield the same THE contribution, corresponding to one flux quantum. Fig. 1.7(a, b, d-f), which makes it easy to judge the THE contributions of domain structures. Distortions from (a) to (b) and (d) may be realized experimentally [22, 23], which will be shown in Chapter 4.

Geometrical distortions and size changes do not change the THE per domain or "skyrmion". The domain structure of Fig. 1.7(h), also referred to as *skyrmionium*. Its skyrmion number $Q = 0$, which may be rationalized in as a superposition of an inner domain wall having $Q = -1$, as in Fig. 1.7(c), and an outer domain wall having $Q = + 1$. Superficially, Figs. 1.7(h) and (j) look similar, but their THE contributions (Q) are very different. The ring (h) is not protected against a cut transforming it into the configuration (j), because (j) is topologically equivalent to (a, b, d-f) and therefore has $Q = 1$. In terms of Eq. (20), the cut creates small but sharp regions of high domain-wall curvature, and the corresponding derivatives $\partial/\partial x$ and $\partial/\partial y$ realize the change from $Q = 0$ to $Q = 1$.

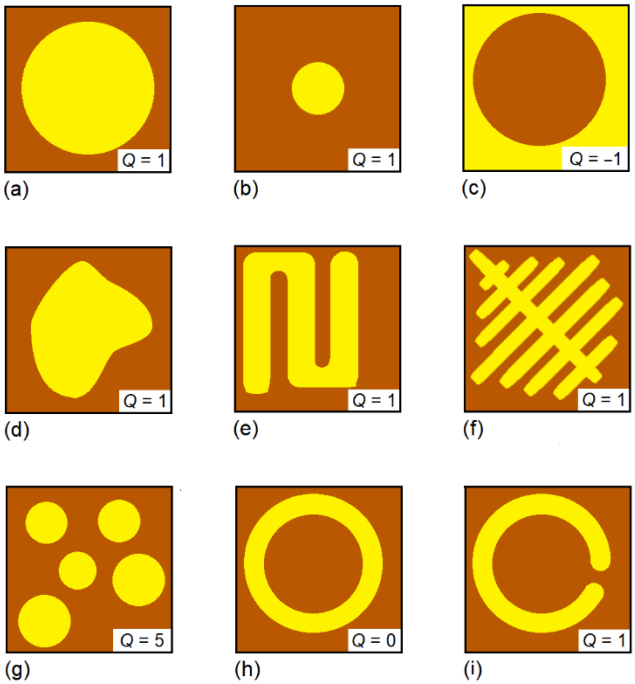

Figure 1.7. Skyrmion numbers Q for different thin-film spin structures (yellow = ↑, brown = ↓). The configurations (a, b, d-e, and i) can be continuously transformed into each other and are therefore topologically equivalent, all having $Q = 1$. The configurations (c, g, and h) are discussed in the main text.

1.3 Particulate Magnetic Nanostructures

In this thesis, the main emphasis is on the Berry-phase effects of particulate magnetic nanostructures. Nanoclusters and small nanoparticles exhibit a strong size-dependent modification in electronic structure due to confinement and surface effects. These structures often show entirely different magnetic properties as compared to corresponding bulk materials and traditional thin films due to the inhomogeneity of magnetizations. The nanoscale effects in particulate magnetic nanostructure play a crucial role in the electron-transport properties [27]. The particulate materials are made from magnetic nanoparticles and clusters.

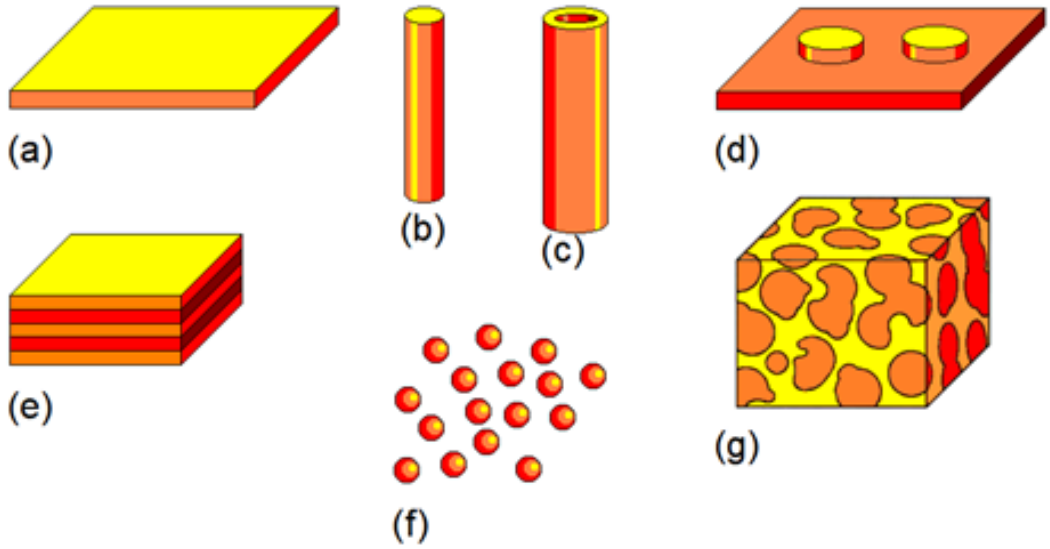

Figure 1.8. Typical nanoscale geometries: (a) thin film, (b) nanowire, (c) nanotube, (d) nanodots, (e) multilayers, (f) nanoparticles, (g) granular composites.

1.3.1 Nanoparticles and Nanodots

Examples of particulate magnetic materials are magnetic nanodots and non-interacting magnetic nanoparticles. These are small pieces of bulk material and the key feature of nanoparticles is their single-domain characters [24]. The magnetic properties of nanoparticles predominantly depend on the intrinsic properties of magnetic materials like anisotropy, exchange interaction, and saturation magnetization. The magnetic properties can often be described by continuum theory, for example by assuming a radial dependence $\boldsymbol{M}(\boldsymbol{r})$ of the magnetization. The transition from a single domain to a multidomain gets apparent through the study of the coercive field. Even within a single domain state the coercive field change because of the different states as the size increase as shown in Fig. 1.9 [24].

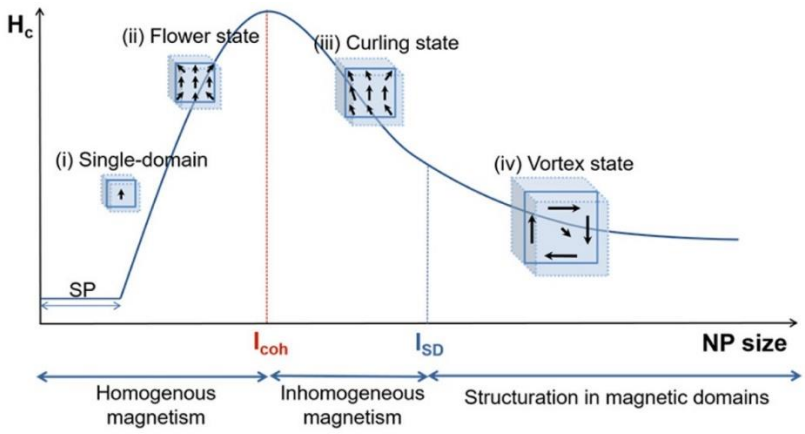

Figure 1.9. Sketch of the dependence of the magnetization hysteresis loop coercive field (H_c) with the nano-particle (NP) size (l). SP stands for superparamagnetic. Insets: The most energetically favored states of cubic nanoparticles with uniaxial anisotropy. The figure is taken from reference [24].

1.3.2 Magnetic Nanoclusters film

The difference between clusters and nanoparticles is that clusters are combinations of nanoparticles. They are fabricated by densely packed nanoparticle assemblies. The particles are interacting and the magnetic properties are widely affected by the exchange interaction between nanoparticles which are in contact with each other. As compared to the grain of bulk materials, the spin texture in magnetic nanoclusters films is modified significantly due to the large surface-to-volume ratio and confinement. The nanoparticles in nanoclusters easily align in the direction of the externally applied field which results in high remnant magnetization. One advantage of magnetic nanocluster is that it shows significant magnetization in a wide temperature range and exists in a broad composition range. These nanoclusters can be fabricated without the use of high-temperature melting giving unique control over phase purity and crystal order. Typical example of nanocluster film is shown in Figure 1.10.

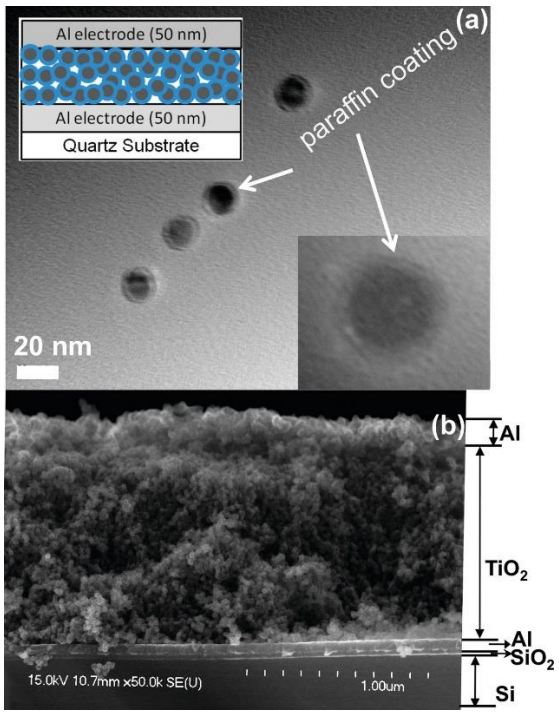

Figure 1.10. (a) A typical TEM image showing the TiO_2 paraffin core-shell nanoparticles prepared, where a single core-shell nanoparticle recorded at higher magnification is shown in the lower inset. (b) Cross-sectional FESEM image, consisting of a TiO_2 nanoparticle films deposited on aluminum electrodes, fabricated on a thin SiO_2-covered Si substrate. The figure is taken from reference [25].

1.4 Ferromagnetism in Particulate Magnetic Nanostructures

In a ferromagnetic material, spontaneous magnetization exists after the removal of the applied external field. In these materials spins within the grains not only align parallel to each other but also parallel to the spins in neighboring grains which gives rise to finite net magnetization. Understanding the magnetization prosses in the small magnetic nanoparticle is important to understand the ferromagnetism related to single domains in nanoparticles and for the magnetism in nanoclusters. The Stoner-Wohlfarth model gives good intuition for the understanding of magnetization and magnetic hysteresis.

1.4.1 Stoner-Wohlfarth Model

Stoner-Wohlfarth model is the simple model used to analyze the magnetic hysteresis of ferromagnetic material with uniaxial anisotropy. This model is very simple and is also called the *coherent rotation model*. This model assumes strong exchange interaction between the spins of atoms in ferromagnetic material giving rise to constant magnetization in particles. As a result, the energy of the particle is equal to anisotropy and externally applied field. For magnets of spherical shape, the micromagnetic energy per unit volume is the sum of anisotropy and Zeeman energies:

$$\frac{E}{V} = K_1 \sin^2\theta - \mu_o M_s H \cos(\theta - \alpha). \tag{22}$$

In zero field, the energy has two minima, at $\theta = 0$ (↑) and $\theta = \pi$ (↓). Since the exchange interaction dominates the nanoparticle acts as a small magnet with a magnetic moment align in the direction of anisotropy. Here θ is the angle between magnetization $\boldsymbol{M}$ and the easy axis and α the angle between the applied field and the easy axis. Fig. 1.11(a) shows the schematic of single-domain particles in the external field. The magnetization makes an angle with an easy axis decreasing the component of magnetization along the easy axis as shown in Fig. 1.11(b) for different finite field angles i.e. $M_e(\theta) = M_e(\theta = 0)\cos\theta$. However, when the field is aligned to the direction of the easy axis the hysteresis shows a perfect square. This is very important as in most cases the magnetization reversal is studied with a field applied along the direction of the easy axis. Stoner-Wohlfarth particle act as a small magnet and even a small field align them in a specific direction. The reversal field for Stoner- Wolfratth particles is determined by energy minimization:

$$H_N = \frac{2K_1}{\mu_o M_s}. \tag{23}$$

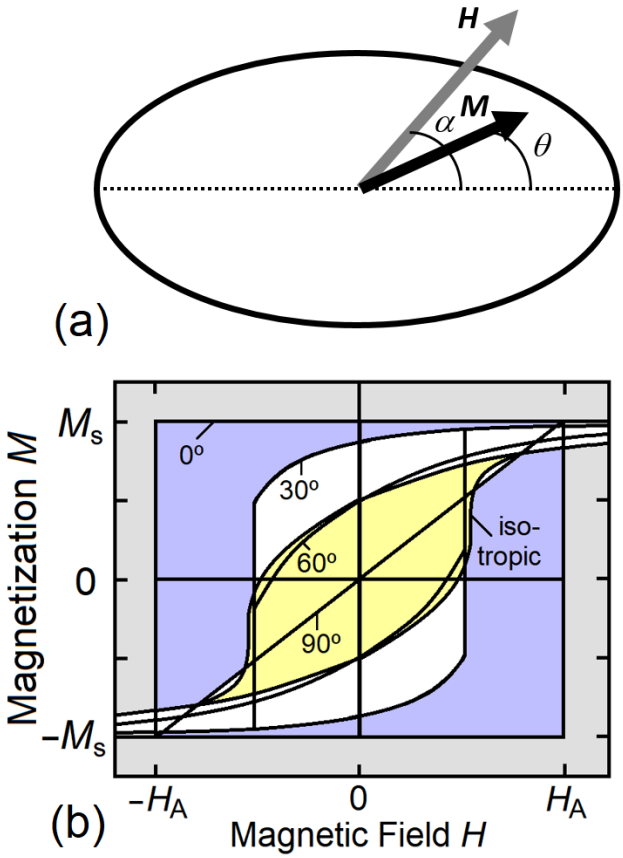

Figure 1.11 (a) Single domain Stoner-Wohlfrath particle in an external field. (b) Magnetization reversal for Stoner-Whlofrath particle. Note that the square loop is when the field is applied parallel to the easy axis and when the field is applied in a different direction.

1.4.2 Magnetization in Moderately Large Particles

The Stoner-Wohlfarth model assumes uniform magnetization throughout the magnet. In reality, interatomic exchange (A) favors magnetization uniformity but competes against other energy contributions, such as magnetostatic energies. As the size of particles increases, the particle still follows Stoner-Wohlfarth criteria but due to an increase in the size of the particle, the magnetostatic self-interaction plays a significant role in the magnetization measurement. As shown in Fig. 1.9 different magnetic spin states exist in nanoparticles and nanodots.

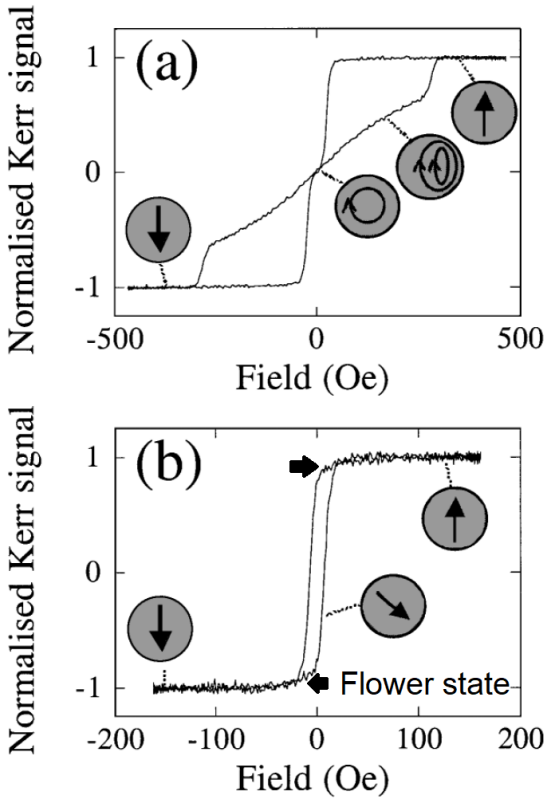

Figure 1.12 Hysteresis loops measured from nanomagnets of diameter *d* and thickness *t*: (a) *d* = 300nm, *t* = 10 nm; (b) *d* = 100 nm, *t* = 10 nm. The schematic annotation shows the magnetization within a circular nanomagnet, and arrows show the presence of flower states. The figure is taken from reference [26].

For larger nanoparticles, three states exist. (i) flower state (ii) curling state (iii) vortex state as shown in Fig. 1.9 [24]. The states appear at the nucleation field and tend to decrease the magnetization. As shown in Fig 1.12 the magnetization at the nucleation is some fraction of saturated magnetization. For the flower state, the decrease in magnetization is small while for curling mode the decrease in magnetization is significantly larger. These states will be discussed in detail in Chapter 3.

1.4.3 Magnetization in Nanoparticle/Nanocluster Films

The Nanoparticle/Nanocluster Films made in our lab which are shown in Fig 1.10 and with schematic in Fig. 1.13 are made of small nanoparticles of size in the range of 8

nm to 20 nm. These small nanoparticles or nanoclusters act like grains and can be treated as Stoner-Wholfarth grains. This system is not completely ideal i.e. Stoner-Wohlfarth model for a thin film of grains treats them as noninteracting [see Stoner-Wohlfarth model for noninteracting grains Fig 7 in 5] while in reality, the particles do interact with each other via exchange interactions which give rise to cooperative magnetization reversal. For an ideal stoner-Wholfarth model of non-interacting nanoparticles, the reversal will be cooperative.

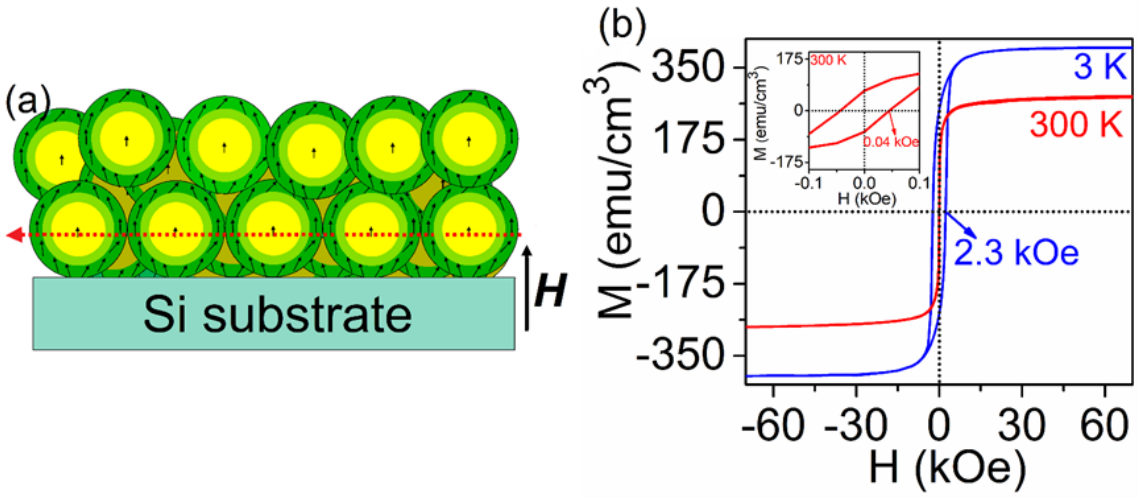

Figure 1.13 (a) Co_2Si nanoclusters: Schematic of a deposited thin film (b) Magnetic properties: (a) Field-dependent magnetization curves measured at 300 K and 3 K, where the inset shows the expanded room-temperature hysteresis loop in the low-field region. The figure is taken from reference [27].

References

[1]Joel E. Moore, " The birth of topological insulators" Nature volume **464**, 194 (2010).

[2] Sh. Seki and M. Mochizuki, "Skyrmions in Magnetic Materials", Springer International, Cham (2016).

[3] R. Skomski, "Nanomagnetics", J. Phys.: Condens. Matter **15**, R841-896 (2003).

[4] R. Skomski, *Simple Models of Magnetism*, Oxford: University Press, (2008).

[5] J. M. D. Coey, "Magnetism and Magnetic Materials" (Cambridge University Press, New York, (2010).

[6] A. A. Thiele, Bell Syst. Tech. J. **48**, 3287 (1969).

[7] I. Dzyaloshinskii, *J. Phys. Chem. Solids* **4**, 241 (1958).

[8] R. Skomski and J. M. D. Coey, *Permanent Magnetism*, Institute of Physics, Bristol (1999).

[9] T. Moriya, *Phys. Rev.* **120**, 91 (1960).

[10] William Fuller Brown, (Jr.) New York, London J. Wiley, (1963).

[11] A. Aharoni, *Introduction to the Theory of Ferromagnetism*, University Press, Oxford (1996).

[12] L. D. Landau and E. M. Lifshitz, On the theory of the dispersion of magnetic permeability in ferromagnetic bodies, Phys. Zs. Sowjet. 8, 153 (1935) [Reproduced in Ukr. J. Phys. 53 Special Issue, 14 (2008)].

[13] E. H. Frei, S. Shtrikman, and D. Treves Phys. Rev. **106**, 446 (1957).

[14] M. V. Berry, "Quantal phase factors accompanying adiabatic changes", Proc. R. Soc. Lond. A **392**, 45-57 (1984).

[15] W. Fenchel, "Über Krümmung and Windung geschlossner Raumkurven", Math. Ann. **101**, 238-252 (1929).

[16] Y. Taguchi, Y. Oohara, H. Yoshizawa, N. Nagaosa, and Y. Tokura, Science **291**, 2573 (2001).

[17] W. Wang, M. W. Daniels, Z. Liao, Y. Zhao, J. Wang, G. Koster, G. Rijnders, C.-Z. Chang, D. Xiao, and W. Wu, Nat. Mater. **18**, 1054 (2019).

[18] T. H. R. Skyrme, "A Non-Linear Theory of Strong Interactions", Proc. Roy. Soc. (London) A **247**, 260-278 (1958).

[19] C. Naya and P. Sutcliffe, "Skyrmions and Clustering in Light Nuclei", Phys. Rev. Lett. **121**, 232002-1-5 (2018).

[20] D. Xiao, M.-Ch. Chang, and Q. Niu, "Berry phase effects on electronic properties", Rev. Mod. Phys. **82**, 1959–2007 (2010).

[21] R. Skomski, B. Balasubramanian, A. Ullah, C. Binek, and D. J. Sellmyer, AIP Adv., **12**, 035341 (2022).

[22] W. Jiang, P. Upadhyaya, W. Zhang, G. Yu, M. B. Jungfleisch, F. Y. Fradin, J. E. Pearson, Y. Tserkovnyak, K. L. Wang, O. Heinonen, S. G. E. te Velthuis, and A. Hoffmann, "Blowing magnetic skyrmion bubbles", Science 349, Issue 6245, pp. 283-286 (2015).

[23] M. Lonsky and A. Hoffmann, "Coupled skyrmion breathing modes in synthetic ferri- and antiferromagnets", Phys. Rev. B 102, 104403-1-11 (2020).

[24] E. Pinilla-Cienfuegos, S. Mañas-Valero, A. Forment-Aliaga, and E. Coronado, ACS Nano **10**, 1764 (2016).

[25] Balamurugan Balasubramanian*, Kristin L. Kraemer, Nicholas A. Reding, Ralph Skomski, Stephen Ducharme, and David J. Sellmyer, ACS Nano **4**, 1893 (2010).

[26] R. P. Cowburn, D. K. Koltsov, A. O. Adeyeye, M. E. Welland, and D. M. Tricker Phys. Rev. Lett. **83**, 1042 (1999).

[27] B. Balasubramanian, T. A. George, P. Manchanda, R. Pahari, A. Ullah, R. Skomski, and D. J. Sellmyer, Phys. Rev. Mater. **5**, 024402-1-9 (2021).

Chapter 2 Experimental and Computational Methods

2.1 Fabrication

The physics vapor deposition (PVD) techniques such as magnetron sputtering and electron beam evaporation are based on high vacuum techniques used for the deposition of thin films [1]. In these methods, the material is collected onto the surface/substrate in the form of condensed vapor. The PVD techniques used for the fabrication of nanodots in this thesis are electron beam evaporation and magnetron sputtering.

2.1.1 Electron Beam Evaporation

In electron beam (e-beam) evaporation, a stream of electrons is aimed at the source material [2]. The beam of electrons with kinetic energy heats the target source material to its melting point and evaporates the source material. This electron beam is well confined by the magnet to the source. In e-beam evaporation, we can rotate the different source materials in the path of the electron beam to evaporate and can deposit multiple layers [2].

The electron beam evaporation system has two main components. First the electron source or electron gun produces the beam of electrons. Second, the crucible where the source material is contained. The electron gun has a filament which is the source of the electron and a magnet which directs the electron toward the crucible with the source material. An Electron beam is generated by heating metal filament. At high temperatures, the electron leaves the filament and accelerates toward the source material due to high voltage. The electron beam does not lose any kinetic energy as the system is maintained at low pressure in a vacuum and the electron does not collide with atmospheric atoms. The kinetic energy of electrons is converted into heat and evaporates

the materials. The kinetic energy can be controlled by filament current and applied potential. The source material is placed in a crucible made of Cu, or ceramic. The system contains multiple crucibles with different sources, from which thin film of multiple layers can be deposited. The rotator holder of Cu is used to rotate the crucible in the electron beam path. The Cu rotator is cooled by water which prevents the crucible from melting and mixing with the source.

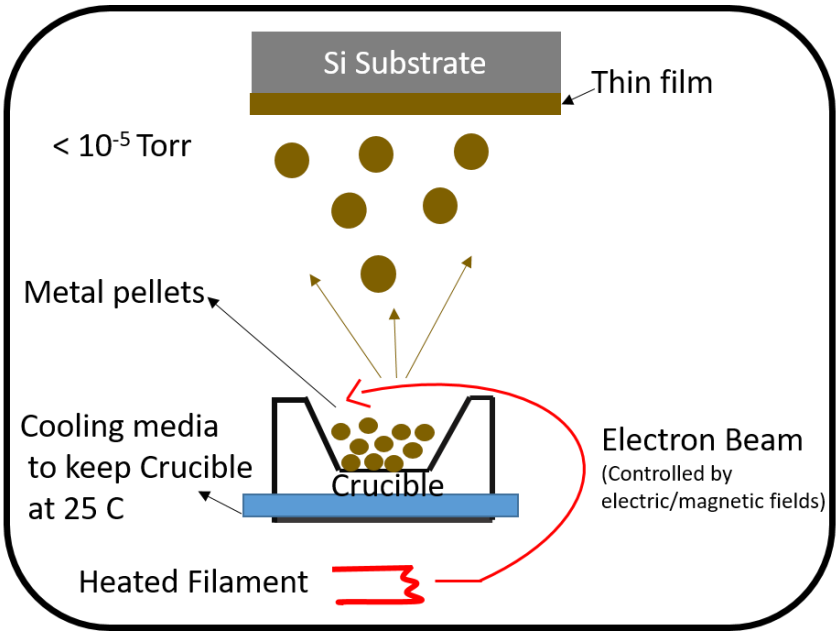

Figure 2.1 The deposition process of electron-beam-induced evaporation by e-type electron gun.

2.1.2 Magnetron Sputtering

Magnetron sputtering is a completely different deposition method as compared to electron beam evaporation [2, 3]. In sputtering the energetic atoms hit the target and remove the source materials atoms from the target [2, 3]. These atoms then travel through vacuum chambers and get collected on the substrate to make thin films. Usually, the extracted atom from the source target has high kinetic energies which are lost by the collision with inert gas atoms.

The energetic atoms which are used to eject the source atoms are Ar ions in the plasma. In the vacuum system after loading the target and substrate the chamber is evacuated to 10^{-6} Torr. Then the Ar gas is allowed to enter the chamber. In the presence of Argon in the chamber high negative voltage is applied to the target. The high potential ionizes the Ar atoms creating Ar+ ions attracted by the strong potential at the target. These Ar+ ions with high kinetic energies knock out the individual atoms from the target material. The sputter atoms move through the chamber and get cooled on the substrate. Usually, the sputtered atoms move in all directions. With the desired thickness of the film, the voltage is turned off and the sputtering of atoms from the source target stops. The schematic image of the sputtering system is shown in the Fig. 2.2

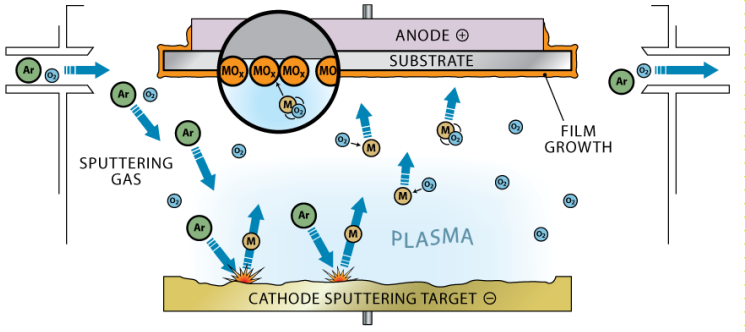

Figure 2.2. The deposition process of thin film by Ar-atom induced sputtering.

2.1.3 Sputtering with Gas Aggregation Chamber

The thin film of nanoparticles is created by using sputtering with a gas aggregation chamber. In this system, the sputtered atoms combine and make nanoparticles and then collected on the substrate to make nanoparticle films [3, 4]. The method involves three stages. First sputtering of atoms from the target, second, aggregation of atoms to make nanoparticles and third collection of nanoparticles in the deposition chamber. The whole system is divided into two parts, the aggregation chamber

and the deposition chamber. The aggregation chamber consists of sputtering and its walls are cooled down by either water or N2. The volume of the gas aggregation chamber can be changed in order to get different sizes of nanoparticles. For small nanoparticles the lowered volume results in a smaller number of collisions with the same type of atoms, resulting in a decrease in the size of nanoparticles. For bigger particles, the size of the chamber is usually increased.

The vaporization of atoms from the target is similar to the sputtering method described in the previous section involving the creation of plasma around the target source due to the application of a high electric field that ionizes the inert gas. The plasma gas in this system is confined to the source as shown in Fig. 2.3 by the circular magnet behind the target source. After the sputtering of the atoms from the target, the atoms move in an aggregation chamber and their kinetic energies decrease due to collision with the inert gas atoms. These inert gas atoms lose their energies during the collision with the wall of the chamber which is cooled by the water.

As long as the atoms stay in the aggregation chamber, they combine and make nanoparticles. Due to the difference between the pressure of the aggregation chamber and the deposition chamber, the sputtered atoms and nanoparticles move away from the plasma and cool down. The nanoparticle further moved to a small nozzle of 1mm diameter which connects the deposition chamber and aggregation chamber and finally deposits onto the substrate.

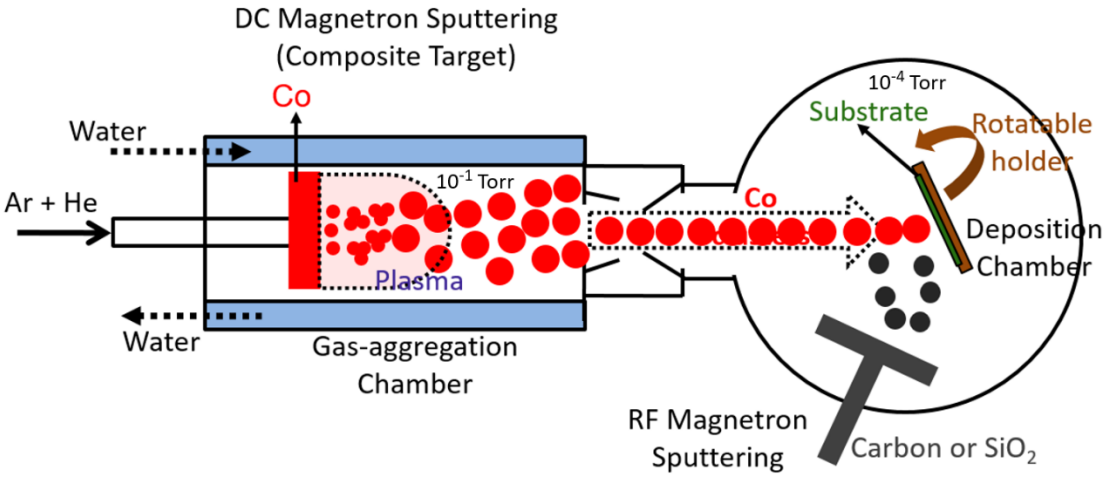

Figure 2.3. The deposition process of a thin film of Co nanoparticles by Ar-atom induced sputtering.

2.2 Electron Beam Lithography

Electron beam lithography (EBL) is used for the fabrication of small feature the size of down to 10 nm. This lithography method is different from photolithography in the sense that it uses an electron beam to react with the resist and no mask is needed, making it easy and fast. In this lithography technique, the computer-aided program is used to write the pattern on the substrate and that pattern is directly loaded into the EBL machine. Substrates on which we want to put a pattern are normally semiconductor wafers such as Si. The wafer is loaded with a thin polymer layer using a process known as a spin coating [5, 6].

2.2.1 Spin Coating

In the process of spin coating, the substrate is coated with a polymer resist. It is accomplished by depositing a few millimeters of liquid polymer on the substrate and spring at high speed between 3000 rpm to 5000 rpm. For higher speeds, the thickness of the polymer decreases. The spring of the substrate is usually done for 30 sec to 1 min. Spinning results in the evenly spreading of polymer for a uniform thin film of resist.

Usually, a thin resist is needed to create the small feature sizes. The thickness can be varied from 50 nm to 500 nm. The uniform polymer resistance of the substrate ensures pattern is accomplished accurately. After spinning, the substrate is heated on a high plate for 1 min to a temperature close to 180 C.

2.2.2 Exposure to Electron Beam

The substrate with polymer resist is put in the EBL system for exposure to the electron beam. The schematic of e-beam exposure is shown in Fig. 2.4. Exposure to a substrate with a polymer resist results in a chemical change in the resist. The EBL instrument has three main sections. First, the electron source emits electrons when high voltage is applied. 2nd is the electromagnetic lens system. It focuses on the beam of electrons. The electron beam can be focused to an extremely small spot size, less than 5nm in diameter. The 3rd section of the EBL instrument is the deflector. The deflector deflects the focused beam of electrons at extremely high speed. This controls the position of the electron beam allowing the beam to be directed to different regions of the substrate. The beam deflector usually moves the electron beam from one place to another position in small intervals. The deflection is done based on a pattern that is written on a computer program and loaded into the EBL system. The EBL system reads the data from a computer-generated pattern and writes the pattern using a deflector. Overall, the electron beam emits the electron, the lens system focuses the electron beam and the deflector streams the electron beam over the surface.

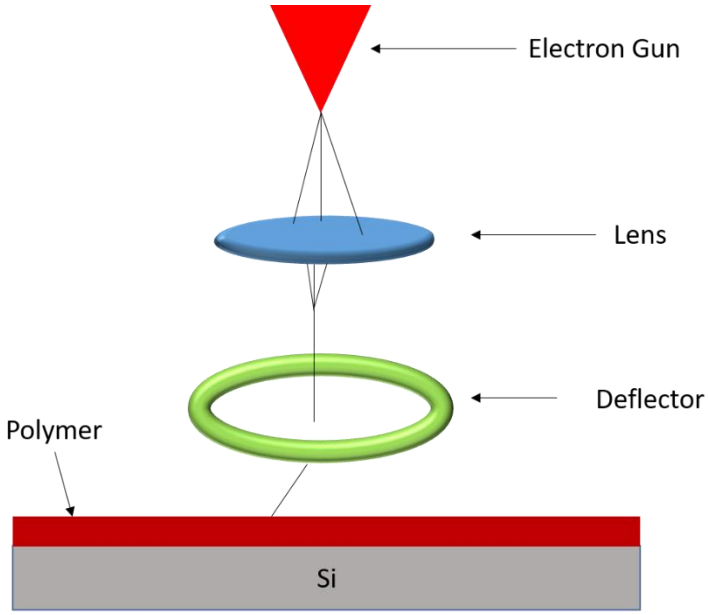

Figure 2.4. Schematic of electron beam instrumentation.

2.2.3 Development

After the completion of exposing the polymer with an electron beam, the substrate is called the exposed substrate. The region of exposed polymer resist has different chemical properties as compared to exposed resist. The exposed substrate is submerged into a chemical called MBIK developer. The developer will only react and dissolve the material which was exposed to the electron beam. It will not have any effect on a polymer that is not exposed to an electron beam. After a brief time in development, the substrate is cleaned with isopropanol and dried by N_2. It gives the substrate the pattern. This substrate is then put in a PVD system for the deposition of material etc.

2.2.4 Lift Off

After patterning and development steps the wafer only has unexposed polymer. In PVD the film is deposited on the whole region including the developed region (pattern) and unexposed region of the polymer. In any area where the resist was exposed to an electron beam, the material sticks to Si substrate during the deposition. After the

deposition when the substrate is put in acetone, the resist chemically reacts with acetone, and the deposited material on the unexposed polymer is removed along with the polymer. It gives rise to nano feature deposited material on Si substrate. The schematic of liftoff processes is shown in Fig. 2.5.

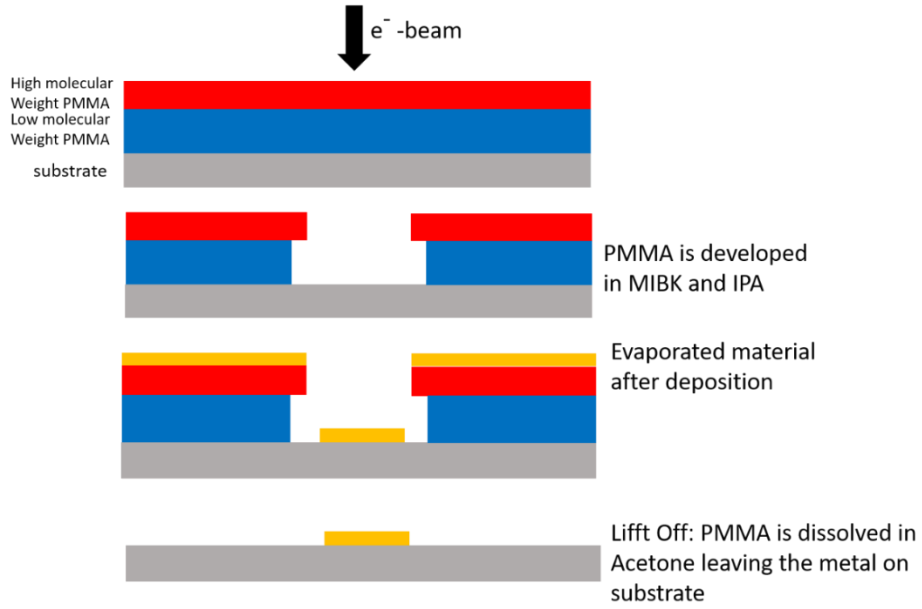

Figure 2.5. Schematic of nanofabrication's step using electron beam lithography, thin film deposition, and lift-off.

2.3 Magnetic Force Microscopy

Magnetic force microscopy is the technique by which the magnetic properties of the surface can be imaged. It is used to reveal the magnetic domain structure of magnetic materials by detecting and imaging the magnetic stray field out of the surface of magnetic materials. In magnetic force microscopy, a cantilever with ferromagnetic particles can interact with stray fields line close to the surface. Magnetic materials with magnetic domains oriented differently will produce stray fields directed in opposite directions as shown in Fig. 2.6. So, in this type of situation, the MFM tip scanning across the sample will experience the force directed in different directions. In one case the tip will

experience the repulsive force while in another case the tip will experience the attractive force. With these two different types of forces from the ferromagnetic particles, the tip of the cantilever will deflect differently between different regions during imaging and gives rise to an image representing the gradient of the stray fields on the sample surface.

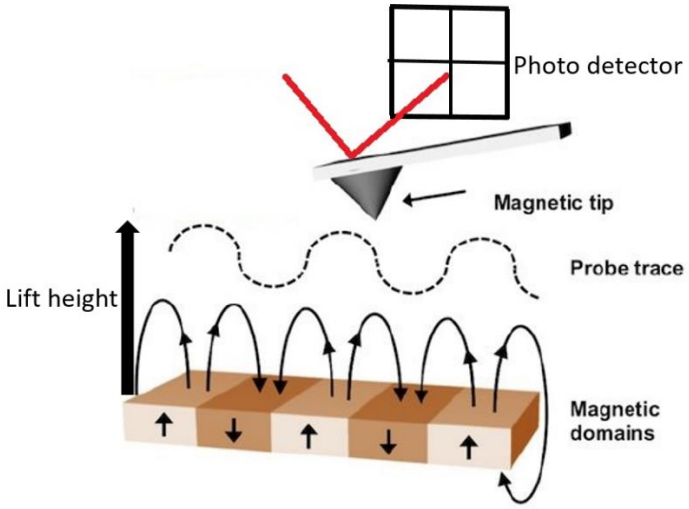

Figure 2.6. Schematic figure showing the interaction between the magnetic and stray field using the domain configuration on the surface of the material. The figure is taken from reference [8].

Magnetic force microscopy is usually done in dynamic mode. In this mode when the tip is brought close to the surface for scan, the change in magnetic interaction gives rise to a change of the cantilever status such as static deflection. The magnetic force acting on the tip due to field lines [7],

$$\boldsymbol{F} = \iint dr^3 dr'^3 \; M(\boldsymbol{r}) \boldsymbol{\nabla} . \boldsymbol{H}(\boldsymbol{r}, \boldsymbol{r}') \tag{1}$$

Here in $M(\boldsymbol{r}')$ is the magnetization of a tip at position $\boldsymbol{r}$ and $\boldsymbol{H}(\boldsymbol{r}, \boldsymbol{r}')$ is the stray field at position $\boldsymbol{r}$ created by magnetic material at position $\boldsymbol{r}'$. This force directly deflects the cantilever by displacement,

$$\delta \boldsymbol{z} = \frac{\boldsymbol{F_c}}{k_c} \tag{2}$$

$\boldsymbol{F_c}$ is a component of force normal to the cantilever or parallel to the probe it causes the cantilever to bend and k_c is the spring constant of the cantilever. The force on the cantilever changes the angular orientation of the light beam reflected from the surface of the cantilever.

During magnetic force microscopy measurement when the distance between the surface and tip is less than 10 nm, the Vander Wall interactions between atom on the tips and atoms on the sample surface also gives rise to topographic features in the magnetic images. When the distance between the surface and tips is greater than 20 nm, the feature only contains magnetic forces as the Van der Waals forces are weaker at a large length scale. To avoid the topographic features in magnetic imaging and magnetic force microscopy is usually done in the lift mode. In lift mode, the cantilever is first brought close to the surface i.e. 10 nm with feedback ON. At this point, the topographic information is obtained. Then the cantilever is raised to a height called lift height with feedback off. The cantilever retraces the topographic information to obtain only magnetic information.

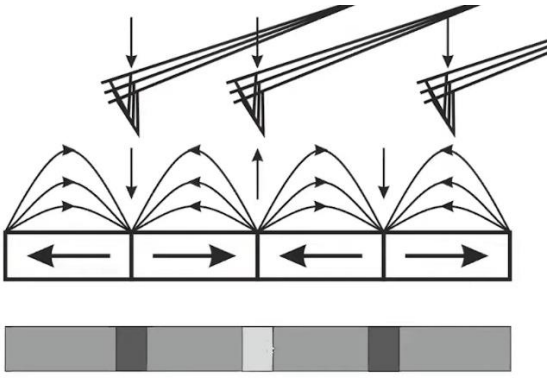

Figure 2.7. Behavior of magnetic tip showing its motion due to force between tip and field lines representing magnetic domains. The figure is taken from reference [8].

The image contrast can be explained by considering the force between the strong field and magnetic atoms on the cantilever. The image contrast can be explained by three cases as shown in Fig. 2.7. In case one when the local magnetic moment in the tip attached to the cantilever is aligned parallel to the local stray field gradient. This configuration gives rise to an attractive force corresponding to the dark color configuration in magnetic imaging. In the 2nd case when the dipole is antiparallel to the local field gradient, the force is repulsive, which shows bright color. In the 3rd case when the field gradient and the dipole moment are perpendicular to each other, there is no vertical force between the dipole and stray field, and the color is intermediate.

2.4 Superconducting Quantum Interference Device (SQUID)

A SQUID magnetometer is used to measure the magnetic signal (magnetic moment) by implementing the quantum interference effect of currents in two different Josephson junctions. Josephson effect shows the quantum tunneling of superconductor single electrons or cooper pair from one superconductor to another through an insulator [9,10]. The two superconductors are separated by an insulator through which the cooper pair of different phase tunnel and produces current. This effect gives evidence of quantum tunneling phenomena.

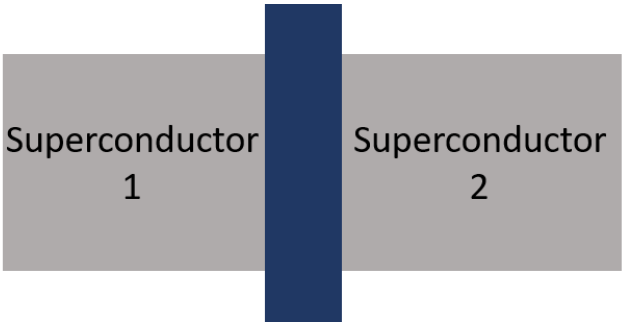

Figure 2.8 Two superconductors are separated by an insulator and a tunneling junction.

The current flowing through the insulator is proportion to the change in cooper pair density with respect to time, which is given by [11].

$$J = J_c \sin(\theta_2 - \theta_1) \tag{3}$$

where θ_1 and θ_2 are the phase of cooper pair with wave function given by $\Psi = \Psi_o e^{i\theta(r)}$. θ changes from one superconductor to the other. The SQUID magnetometer uses the concept of Josephson junction and flux quantization in a superconductor ring. The flux quantization in the superconductor ring arises by using the Meissner effect which states that the current density $\boldsymbol{J}$ is zero in the interior in the presence of external magnetic flux which is also absent in the superconductor [11],

$$\boldsymbol{J} = \Psi^* (\boldsymbol{p} - q\boldsymbol{A})\Psi = \frac{n}{m}(\hbar\nabla\theta(r) - q\boldsymbol{A}) = 0 \tag{4}$$

$$\hbar\nabla\theta(r) = q\boldsymbol{A} \tag{5}$$

taking the line integral and using the Stokes theorem,

$$\hbar(\theta_2 - \theta_1) = \frac{q}{c}\oint \boldsymbol{A}.d\boldsymbol{l} = \frac{q}{c}\int curl\, \boldsymbol{A} d\boldsymbol{s} = \frac{q}{c}\int \boldsymbol{B}.d\boldsymbol{s} = \frac{q}{c}\Phi \tag{6}$$

Here $\Delta\theta$ is the change in phase of the wave function as the cooper pair makes a complete round trip along the ring. So with $\Delta\theta = 2\pi n$,

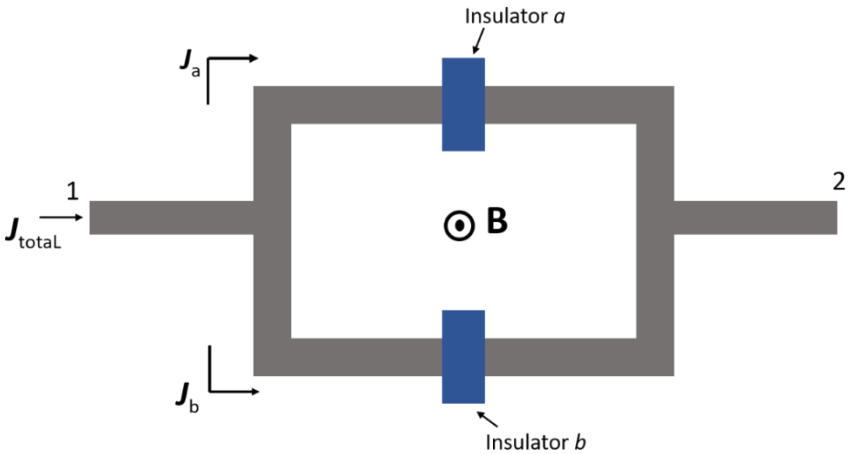

Figure 2.9 Quantum interference: A magnetic flux due to magnetic field B passes through the interior of the loop.

$$\hbar 2\pi n = q\Phi. \tag{7}$$

Giving quantized flux of

$$\Phi = n\frac{h}{q} \tag{8}$$

shows the Cooper pair acquire a quantized flux in the ring of the superconductor in the presence of the external magnetic field. For cooper pair $q = 2e$ and $\Phi = n\frac{h}{2e}$. The SQUID magnetometer is based on the interference of tunneling current through the junctions in the presence of the magnetic field. The total current is given by [11],

$$J = J_c\,(\sin(\delta_a) + \sin(\delta_b)). \tag{9}$$

In the absence of an external magnetic field $\delta_a = \delta_b = \delta_0$. But in the presence of a magnetic field

$$\hbar(\delta_a - \delta_b) = q\Phi \tag{10}$$

which gives the phase change through the insulator as

$$\delta_a = \delta_0 - \frac{q}{2\hbar}\Phi, \quad \delta_b = \delta_0 + \frac{q}{2\hbar}\Phi \tag{11}$$

and current density

$$J = J_c\left(\sin\left(\delta_0 - \frac{q}{2\hbar c}\Phi\right) + \sin\left(\delta_0 - \frac{q}{2\hbar}\Phi\right)\right) \tag{12}$$

$$J = J_c\left(\sin(\delta_0)\cos\left(\frac{e}{\hbar}\Phi\right)\right) \tag{13}$$

with $\frac{e\Phi}{\hbar} = n\pi$. In the above equation, the current varies with the magnetic field through a circular superconductor due to the external magnetic field. The last equations show that the oscillations in the current *J*, caused by the total flux Φ, are the result of the interference of the two supercurrents flowing through the individual Josephson junctions.

So the interference occurs whenever a new flux is created. As the flux change, the current oscillates as a function of the magnetic field. The current in the above equation resembles the interference effect in a double-slit experiment. During the magnetization measurement in SQUID, the magnetic material is moved in the circular coil creating the induced current. This induced current generates a magnetic field and hence magnetic flux in the superconductor coil with the Josephson junction. Change in magnetization in magnetic material leads to a change in current in magnetic coils which changes the magnetic flux in the SQUID loop. The SQUID loop is normally away from the coil with magnetic material and flux is created by the principle of the transformer.

2.5 Numerical Method

The numerical method to understand the magnetization in a magnetic material is based on micromagnetics. In micromagnetics, the neighboring moments have an effect on alignment with each other. This gives rise to a continuum model in which the magnetization can be described by the continuous vectors field i.e., magnetization $\boldsymbol{M} = \boldsymbol{M}(\boldsymbol{r}, t)$ is a function of both space and time [12]. The magnetization field changes slowly with respect to both space $\boldsymbol{r}$ and time t. The continuous description of magnetization is expressed as

$$\boldsymbol{M}(\boldsymbol{r}, t) = M_s(r)\boldsymbol{m}(\boldsymbol{r}, t). \tag{14}$$

Where $\boldsymbol{m}(\boldsymbol{r}, t)$ is the normalized magnetization field vector. In micromagnetic the magnitude of the vector field ($M_s(r)$) does not change with time and remains constant. It represents the constant norm associated with the magnetization vector represented by $||\boldsymbol{M}(\boldsymbol{r}, t)|| = M_s(r)$. The normalized magnetization field vector $\boldsymbol{m}(\boldsymbol{r}, t)$ has the main

importance in micromagnetics. The change in the direction of the magnetization vector is explained by normalized vector $\boldsymbol{m}(\boldsymbol{r}, t)$ given that

$$\left|\left|\boldsymbol{m}\right|\right| = {m_x}^2 + {m_y}^2 + {m_z}^2 = 1 \tag{15}$$

The direction of the normalized vector changes with respect to time until equilibrium is achieved. Knowing how the direction of ***m*** changes gives all the information about the properties associated with the system. In micromagnetics usually, ***m*** is solved by numerical calculation, however, there are limited cases where ***m*** is solved analytically.

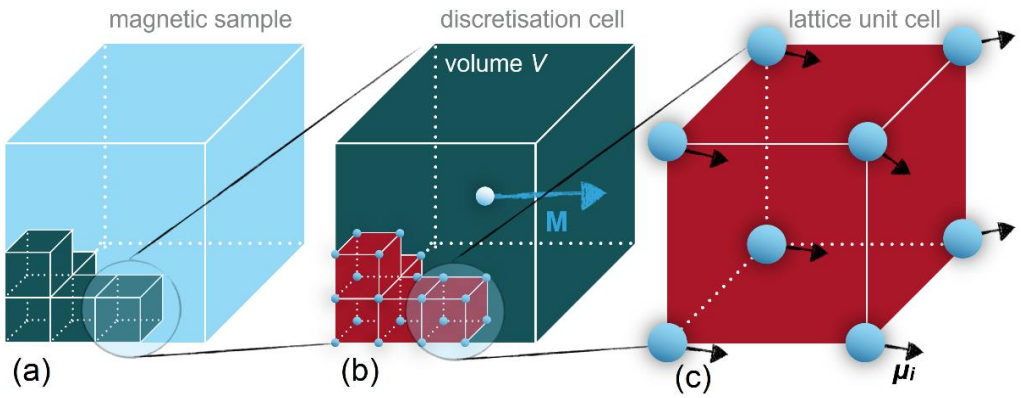

Figure 2.10 Micromagnetic Discretization: (a) Magnetic sample divided into discrete cells (b) Discrete cell consists of atoms arranged in the lattice unit cell (c) atomic lattice unit cell. The figure is taken from reference [12].

In micromagnetics, to solve the magnetization numerically the magnetic geometry is divided into small cells called discretization cells. We can discretize the field by the finite difference method. There are a number of software for finite difference numerical simulations, like OOMMF, MuMax3, and Fidimag. Here in this thesis, we used *ubermag* which is Python-based OOMMF software. In general, there are two rules that need to be considered when the size of the discretization cell is defined: first, it should be large enough to ignore the crystal structure of the materials and second it should be small enough to determine different magnetization features like domain wall, magnetic vortex,

etc. The size of the discretization cell is usually considered lower than the exchange length.

In finite difference discretization, the magnetic sample Fig. 2.10(a) is divided into small cells which are cubes in the finite difference method. Fig. 2.10(b) shows one of the cubes with the magnetic geometry. Within the cell, there are a bunch of magnetic atoms. Fig. 2.10(c) is an example of on lattice unit cell of crystal structure in the discrete cube. The magnetization in a discretization cell is obtained by the sum of all magnetic moments associated with the atoms and divided by the volume of the cell. The magnetization in *i*th discretization cell at position $\boldsymbol{r}_i$ at time t_i is given by,

$$\boldsymbol{M}_i(\boldsymbol{r}_i,\, t_i) = \sum_{i \epsilon V} \frac{\mu_i}{V}. \tag{16}$$

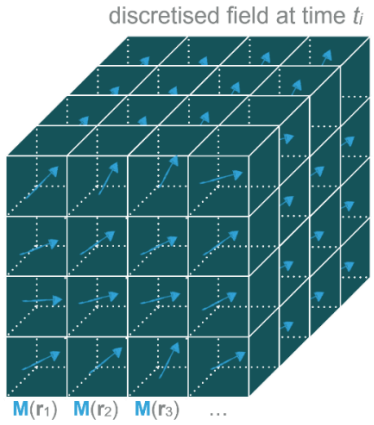

Figure 2.11 Discrete cells: Each discrete cell act as a tiny magnet with associated magnetization which interacts with neighboring discrete cells. The figure is taken from reference [12].

This is the magnetic vector assigned to the discretization cell. Each discretization sample has one vector assigned to it. The main assumption is that the magnetization is uniform in every discretization cell with a unit vector representing the direction of magnetization in that unit cell and magnetization varies smoothly over different cells. Fig

2.11 shows that the sample is divided into small cubes and each cube has a single vector in it $\boldsymbol{M}_i(\boldsymbol{r}_i,\ t_i)$.

References

[1]J. E. Mahan, Physical Vapor Deposition of Thin Films, *John Wiley &Sons, New York* (1999).

[2] Y. Lin, Advanced Nano Deposition Methods, 1st ed.; Wiley-VCH: Weinheim, Germany, (2016).

[3] Y. Huttel, CH. 15, Gas-Phase Synthesis of Nanoparticles; *Wiley-VCH: Weinheim, Germany*, (2017).

[4] H. Haberland, M. Karrais, M. Mall, and Y. Thurner, Thin films from energetic cluster impact: A feasibility study, *Journal of Vacuum Science & Technology* **10**, 3266 (1992).

[5] P. Rai-Choudhury, Handbook of Microlithography, Micromachining, and Microfabrication. Volume 1: Microlithography; SPIE PRESS: Bellingham, WA, USA, 1997;

[6] A. Tseng, C. Kuan Chen, C. D. Chen, K. J. Ma, Electron beam lithography in nanoscale fabrication: recent development. *IEEE Trans. Electron. Packag. Manuf.*, **26**, 141 (2003).

[7] D. A. Bonnel, Scanning Probe Microscopy and Spectroscopy (Wiley, New York, 2001).

[8] https://www.hitachi-hightech.com/global/en/knowledge/microscopes/spm-afm/descriptions/mfm.html, https://www.azonano.com/article.aspx?ArticleID=5958

[9] S. Foner, Versatile and Sensitive Vibrating-Sample Magnetometer, Review of Scientific Instruments 30, 548 (1959).

[10] R. C. Jaklevic, J. Lambe, A. H. Silver, and J. E. Mercereau, Quantum Interference Effects in Josephson Tunneling, Physical Review Letters 12, 159 (1964).

[11] C. Kittel, Introduction to Solid State Physics 4th Edition *John Wiley & Sons, New York,* (1971)

[12] M. Beg, M. Lang, and H. Fangohr, IEEE Trans. Magn. 58, 7300205 (2022).

Chapter 3 Berry Curvature in Magnetic Nanoparticles

3.1 Introduction

When a quantum system traverses in a continuous parameter space slowly, it follows the environment adiabatically, i.e., remaining in the same eigenstate according to the local value of the parameters. Consequently, the wavefunction of the system accumulates a non-dynamic phase called the Berry phase, which is equal to the path integral of Berry connection in the parameter space, or the areal integral of Berry curvature in case the trajectory is a closed loop [1, 2]. This mechanism applies to the process of itinerant electrons flowing through a spin texture in real space, where the spin of the itinerant electron follows the direction of the local spin [3]. The change of spin direction of the itinerant electrons can be described using an emerging magnetic field $\vec{B}_e$ which is proportional to the Berry curvature $\vec{\Omega}$ as $\vec{B}_e = \frac{\hbar}{e}\vec{\Omega}$, where $\hbar$ and e are reduced Plank constant and electronic charge [4]. The Berry curvature can be found in the spin texture

$$\vec{\Omega} = -\epsilon_{ijk}\frac{1}{2}\boldsymbol{S}\cdot\left(\partial_i\boldsymbol{S}\times\partial_j\boldsymbol{S}\right), \quad (1)$$

where $\boldsymbol{S}(\boldsymbol{r})$ is the unit vector describing the spin direction at position $\boldsymbol{r}$, ϵ_{ijk} is the antisymmetric tensor. This can be understood using Fig. 3.1. When $\boldsymbol{S}\cdot\left(\partial_i\boldsymbol{S}\times\partial_j\boldsymbol{S}\right)\neq 0$, the electron trajectory can enclose a non-zero solid angle in the Bloch sphere, which is equal to the Berry phase accumulated.

A famous example that leads to non-zero $\vec{\Omega}$ is the Skyrmion, which is a two-dimensional (2D) spin texture of rotational symmetry [3,4] whose $\boldsymbol{S}$ rotates ±180º from the center to the boundary. In general, the areal integration of $\vec{\Omega}$ of a 2D spin texture of rotational symmetry follows $Q = \frac{1}{2\pi}\int\vec{\Omega}\cdot d\vec{A} = S_z(\infty) - S_z(0)$, where $S_z(0)$ and $S_z(\infty)$ are the z

component of $\boldsymbol{S}$ at the center and far away. Q is also called Skyrmion number because the value is ±1 for Skyrmion [4]. Correspondingly, the areal integral of the emerging field of the Skyrmion is $\int \vec{B}_e \cdot d\vec{A} = \pm\frac{h}{e}$ or the magnetic flux quantum. Some other examples of spin texture with finite Skyrmion number are chiral spin texture, magnetic vortex, and meron [5, 6].

Given that the areal integral of $\vec{\Omega}$ and $\vec{B}_e$ are constant for a Skyrmion regardless of its area, the average Berry curvature $\vec{\Omega}$ and the emerging field $\vec{B}_e$ are then inversely proportional to the Skyrmion area A, or proportional to the areal density of the Skyrmion Ψ as $< |\vec{\Omega}| >= \frac{2\pi Q}{A} = 2\pi\Psi$. For an area A with multiple Skyrmions, the average $\vec{B}_e$ and $\vec{\Omega}$ only depends on the topology of the spin texture, i.e., the number of Skyrmions *N*, or the number of "holes" in the spin texture as $< |\vec{\Omega}| >= 2\pi\Psi = \frac{2\pi NQ}{A}$, regardless of the shape of the "holes". This is the origin of the name topological Hall effect (THE) generated by $\vec{B}_e$ [4, 3, 7, 8]. The Berry-curvature contributions to the Hall effects, i.e., THE, represent a research topic in its own right but are also technologically interesting.

In this chapter, we investigate the spin structure in ferromagnetic nanoparticles and the corresponding Berry curvature. Previous work shows that thin films exhibit magnetic skyrmions and other types of spin textures, which leads to a topological Hall effect [4,3,7,8]. Traditionally, such spin textures are not expected in small isolated nanoparticles because the exchange interaction ensures parallel spin alignment on small-length scales [9,10,11]. However, nanogranular materials exhibit features similar to that of thin films with skyrmions-like spin textures [12, 13]. For example, nanoparticles with DMI interaction create a curling mode without nucleation and gives rise to the

topological Hall effect [14]. But these examples are related to interacting magnetic nanoparticles. Recently, it has been reported that isolated nanoparticles of noncentrosymmetric B-20 structures can exhibit geometrically stabilized skyrmionic spin textures [15]. However, Berry curvature in non-interacting centrosymmetric nanoparticles with minimum state magnetic energy is yet to be systematically modeled.

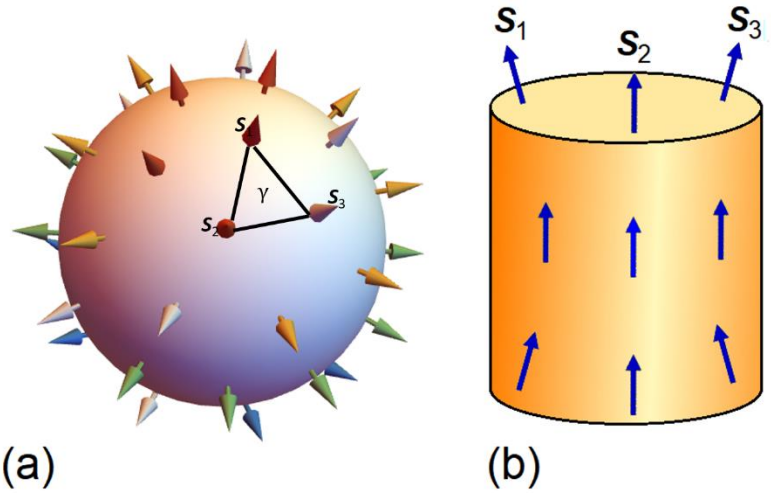

Figure 3.1. Berry curvature: (a) rotating spin on a Bloch sphere and (b) noncoplanar spins in a nanostructure [5]. When the three vectors are symmetrically arranged and form an angle Θ with the symmetry axis, gives rise to finite spin chirality χ_s.

We used micromagnetic approach to investigate the spin structure in ferromagnetic nanoparticles. We calculated the Berry curvature for nanoparticles with non ellipsoidal shapes which tend to exhibit flower-state spins structures [10, 16] which compete against other spin structures, such as vortex states due to magnetostatic flux closure [9,10,11,16,17,18]. Our focus is on the transition between flower and curling states as the size of nanoparticle changes across the coherence radius R_{coh} [9,10,11,19] and the corresponding Berry curvature. R_{coh} reflects the competition between magnetostatic and exchange energies, it is independent of the anisotropy constant K_1. In particular, it is unrelated to the critical single-domain size R_{SD}, which can be much larger

than R_{coh} [20]. We found that in general flux closure is favorable but competes against the exchange interaction. The latter scales as A_e/R^2 and is therefore less important in big particles. In small particles, the A_e/R^2 term completely kills the curling/vortex contribution and largely (but not completely) the flower-state contribution and the Berry curvature.

3.2 Methods

Throughout the paper, we express the local magnetization $\boldsymbol{M}(\boldsymbol{r})$ as $\boldsymbol{M}(\boldsymbol{r}) = M_s\, \boldsymbol{S}(\boldsymbol{r})$, where $\boldsymbol{S}(\boldsymbol{r})$ is a unit vector representing the normalized quasi-classical spin. The spin of the charge carriers is assumed to follow the local magnetization adiabatically, so that $\boldsymbol{S}(\boldsymbol{r})$ also characterizes the conduction electrons. These spin structures are investigated analytically, by considering an approximate Hamiltonian, and by micromagnetic simulation using *Ubermag* [22]. The determination of local configuration $M(\mathrm{r}) = M_s\, \boldsymbol{S}(\boldsymbol{r})$, done by energy function is given by [11, 21]:

$$\mathscr{E} = \int \left\{ A_e \left[\nabla\left(\frac{\boldsymbol{M}}{M_s}\right) \right]^2 - K_1 \frac{(\boldsymbol{n}.\boldsymbol{M})^2}{{M_s}^2} - \mu_o\, \boldsymbol{M}.\boldsymbol{H} - \frac{\mu_o}{2}\, \boldsymbol{M}.\boldsymbol{H}_d(\boldsymbol{M}) \right\} \mathrm{d}V \qquad (2)$$

Where A_e is the exchange stiffness, $K_1(\boldsymbol{r})$ denotes the first uniaxial anisotropy constant, $\boldsymbol{n}(\mathbf{r})$ is the unit vector of the local anisotropy direction, $\boldsymbol{H}$ is the applied field and $\boldsymbol{H}_d(\boldsymbol{M})$ is the magnetostatic self-interaction. Physically $\boldsymbol{M}(\mathbf{r})$ corresponds to local and global minima. Before presenting exact analytical and numerical results for $\boldsymbol{S}(\boldsymbol{r})$, we provide an analytical scaling analysis to gauge the broad range of effects important in the present context. The basic idea goes back to Felix Bloch [23], where an approximate quantum-mechanical energy functional (p. 324) and a variational argument (p. 325) were used to show that the domain-wall width is of the order of $(A_e/K)^{1/2}$, where A_e is the exchange

stiffness and K is the first uniaxial anisotropy constant. We know today that quantum mechanics beyond the determination of A_e and K is not necessary, because micromagnetic distances ($\geq$ 10 nm) are much larger than interatomic distances (about 0.25 nm). Furthermore, micromagnetic (free) energies soon became well-understood [24], and present-day micromagnetism is almost exclusively based on continuum theory [9, 10,11, 24, 25, 26, 27,]. Approximate energy functional creates errors such as a wall width $(A_e/K)^{1/2}$ rather than the exact result $\pi(A_e/K)^{1/2}$ [11, 27] but have the advantages of yielding estimates for systems without exact solutions and of elucidating parameter dependences that are cumbersome to investigate numerically [11, 28].

To model the spin textures in nanoparticles and study Berry-phase numerically, we have performed micromagnetic simulations using *ubermag* supported by OOMMF [22]. We have numerically extracted the skyrmion number Q from the spin structure. For simulations different sizes of nanoparticles were considered for the study of flower, curling, and vortex state. We have used a computational cell size of 1.9 nm, which is well below the exchange length l_{ex} [11].

Samples of Co ferromagnetic dots were made by using electron-beam lithography and evaporation in an ultrahigh vacuum using an electron-beam gun. The circular nanodot patterns were defined on thermally oxidized Si substrates with positive resists. The bilayer positive resists PMMA950/MMA EL6 was exposed to an electron beam and the liftoff method was used to create the circular pattern. Ordered Co circular arrays were fabricated, in a trilayered structure of Ti/Co/SiO_2 were fabricated. The circular layered structure was grown by e-beam evaporation in a UHV system. The base pressure was in the range of 1×10^{-8} torr. The evaporation pressure is less than 5×10^{-7} torr. The

thickness is in the range of ~20 nm for Ti and ~40 nm for Co, and ~20 nm SiO_2 layer to prevent oxidation. The thickness was monitored during growth by a quartz balance for each layer. By a lift-off process, the resist is removed and dots with designed sizes remain on top of the Si surface. A Bruker Dimension Icon® Atomic Force Microscope was used to map the topography and magnetic images at room temperature. During the measurement, magnetic force microscopy was performed in constant height mode (single pass).

3.3 Calculations and Results

Equation (1) means that the Berry curvature and Skyrmion number are unique functions of the spin structure $\boldsymbol{S}(\boldsymbol{r})$, which is determined by the magnetic interactions and sample geometry. $\boldsymbol{S}(\boldsymbol{r})$ describes the orientation of magnetization at position $\boldsymbol{r}$, which can be written as [19]:

$$\boldsymbol{S}(\boldsymbol{r}) = \sin\Theta(\boldsymbol{r})\cos\Phi(\boldsymbol{r})\,\boldsymbol{e}_x + \sin\Theta(\boldsymbol{r})\cos\Phi(\boldsymbol{r})\,\boldsymbol{e}_y + \cos\Theta(\boldsymbol{r})\,\boldsymbol{e}_z, \quad (3)$$

where $\boldsymbol{e}_R$, $\boldsymbol{e}_x$, $\boldsymbol{e}_y$ and $\boldsymbol{e}_z$ are unit vectors along radial, x, y, and z directions respectively, $\Theta(\boldsymbol{r})$ and $\Phi(\boldsymbol{r})$ are the polar and azimuthal angles. Both the flower state and the curling state are small deviations from the homogeneous magnetization along the easy axis direction (z-axis). The deviation, or the x-y component of $\boldsymbol{S}$

$$\boldsymbol{S}_{xy}(\boldsymbol{r}) = \sin\Theta(\boldsymbol{r})\cos\Phi(\boldsymbol{r})\,\boldsymbol{e}_x + \sin\Theta(\boldsymbol{r})\cos\Phi(\boldsymbol{r})\,\boldsymbol{e}_y \quad (4)$$

is along the radial direction and the azimuthal direction for the flower and the curling state (see Fig. 3.2) respectively. Using cylindrical coordinates, i.e., $\boldsymbol{r} = (\rho, \varphi, z)$, one can describe the flower state and the curling state using $\Phi(\boldsymbol{r}) = \varphi$ and $\Phi(\boldsymbol{r}) = \varphi \pm \pi/2$ respectively.

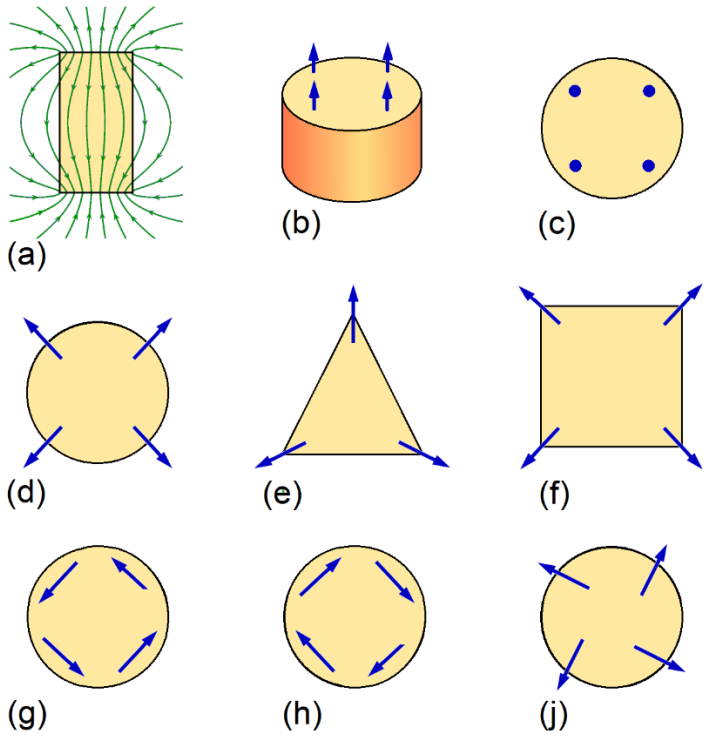

Figure 3.2. Competing spin structures in small nanoparticles: (a) field distribution in the middle of a cylindrical nanoparticle, (b-c) uniform magnetization, (d) flower state in a cylindrical particle, (e-f) flower states in prismatic nanoparticles, (g-h) vortex states of opposite chirality and (j) mixed state. The spins $\boldsymbol{S}(\boldsymbol{r})$ are shown as blue arrows.

Figure 3.2 shows schematic spin structures encountered in nanoparticles of various cross-sections, which we considered in this work to study the Emergent magnetic field in these small particles. All structures in Fig. 3.2 exhibit axial symmetry, that is, the magnetic anisotropy is of the aligned *c*-axis type and C_3, C_4, or C_∞ rotations reproduce the original spin structure. Beyond Fig. 3.1, one needs to consider the case of coherent state, where $\boldsymbol{S}(\boldsymbol{r})$ is almost constant in the particle and forms an angle with the symmetry axis of the particle i.e. flower state.

3.4 Flower State

In particles smaller than about 10 nm, the magnetization $\boldsymbol{M}(\boldsymbol{r})$ is almost uniform, as in (b-c). The reason is the interatomic exchange described by the energy density $A_e (\nabla \boldsymbol{S})^2$, where $A_e \sim 10^{-11}$ pJ/m is the exchange stiffness. The gradient term suppresses the magnetization inhomogeneities and scales as $1/R^2$, where R is the particle radius. Particles having radii of several 10 nm tend to exhibit nonuniform spin configurations, such as the side view in Fig. 3.2(a) and the top views shown in Figs. 3.2(d-f). The non-uniform state is called flower state in which the spins $\boldsymbol{S}(\boldsymbol{r})$ close to the edge forms an angle $\Theta(\boldsymbol{r})$ with the symmetry axis of the particle. The flower state is limited to non-spherical shapes, ideally cubes. In very small nanoparticles, the exchange energy $\sim A_e/R^2$ dominates and $\Theta(\boldsymbol{r})$ approaches zero as shown in Fig. 3.2(b, c). When the size increases the 'flower opens', i.e., the magnetization on these edges rotates away from the parallel orientation [16]. In the flower-state, spins tilt away from the z-axis with 'radial' symmetry. The tilt angle increases with the distance from the center, as illustrated using the spin at the particle edges or corners in Fig. 3.2(d-f). The angle Θ not only depends on the radius of the nanoparticles but also on the external magnetic field. We used micromagnetics to find $\Theta(\boldsymbol{r})$. The spin structure $\boldsymbol{S}(\boldsymbol{r})$ is determined by minimizing the micromagnetic (free) energy:

$$\mathscr{E} = \int \eta \, \mathrm{d}V \tag{5}$$

here the energy density η contains exchange, anisotropy, Zeeman, and magnetostatic-selfinteraction for flower-state contribution as described in Eq. (2). Here we show analytical calculations based on a set of simplifications to demonstrate the physical picture in a semi quantitative way. We perform an approximate volume-averaging first,

so that $\int \eta \, dV = <\eta> V$. and then minimize $<\eta>$ with respect to Θ, which is the polar angle of the magnetization at the particle edges or corners (blue arrows in Fig. 3.2); sinΘ is the length of the blue arrows in Fig. 3.2(d). An exact determination of the average $<\eta>$ is highly nontrivial because it requires the knowledge of $\boldsymbol{S}(\boldsymbol{r})$. However, $\boldsymbol{S}(\boldsymbol{r})$ is subject to some constraints (normalization and symmetry) and is approximately known for several cases. To determine the parameters in Eq. (3), we use the approximation of small values Θ. Starting from the magnetizations as:

$$\boldsymbol{M}(\boldsymbol{r}) = M_s \boldsymbol{S} = M_s \left(S_z \boldsymbol{e}_z + \boldsymbol{S}_{xy}(\boldsymbol{r}) \right) \tag{6}$$

with spin unit vector as $\boldsymbol{S}(\boldsymbol{r}) = \sin\Theta(\boldsymbol{r}) \cos\Phi(\boldsymbol{r}) \, \boldsymbol{e}_x + \sin\Theta(\boldsymbol{r}) \cos\Phi(\boldsymbol{r}) \, \boldsymbol{e}_y + \cos\Theta(\boldsymbol{r}) \, \boldsymbol{e}_z$, and

$$\boldsymbol{S}_{xy}(\boldsymbol{r}) = \sin\Theta(\boldsymbol{r}) \cos\Phi(\boldsymbol{r}) \, \boldsymbol{e}_x + \sin\Theta(\boldsymbol{r}) \cos\Phi(\boldsymbol{r}) \, \boldsymbol{e}_y \tag{7}$$

provided that $|\boldsymbol{S}_{xy}(\boldsymbol{r})| = (\sin\Theta(\boldsymbol{r}))^2$. In order to use small angle approximation can write z component of magnetization in terms of xy-component as,

$$\boldsymbol{M}(\boldsymbol{r}) = M_s \left(\sqrt{1 - S_{xy}^{\,2}(\boldsymbol{r})} \; \boldsymbol{e}_z + \boldsymbol{S}_{xy}(\boldsymbol{r}) \right) \tag{8}$$

$$\boldsymbol{M}(\boldsymbol{r}) = M_s \left((1 - \frac{S_{xy}^{\,2}(\boldsymbol{r})}{2}) \boldsymbol{e}_z + \boldsymbol{S}_{xy}(\boldsymbol{r}) \right) \tag{9}$$

Using $\nabla \boldsymbol{M}(\boldsymbol{r}) = M_s \nabla \boldsymbol{S}_{xy}(\boldsymbol{r})$, $\boldsymbol{n}.\boldsymbol{M} = M_s^2 \, (1 - \frac{S_{xy}(\boldsymbol{r})^2}{2})$, $\boldsymbol{M}.\boldsymbol{H} = M_s^2 H \, (1 - \frac{S_{xy}(\boldsymbol{r})^2}{2})$, and $\boldsymbol{M}.\boldsymbol{H}_d(\boldsymbol{M}) = -M_s^2 \, D \, (1 - S_{xy}(\boldsymbol{r})^2)$, and Eq. (2) aside from unimportant zero-point energy becomes:

$$\mathscr{E} = \int \left[A \, (\nabla \boldsymbol{S}_{xy}(\boldsymbol{r}))^2 + K \, (\boldsymbol{S}_{xy}(\boldsymbol{r}))^2 + \frac{1}{2} \mu_o \, (H - D \, M_s) \, M_s \, \boldsymbol{S}_{xy}(\boldsymbol{r})^2 \right] dV. \tag{10}$$

For small particles, $D = 0$, i.e. no magneto static self-interaction creation flux closure, hence above equation becomes

$$\mathscr{E} = \int \left[A\,(\nabla \boldsymbol{S}_{xy}(\boldsymbol{r}))^2 + K\,(\boldsymbol{S}_{xy}(\boldsymbol{r}))^2 + \frac{1}{2}\,\mu_o\,H\,M_s\,\boldsymbol{S}_{xy}(\boldsymbol{r})^{\,2} \right] dV. \qquad (11)$$

In small nanoparticles, the stoner wolfarth assumes uniform magnetization but in reality, exchange interaction competes with other energy contributions such as magnetostatic interactions, etc. In very small nanoparticles the magnetostatic interaction is absent i.e D = 0, but there is still a contribution of exchange interaction i.e. $A\nabla^2 = A/R^2$ where R is the radious of particle. So the volume averaging of eq. (11) yields the approximation:

$$\mathscr{E}/V = <\eta> = \left[\frac{A}{R^2}\,\boldsymbol{S}_{xy}(\boldsymbol{r})^{\,2} + K\,(\boldsymbol{S}_{xy}(\boldsymbol{r}))^2 + \frac{1}{2}\,\mu_o\,H\,M_s\,\boldsymbol{S}_{xy}(\boldsymbol{r})^{\,2} \right] \qquad (12)$$

For a moderately large particle with edges, the nanoparticle exhibits a flower state to minimize the energy. The flower state is given by $\boldsymbol{S} = \sin\Theta \boldsymbol{e}_R + S_z\,\boldsymbol{e}_z = S_{xy}(\boldsymbol{r})\,\boldsymbol{e}_R + S_z\,\boldsymbol{e}_z$, and carries only a little anisotropy energy. Note that we used $\Phi(\boldsymbol{r}) = \varphi$ for flower state and radial component $\boldsymbol{e}_R = \cos\varphi\,\boldsymbol{e}_x + \sin\varphi\,\boldsymbol{e}_y$ and $S_{xy}(\boldsymbol{r}) = \sin\Theta(\boldsymbol{r})$. The flower state causes a xy-component of the demagnetizing magnetostatic selfinteraction, $\mu_o \boldsymbol{M}(\mathrm{r})\cdot\boldsymbol{H}_d(\boldsymbol{M}(\mathrm{r}))/2$. Here $\boldsymbol{H}_d$ contains a uniform demagnetizing-field contribution $H_u = -H_u\boldsymbol{e_z}$ and a non-uniform or flower-state contribution perpendicular to $\boldsymbol{e}_z$. For particle $R < R_{coh}$, the flux closure due to magnetostatic-selfinteraction is absent. The non-uniform or flower-state contribution self-interaction is perpendicular to $\mathbf{e_z}$ i.e. $|S_{xy}(\boldsymbol{r})| = \sin\Theta$, given by additional demagnetization term as:

$$\boldsymbol{H}_F.\boldsymbol{S} = M_s\,H_F\sin\Theta \qquad (13)$$

hence Eq. (12) with flower state energy correction is given by:

$$<\eta> = \left[\frac{A}{R^2}\sin\Theta^{\,2} + K\sin\Theta^{\,2} + \frac{1}{2}\,\mu_o\,H\,M_s\sin\Theta^{\,2} - \mu_o\,M_s\,H_F\sin\Theta \right] \qquad (14)$$

with the assumption of small Θ and find:

$$<\eta> = \left(\frac{A_e}{R^2} + \left(K + \frac{\mu_o}{2} M_s H\right)\right) (\sin^2\Theta) - \mu_o M_s H_F \sin\Theta. \quad (15)$$

As usual, the exchange stiffness A_e parameterizes the interatomic exchange, $\eta_A = A_e(\nabla \boldsymbol{S})^2$, whereas K is the uniaxial anisotropy of the particles, which are assumed to be *c*-axis aligned in the z-direction. This K includes both magnetocrystalline (K_1) and shape-anisotropy contributions. There are three magnetostatic terms in Eq. (10), namely the Zeeman interactions with the external magnetic field H, the magnetostatic selfinteraction energy described by the demagnetizing factor D which give the flux closure, and the flower-state energy correction (H_F) due to the nonuniform magnetization inside the particles. The spin texture due to flux closure, i.e., curling state is absent in small particles ($R < R_{coh}$). Overall, the flower state reduces the selfinteraction energy compared with the homogeneous state, which is accounted for using an energy correction $\mu_o M_s H_F \sin\Theta$, where H_F is assumed a positive constant. The field H_F parameterizes the interaction of the nanoparticle spins with the in-plane component of the demagnetizing field inside the nanoparticles. This field is zero for homogeneously magnetized ellipsoids but nonzero for magnetized particles of arbitrary shape (see Fig. 3.2) where it gives rise to flower-state spin structures such as those in Figs. 3.2(d-f). The parameter H_F depends on the shape of the particles, especially on the cross-section, but is generally comparable to but somewhat smaller than the saturation magnetization M_s. To find the stable state, we minimize $<\eta>$ using Eq. (15) with respect to Θ. Equation (15) is quadratic in sinΘ, and therefore easily minimized. Explicitly, one has:

$$\sin\Theta = \frac{\mu_o M_s H_F}{\frac{A_e}{R^2} + 2K + \mu_o M_s H} \tag{16}$$

in Eq. (16), H_F is positive, meaning that the magnetization has a component pointing away from the symmetry axis. Essentially, larger Θ increases the exchange energy and anisotropy energy but decreases the Zeeman energy and the selfinteraction energy. It is also clear that when H is large enough, sinΘ diverges, corresponding to the magnetization reversal.

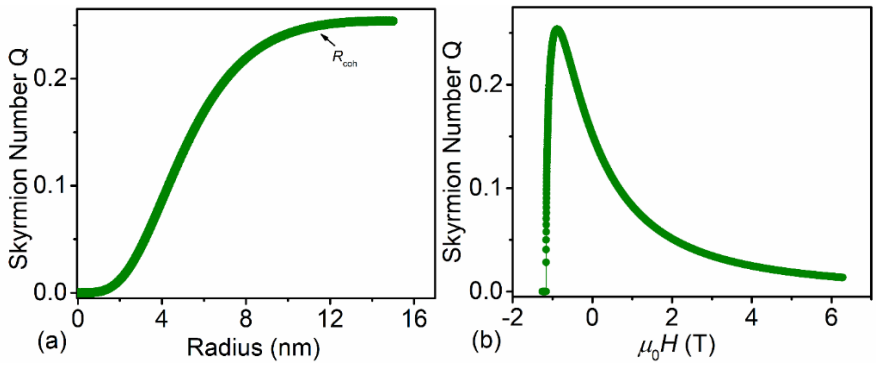

Figure 3.3. Skyrmion number in very small particles: (a) particle-size dependence and (b) field dependence. In (a), the plots are in the absence of an external magnetic field, whereas in (b) the plots are in a reverse field. In (a) at the maximum value where the skyrmion number is constant represent i.e., $R = R_{coh}$ where flower state vanishes, and curling mode appears.

The Berry curvature can be calculated accordingly using Eq. (1) using $\boldsymbol{S}(\boldsymbol{r})$. The integration of Berry curvature over the entire magnetic particles gives the Skyrmion number Q. We plotted the skyrmion number as a function of particle size at zero magnetic fields and as a function of magnetic field for a particle of size 10 nm. Figure 3.3(a) shows the change in skyrmion number as a function of particle size. The striking feature in Fig. 3.3(a) is that the skyrmion number is almost zero for very small particles, rapidly increases at a certain size, and slowly converges to a limiting curve. While the corresponding transition size depends on the micromagnetic parameters, the overall trend

can be qualitatively understood using Eq. (16). It can be shown that the Skyrmion number for a cylindrical particle is:

$$Q = \frac{\cos\Theta_c - \cos\Theta_\infty}{2} \tag{17}$$

where Θ_c and Θ_∞ are the polar angles of $\boldsymbol{S}$ at the center and far away. In the flower state discussed here, $\Theta_c = 0$ and $\Theta_\infty = \Theta$. One can calculate the skyrmion number from Θ in Eq. (16), which clearly shows that $\Theta \to 0$ when $R \to 0$. Eq. (16) also shows that Θ saturates when $R \to \infty$. Microscopically, since the exchange term (A_e) is proportional to $\sin^2\Theta$, it tends to suppress the magnetization gradients (spin tilt). This suppression is most effective in small particles since the exchange energy is proportional to $\frac{A_e}{R^2}$.

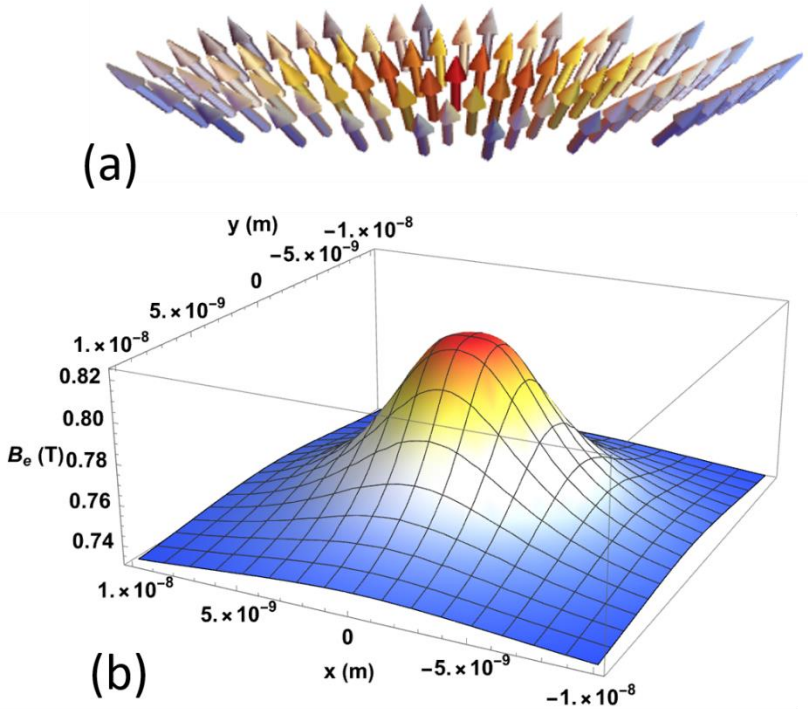

Figure 3.4. (a) Vectro3d plot for flower state in Eq. 3. At the center, the spin is directed in upward direction, (b) emergent magnetic field due to flower state in cylinder of radius 10 nm.

Figure 3.3(b) shows the skyrmion number as a function of the magnetic field. The high-field Q is very small but nonzero, except for aligned ellipsoids where $Q = 0$ due to the absence of the edges or corners. In principle, the high field state is still a flower state like those in Fig. 3.2(d-f), but Θ is so small that they are close to uniform magnetization shown in Fig. 3.2(b-c). In Fig 3.3(b) the skyrmion number achieves the maximum value just before the magnetization reversal. Positive and negative magnetic fields align and misalign the magnetization, respectively, and the latter, which amounts to increasing lengths of the blue arrows in 3.2(d-f), is plotted in Fig. 3.3(b).

Fig. 3.4 shows the vector 3d plot for flower state [Fig. 3.4(a)] and emergent magnetic field [Fig. 3.4(b)] due to flower state in cylindrical nanoparticle. The emergent magnetic field which is proportional to the Berry curvature gives rise to THE. Figures 3.3 and 3.4 have important implications for the experimental and numerical investigation of THE in nanoparticles, which is proportional to the Skyrmion density or Berry curvature.

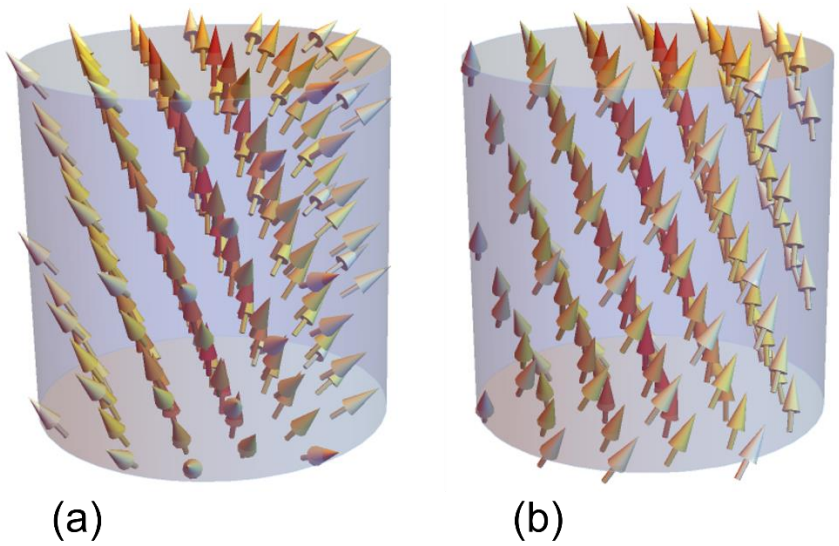

Figure 3.5. Vector 3d plots in cylinder: (a) flower state (b) curling state.

3.5 Magnetization Curling

In reality, exchange interatomic (A_e) favors magnetization uniformity but competes against other energy contributions, such as magnetostatic energies. Magnetostatic interactions favor flux closure ($\nabla \cdot \boldsymbol{M} = 0$) over magnetic poles ($\nabla \cdot \boldsymbol{M} \neq 0$), and this principle manifests in the existence of a curling mode during nucleation and with the increase of the size of nanoparticle [11, 29]. This flux closure reduces the magnetostatic energy and therefore yields a nonzero azimuthal component to magnetization to the perpendicular component. Therefore, magnetization reversal in ellipsoids and cylinders having radii larger than R_{coh} leads to magnetization curling/vortex as long as the size in single domain limit ($R_{\text{coh}} < R < R_{\text{SD}}$) [29] and the energy correction (H_F) giving flower state is absent. Curling is a special vortex state, occurring in the intermediate vicinity of the nucleation field during the magnetization reversal and R_{coh} and being symmetric around the z-axis. The curling mode, which has the symmetry of Fig. 3.2(g-h), is one of the few exact solutions in many-body physics [10, 21]. The question, therefore, is how the curling mode yields a topological Hall effect and how this effect depends on the particle. Our interest is to study the skyrmion density at the nucleation field and particles with a radius slightly greater than R_{coh}.

The curling mode is defined by a small perpendicular magnetization components $|\boldsymbol{S}_{xy}(\boldsymbol{r})|<<1$. As the size of nanoparticles or the reverse magnetic field increase, $|\boldsymbol{S}_{xy}(\boldsymbol{r})|$ increases, and the magnetic state eventually becomes the curling/vortex state. Due to the flux closure, the curling state does not require the correction to the selfinteraction energy as introduced in the flower state, i.e., $H_F=0$ and the demagnetization fiend $\mathbf{H}_d(\mathbf{M}(\mathrm{r}))$ provides the magnetostatic selfinteraction for flux closure. As the size of the particle

increases, flux closure due to magneto-static self-interaction gives rise to curling mode. Recall in the curling state, $\Theta(\boldsymbol{r})= \varphi \pm \pi/2$, Eq. (3) can be rewritten as:

$$\boldsymbol{M}(\boldsymbol{r}) = M_s \left(S_z \mathbf{e}_z + S_{xy}(r)\mathbf{e}_P\right) = \left(S_z \mathbf{e}_z - S_{xy}(r)\sin\phi\, \boldsymbol{e}_x + S_{xy}(r)\cos\phi\, \boldsymbol{e}_y\right) \tag{18}$$

And the energy equation is given by eq. (2):

$$\mathscr{E} = \int \left[A\,(\nabla \boldsymbol{S}_{xy}(\boldsymbol{r}))^2 + K\,(\boldsymbol{S}_{xy}(\boldsymbol{r}))^2 + \frac{1}{2}\,\mu_o\,(H - \mathrm{D}\,M_s)\,M_s\,\boldsymbol{S}_{xy}(\boldsymbol{r})^2] \right] \mathrm{d}V \tag{19}$$

The energy

$$\mathscr{E} = \int \eta \,\mathrm{d}V \tag{20}$$

is minimized by Euler Lagrange equation such that

$$\left[\frac{\delta \eta}{\delta\, \boldsymbol{S}_{xy}\,(\mathrm{r})} = -\nabla\left(\frac{\partial \eta}{\partial \nabla\, \boldsymbol{S}_{xy}\,(\mathrm{r})}\right) + \frac{\partial \eta}{\partial\, \boldsymbol{S}_{xy}\,(\mathrm{r})} \right]. \tag{21}$$

The equation of state obtained by minimizing the total energy eq. (19) with respect to $S_{xy}(\boldsymbol{r})$ [10]

$$(2A_e\nabla^2 - 2K_1 - \mu_0 M_s H + \mu_0 D M_s^2\,)\boldsymbol{S_{xy}}(\boldsymbol{r}) = 0 \tag{22}$$

where we used $\nabla(A\nabla\, \boldsymbol{S}_{xy}) \approx A\,\nabla^2\, \boldsymbol{S}_{xy}$. In Eq. (9), $\boldsymbol{H}_d = -D\mathbf{M}$ where D is the demagnetization factor addition giving flux closure. The curling mode considered by Frei [19] can be written by using small-angle approximation. Brown considered the exact solution of specific micromagnetic problem under the cylindrical symmetry, i.e., $S_{xy}(\boldsymbol{r})= S_{xy}(\rho)$ [9, 10]. Hence

$$M(r) = M_s\left[-S_{xy}(\rho)\,\sin(\phi)\,\boldsymbol{e_x} + S_{xy}(\rho)\,\cos(\phi)\,\boldsymbol{e_y} + S_z\boldsymbol{e_z}\right] \tag{23}$$

where $S_{xy} = \sin\Theta$ and $S_z = \cos\Theta$. Because it is Eigen function of differential eq. (22), substituting the curling mode considered in Eq. (23) in micromagnetic Eq. (22) leads to:

$$\left(\rho^2\frac{\partial^2}{\partial\rho^2} + \rho\frac{\partial}{\partial\rho} + ((\mathrm{k}\rho)^2 - 1)\right)S_{xy}(\rho) = 0 \tag{24}$$

where $k^2 = -\left(\frac{2K_1 + \mu_0 M_s H - \mu_0 M_s^2 D}{2A_e}\right)$. Eq. (24) is Bessel equation and therefore, we can write the curling mode in the cylinder $S_{xy}(\rho) = J_1(k\rho)$ or $\sin\Theta \approx \Theta(\rho) = J_1(k\rho)$. The boundary condition is modified as $\frac{\partial J_1(k\rho)}{\partial \rho}|_{\rho=R} = 0$. This boundary condition is possible only when $kR = q_1 = 1.841$. In addition, in spherical particles with $D = 1/3$, the curling mode can be described by a spherical Bessel function, $S_{xy}(\rho) = j_1(k\rho)$ with the smallest root $kR = q_2 = 2.0816$. The skyrmion density due to magnetization curling in cylinder and sphere was calculated by using Eq. 1 as:

$$\Psi_{cylinder} = \frac{J_1(k\rho)\partial J_1(k\rho)}{\rho \quad \partial \rho} \tag{25}$$

$$\Psi_{sphere} = \frac{j_1(k'\mathrm{r})\partial j_1(k'\mathrm{r})}{\mathrm{r} \quad \partial \mathrm{r}} \ . \tag{26}$$

Figure 3.5(b) and 3.6(a) shows the curling mode vector 3d plot in a cylinder using $J_1(k\rho)$. Figure 3.5(b) shows that emergent magnetic field within the cylinder due to curling mode. At the boundaries of the cylinder, the Berry curvature vanishes. Berry curvature is the maximum at the origin of the cylinder. The skyrmion number is obtained by integrating the Berry curvature in limits of 0 to R, where R is the radii of the cylinder or sphere provided that $R > R_{coh}$:

$$Q_{\text{cylinder}} = \frac{1}{2} J_1(kR)^2 \tag{27}$$

$$Q_{\text{sphere}} = \frac{1}{2} j_1(kR)^2 \ . \tag{28}$$

In a high magnetic field, the particle will show a flower state with a small Θ, which corresponds to a small skyrmion number or emergent magnetic field. At the nucleation field, $H = H_n$, flower state turns into a curling state. The skyrmion number and hence the

emergent field and THE will jump to a large value. These observations are shown in micromagnetic simulations in next section. The nucleation field at which the curling appears is given by [21]:

$$H_n = \frac{2K_1}{\mu_0 M_s} - DM_s + \frac{2A_e q_i^2}{\mu_0 M_s R^2} \tag{29}$$

where $q_1 = 1.841$, $D = 0$ for the cylinder and $q_2 = 2.0816$, $D = 1/3$ for the sphere. The nanoparticle with curling will give a sudden jump in THE at the nucleation field. We will have a finite skyrmion number or THE at the nucleation field as shown in simulations. In the flower state, we do not have any nucleation field so for that case we do not have any jump change in the skyrmion number. In a cylinder of radii "*R"* the boundary condition gives $kR = q_1 = 1.841$ and $Q_{\text{cylinder}} = 0.17$; for sphere one has $k'R = q_2 = 2.0816$ and $Q_{\text{sphere}} = 0.11$. This skyrmion number will increase as a function of the field after the nucleation field until we have a sudden magnetization reversal. For the fixed value of $R > R_{coh}$ where curling appears Q has a constant value. It's because the curling mode is subject to the eigenvalue condition $kR = 1.84$ so $Q = 0.5J_1(1.84)^2 = 0.17$. This also applies to the following two considerations. The $J_1(kr)$ oscillations describe radial spin waves. The curling mode is a 1s state in the analogy of an electron in a cylinder, where the lowest-lying excited radial spin-wave mode is a 2s state and has $kR = 5.33$ and Q = 0.06 showing the Berry curvature of electron scattering from excited states is tricky from the viewpoint of dynamics [21].

For larger values of radii R, $\boldsymbol{S}_{xy}(\boldsymbol{r})$ becomes larger and eventually the curling mode turns into a vortex mode. As the size of the nanoparticle increases the long-range magnetostatic interaction between $\boldsymbol{M}(\mathbf{r})$ and $\boldsymbol{M}(\mathbf{r}')$ gives rise to in-plane spin configurations. Due to the

increase in size, the magnetostatic self-interaction has a higher magnitude compared with the short-range exchange interactions.

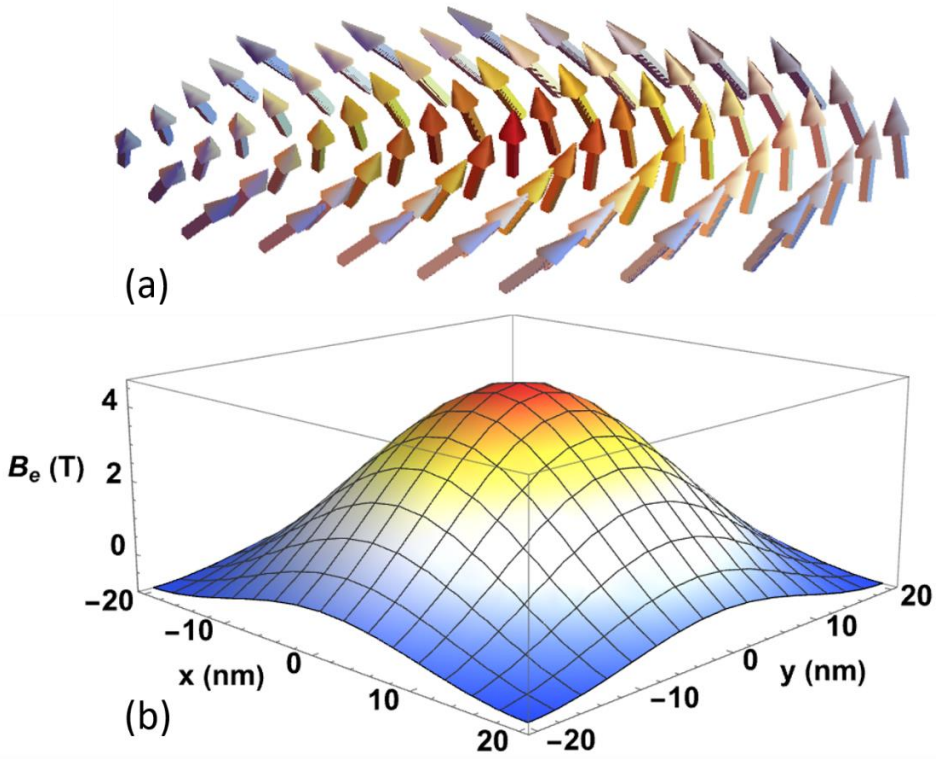

Figure 3.6. (a) Vectro3d plot for curling mode using exact curling mode Eq. 23. At the center the spin is directed in upward direction, (b) emergent magnetic field due to curling mode in cylinder of radii 20 nm.

3.6 Micromagnetic Simulations

The micromagnetic simulations are performed near R_{coh} using OOMMF-based software *ubermag* [22]. The parameters which we used for simulations are $M_s=1.2\times10^6$A/m, $A_e=1\times10^{-11}$J/m, $K_1=0.2$MJ/m^3, $l_o = (A_e/\mu_o M_s^2)^{1/2}$. In all cases, cell size is considered smaller than the exchange length. For simulation, we considered ferromagnetic cubes, cylinders, and spheres with uniaxial anisotropy. We changed the radii of the cylinder and sphere and simulated the skyrmion number for different radii.

Our results show that as the size increased the skyrmion number Q for the flower state also increases. We calculated the skyrmion number for a size lower than critical single-domain size i.e., $R < R_{coh}$. The flower-state spin structure is well established and used as a standard problem in micromagnetism [17, 16, 29, 30]. The simulation results show that the flower state only exists in either cylinder or a ferromagnetic cube. In the sphere, the flower state does not open due to a small edge effect i.e., $H_F = 0$.

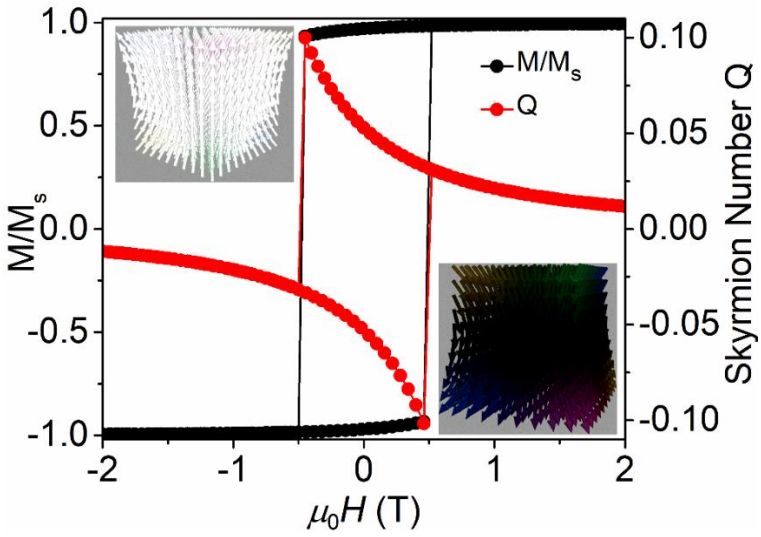

Figure 3.7. Magnetization and Skyrmion number in ferromagnetic cube with $L < L_{coh}$: Skyrmion number Q as a function magnetic field during magnetization reversal. The deviation from the saturation clearly appears just before the reversal.

Figure 3.7 shows the Skyrmion number hysteresis and normalized magnetization as a function of the decreasing magnetic field $B(T)$ in a cube of $L > L_{coh}$. This indicates the presence of a flower state, which appears during magnetization reversal. The skyrmion number changes the sign at the reversal indicating the change of magnetization $+M_z$ to $-M_z$. At the maximum value of the skyrmion number, the magnetization is some fraction of $\pm M_s$ (which is the minimum value of magnetization just before reversal). The sign of Q flips when the field is applied from B_{max} to $-B_{max}$. Q achieves maximum value

just before the reversal (the point where we have a minimum value of magnetization) close to the coercivity field.

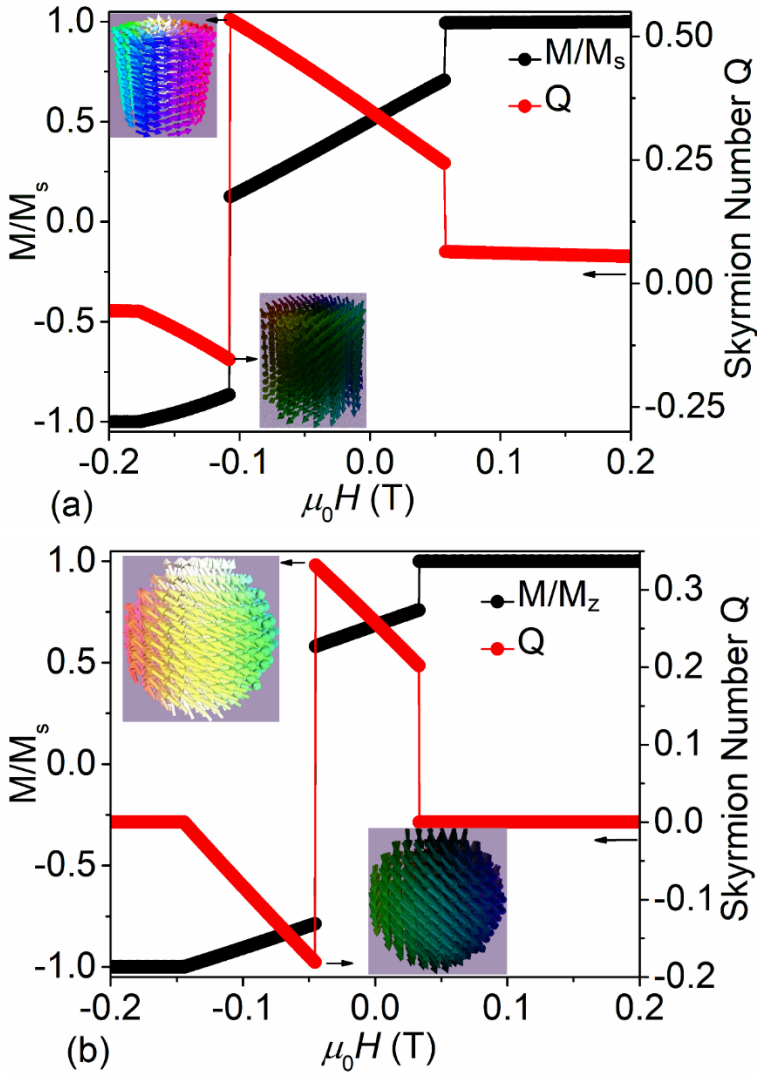

Figure 3.8. Magnetization and Skyrmion number in ferromagnetic (a) cylinder (b) sphere for $R > R_{coh}$.

As the nanoparticles size increases, i.e., $R > R_{coh}$, the magnetization reversal involves the presence of curling mode. For cylinder and cubes, the spin texture first involves the presence of a flower state then at some magnetic field the spin texture change to a curling/vortex state with core polarity in p = +1. At the magnetization

reversal the polarity changes to p = -1 with curling mode. At the high field, the curling mode disappears and gives rise to a flower state with polarity pointing in the direction of magnetization. In other words, we can say that in nanoparticles with non-coplanar and noncollinear spin texture the core polarity is directed in the direction of magnetization which is the opposite of the case of a conventional skyrmion in materials [31]. Micromagnetic simulation for cylinder (Fig 3.8(a)) and sphere (Fig. 3.8(b)) for radius $R > R_{coh}$ shows the presence of curling which appears during magnetization reversal. The absence of THE contribution in the sphere at a high magnetic field indicates the absence of a flower state in the sphere as compared with the cylinder which has a finite skyrmion number when curling mode disappears indicating the effect of edges i.e. $H_F \neq 0$.

3.7 Experimental Studies of Magnetic Vortex

To study the single domain state we carried out magnetic force microscopy (MFM) measurements on circular dots of Co that give evidence for the presence of a vortex state with a perpendicular magnetization core. Samples of Co ferromagnetic dots were made by using electron-beam lithography and evaporation in an ultrahigh vacuum using an electron-beam gun. The circular nanodot patterns were defined on thermally oxidized Si substrates with positive resists. The bilayer positive resists PMMA950/MMA EL6 was exposed to an electron beam and the liftoff method was used to create the circular pattern. Ordered Co circular arrays were fabricated, in a trilayered structure of Ti/Co/SiO_2 were fabricated. The circular layered structure was grown by e-beam evaporation in a UHV system. The base pressure was in the range of 1×10^{-8} torr. The evaporation pressure is less than 5×10^{-7} torr. The thickness is in the range of 10-15 nm for Ti and ~50 nm for Co, and SiO_2 layer to prevent oxidation. The thickness was

monitored during growth by a quartz balance for each layer. By a lift-off process, the resist is removed and dots with designed sizes remain on top of the Si surface.

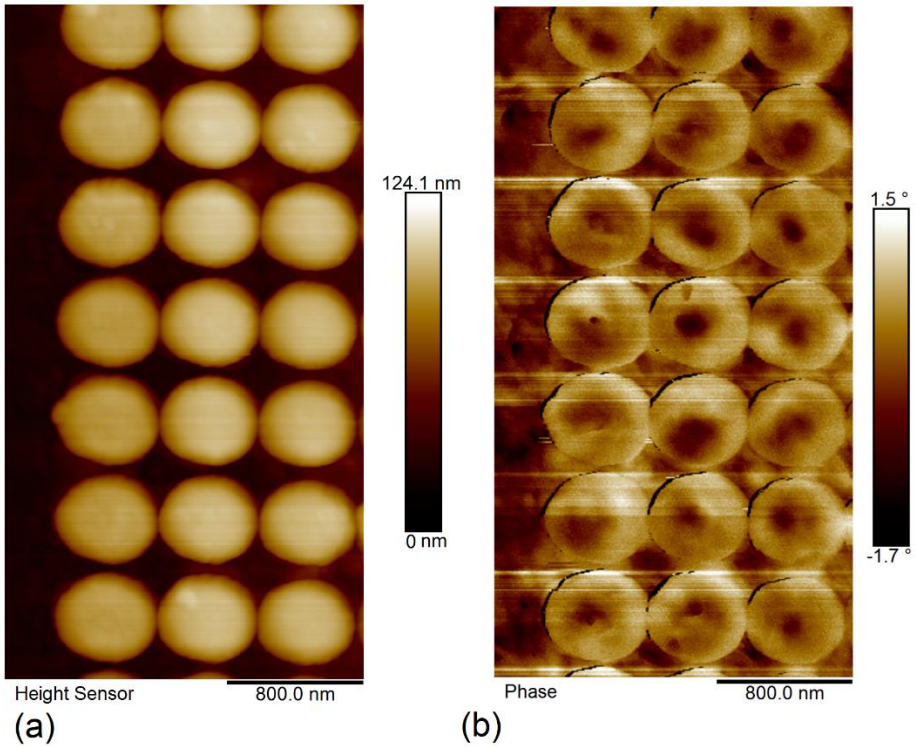

Figure 3.9. (a) AFM for pattern of circular nanodots (b) MFM of circular nanodots showing precence of single domain vortex states.

In MFM, the instrument was operated in ac mode to detect the magnetic force acting between the cantilever tip and the surface of the circular dots in ambient condition. To minimize the stray-field effect, the low moment CoCr tip was used. The distance between the surface and the tip was between 30 nm. The MFM and AFM images are shown in Figs. 3.9 & 3.10. The MFM images for most of the circular nanodots show clear contrast between the center and the surrounding. These MFM images show that the spins in the dots align parallel to the plane and at the dark spot, the spin aligns perpendicular to the plane. The area of the dark region is very small for vortex in permelally [18, 32] but the anisotropy of Co is large making it a semi-hard magnet. This gives rise to a

significantly large area for the dark spot in the middle of the single-domain magnetic state. These direct imaging of single domain states in Co are done for the 1st time. When the dot thickness becomes much smaller than the dot diameter, usually all spins tend to align in-plane giving vortex. Our micromagnetic simulation Fig. 3.10(c) for Co nanodisk also shows that the Co disk of up to 500 nm exhibit magnetic vortex state.

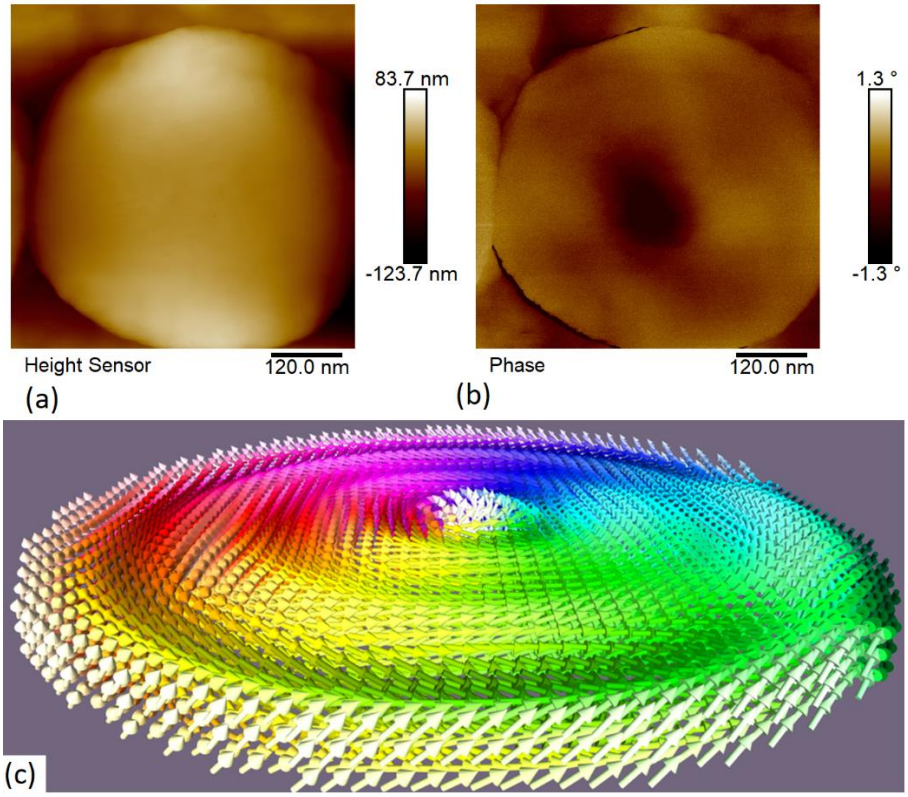

Figure 3.10. (a) AFM for a pattern of circular nanodots, (b) MFM of circular nanodots showing magnetic vortex core observation in circular Dots, and (c) Micromagnetic simulation of Co nanodot of 500 nm diameter showing the presence of vortex state.

Our micromagnetic simulation in Fig. 3.8(a) and 3. 11 shows that for particle with radius $R_{coh} < R < R_{SD}$, where R_{SD} is the radius of single domain, constitute two sates at different magnetic field. At very high field the presence of finite skyrmion number is due to flower states, while at low field, it represents the curling/vortex like spin textures. So,

we also applied an external magnetic field of 1-tesla perpendicular to the plane using permanent magnets. The image in Fig. 3.12 shows that the vortex-like state disappears and most of the spin aligns in the direction of the field except at the edges where the spins are slightly tilted showing the edge effects of the flower state for the spins.

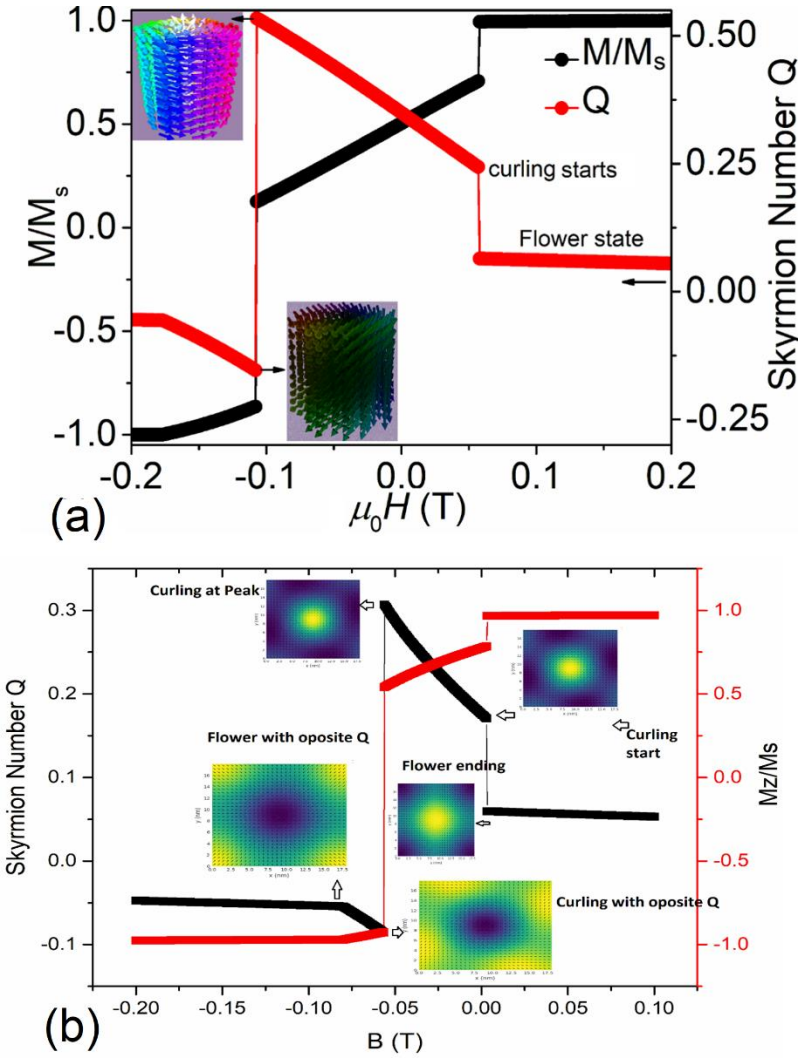

Figure 3.11. Bird view: Reversal in magnetic nanodot with radius/length greater than coherence radius/length. (a) Cylinder (b) Cube. At a high magnetic field, the spins align in the direction of the external field giving a finite skyrmion number due to flower state. But at the nucleation field due to flux closure, the skyrmion number jumps to a higher value representing the flux closure state.

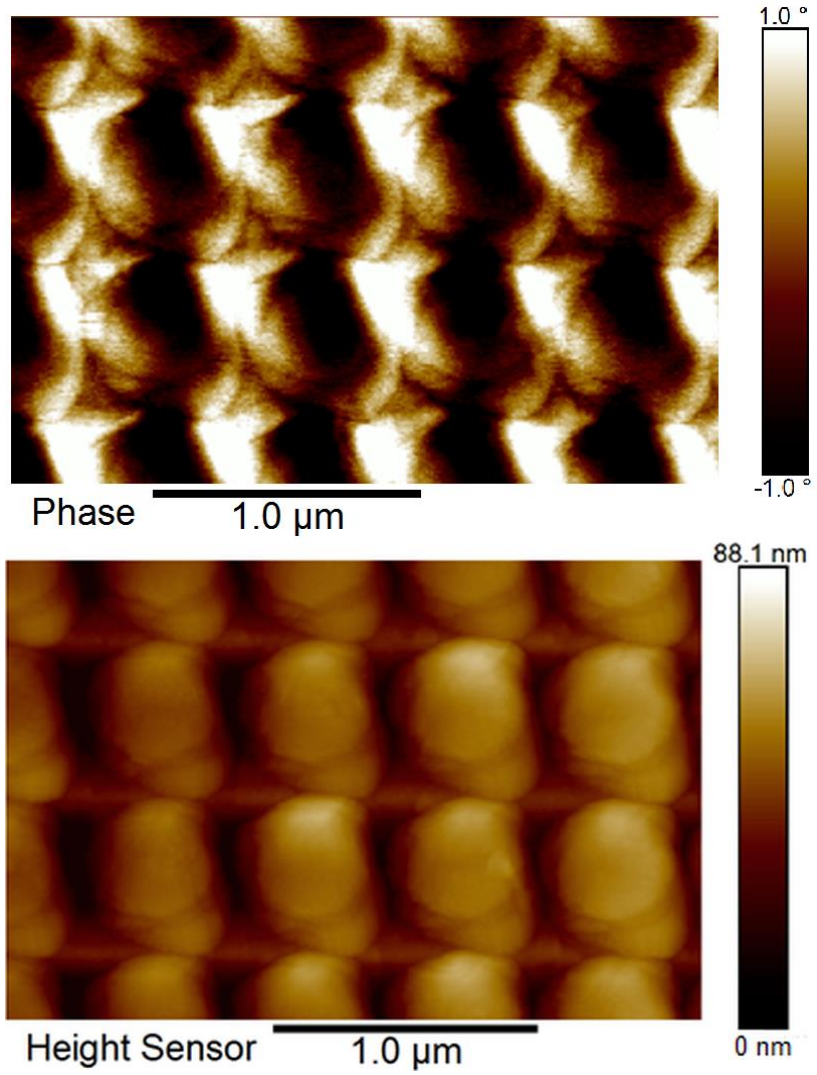

Figure 3.12. Magnetic nanodots arrays in the presence of magnetic field showing magnetic vortex state desapear and showing the presence of tilted spin at the edges.

3.8 Conclusions

We calculated the spin structure $\boldsymbol{S}(\boldsymbol{r})$ and the resulting Skyrmion numbers using micromagnetic models. Our calculations reveal a complex Berry curvature and topological Hall-effect scenario in the nanoparticles. The distinction is between ellipsoidal (spherical) and nonellipsoidal (cubic and cylindrical) nanoparticles, the latter

exhibiting flower-state contributions to the Hall effect. We studied finite Skyrmion density due to flower states and curling mode both analytically and using micromagnetic simulations. Very small grains have an approximately uniform magnetization, whereas in somewhat bigger grains flower-state, curling, and vortex state appears which gives rise to finite Berry curvature. These results can be very useful for the study of the Hall effect due to the emergent magnetic field, which has a finite value associated with the topological spin texture. These contributions can be potentially realized experimentally, for example by embedding individual magnetic particles in a nonmagnetic metallic matrix.

References

[1] M. V. Berry, Proc. R. Soc. Lond. A **392**, 45-57 (1984).

[2] D. Xiao, M.-Ch. Chang, and Q. Niu, "Berry phase effects on electronic properties", Rev. Mod. Phys. **82**, 1959 (2010).

[3] S. Seki and M. Mochizuki, Skyrmions in Magnetic Materials, Springer International, Cham (2016).

[4] N. Nagaosa and Y. Tokura, *Nature Nanotech*. **8**, 899 (2013).

[5] Y. Taguchi, Y. Oohara, H. Yoshizawa, N. Nagaosa, and Y. Tokura, Science **291**, 2573 (2001).

[6] J. Bouaziz, H. Ishida, S. Lounis, and S. Blügel, Phys. Rev. Lett. **126**, 147203 (2021).

[7] N. Kanazawa, M. Kubota, A. Tsukazaki,4 Y. Kozuka, K. S. Takahashi, M. Kawasaki, M. Ichikawa,1 F. Kagawa, and Y. Tokura, Phys. Rev. B **91**, 041122(R) (2015).

[8] A. S. Ahmed, J. Rowland, B. D. Esser, S. R. Dunsiger, D. W. McComb, M. Randeria, and R. K. Kawakami, Phys. Rev. Mater. **2**, 041401(R) (2018).

[9] William Fuller Brown, (Jr.) New York, London J. Wiley, (1963).

[10] A. Aharoni, *Introduction to the Theory of Ferromagnetism*, University Press, Oxford 1996.

[11] R. Skomski, Journal of Physics: Condensed Matter, 15, R841-R896 (2003).

[12] W. Zhang, B. Balasubramanian, A. Ullah, R. Pahari, X. Li, L. Yue, Shah R. Valloppilly, A. Sokolov, R. Skomski, and David J. Sellmyer, Appl. Phys. Lett. **115**, 172404 (2019).

[13] A. Ullah, X. Li, Y. Jin, R. Pahari, L. Yue, X. Xu, B. Balasubramanian, David J. Sellmyer, and R. Skomski, Phys. Rev. B **106**, 134430 (2022).

[14] R. Pahari, B. Balasubramanian, A. Ullah, P. Manchanda, H. Komuro, R. Streubel, C. Klewe, S. R. Valloppilly, P. Shafer, P. Dev, R. Skomski, and D. J. Sellmyer Phys. Rev. Materials **5**, 124418 (2021).

[15] K. Niitsu, Y. Liu, A. C. Booth, X. Yu, N. Mathur, M. J. Stolt, D. Shindo, S. Jin, J. Zang, N. Nagaosa and Y. Tokura, Nature Materials **21**, 305–310 (2022).

[16] W. Rave, K. Fabian, A. Hubert JMMM **190** 332-348 (1998).

[17] M. E. Schabes and H.N. Bertram J. Appl. Phys. **64**, 1347 (1988).

[18] T. Shinjo, T. Okuno, R. Hassdorf, K. Shigeto, and T. Ono, Magnetic vortex core observation in circular dots of permalloy, Science **289**, 930 (2000).

[19] E. H. Frei, S. Shtrikman, and D. Treves Phys. Rev. **106**, 446 (1957).

[20] R. Skomski, H.-P. Oepen, and J. Kirschner, "Micromagnetics of ultrathin films with perpendicular magnetic anisotropy", Phys. Rev. B **58**, 3223-3227 (1998).

[21] R. Skomski, J. P. Liu and D. J. Sellmyer Phys. Rev. B **60** 7359 (1999).

[22] M. Beg, M. Lang, and H. Fangohr, IEEE Trans. Magn. 58, 7300205 (2022).

[23] F. Bloch, Zs. f. Phys. **74**, 295 (1932).

[24] L. D. Landau and E. M. Lifshitz, On the theory of the dispersion of magnetic permeability in ferromagnetic bodies, Phys. Zs. Sowjet. 8, 153 (1935) [Reproduced in Ukr. J. Phys. 53 Special Issue, 14 (2008)].

[25] C. Kittel, Theory of the structure of ferromagnetic domains in films and small particles, Phys. Rev. **70**, 965 (1946).

[26] S. Chikazumi, Physics of Magnetism (New York: Wiley 1964).

[27] R. Skomski, Simple Models of Magnetism (University Press, Oxford, 2008).

[28] R. Skomski, P. Manchanda, P. Kumar, B. Balamurugan, A. Kashyap, and D. J. Sellmyer, "Predicting the Future of Permanent-Magnet Materials" (invited), IEEE Trans. Magn. 49, 3215 (2013).

[29] E. Pinilla-Cienfuegos, S. Mañas-Valero, A. Forment-Aliaga, and E. Coronado, ACS Nano **10**, 1764 (2016).

[30] C. Gatel, F. J. Bonilla, A. Meffre, E. Snoeck, B. Warot-Fonrose, B. Chaudret, L.-M. Lacroix, and T. Blon, Nano Lett. **15**, 6952 (2015).

[31] B. Balasubramanian, P. Manchanda, R. Pahari, Z. Chen, W. Zhang, S. R. Valloppilly, X. Li, A. Sarella, L. Yue, A. Ullah, P. Dev, D. A. Muller, R. Skomski, G. C. Hadjipanayis, and D. J. Sellmyer, Phys. Rev. Lett. 124, 057201 (2020).

[32] X. H. Zhang, T. R. Gao, L. Fang, S. Fackler, J. A. Borchers, B. J. Kirby, B. B. Maranville, S. E. Lofland, A. T. N'Diaye, E. Arenholz, A. Ullah, J. Cui, R. Skomski, I. Takeuchi J. Magn. Magn. Mater. 560, 169627 (2022).

Chapter 4 Topological Phase Transitions and Berry-Curvature in Exchange-Coupled Nanomagnets

4.1 Introduction

Topological phase transitions (TPTs) permeate areas such as superfluid and superconductors [1, 2], basic quantum mechanics [3, 4], fractional quantum-Hall effect [5], and topological insulators [6] and therefore have gained significant interest in both science and technology. TPTs are very different from ordinary Landau-type phase transitions [4, 7-9]. Rather than involving symmetry breaking and order-parameter changes, they are characterized by changes in topological numbers. For example, coffee cups have one hole, located in the handle, and are therefore characterized by the topological number (Euler genus) $g = 1$. A flat pancake has no holes ($g = 0$) so that the piercing of a number of holes into a pancake is a trivial example of a TPT.

Topological phase transition is in contrast to magnetic hysteresis, which is based on a phase transition between an ordered low-temperature and a disordered high-temperature [1-6, 10, 11, 12]. An intriguing aspect of magnetic hysteresis is its relation to magnetic phase transitions. Figures 4.1(a-b) compare the atomic-scale origin of ferromagnetism with the nanoscale or 'micromagnetic' origin of hysteresis. When a ferromagnet is cooled below the Curie temperature T_c, it develops a spontaneous magnetization M_s (a). This process is a Landau-type phase transition, defined as a singular change of a local order parameter (M) due to spontaneous symmetry breaking. The ordered phase has the character of a $k = 0$ Goldstone mode whose magnetization can point in any direction (a). This degeneracy is removed by symmetry-*violating* terms in the Hamiltonian, such as magnetic anisotropy [13].

Magnetic hysteresis, Fig. 4.1(b), is on top of the Landau transition (a). When a magnetic material is subjected to an external field H, then its magnetization $M(H)$ is generally not single-valued but splits into ascending and descending branches. A well-known example is small nanoparticles of volume V and anisotropy energy $K_1V\sin^2\theta$ in a magnetic field $H = H_z$. The color coding throughout this article is $M_z(\boldsymbol{r}) = +M_s$ (red), $M_z(\boldsymbol{r}) = -M_s$ (blue) and intermediate (yellow). For positive K_1, $\theta = 0$ (red) and $\theta = 180^o$ (blue) are energetically favorable but separated by an energy barrier K_1V ($\theta = 90^o$). This energy barrier needs some external field to be overcome and is therefore the reason for the hysteresis.

While topology has a long history, the idea of topological phase transition goes back to the Lifshitz transition [4, 7]. Figure 4.1(c) shows the *k*-space meaning of the Lifshitz transition in metals. Itinerant electrons fill the available electron states until the Fermi level is reached. The occupancy at the Fermi level (gray) depends on the number of electrons, and there are several scenarios that change the topological quantum number Q, such as external mechanical pressure and chemical addition of electrons. Each Fermi-surface region (gray) yields an integer contribution to Q, irrespective of the size and shape of the pocket. Topological concepts are now applied to many areas of physics, from skyrmions [7, 8, 13, 15, 16, 17- 20] to topological insulators and other quantum materials [21-30], all of them fascinating research topics in their own rights.

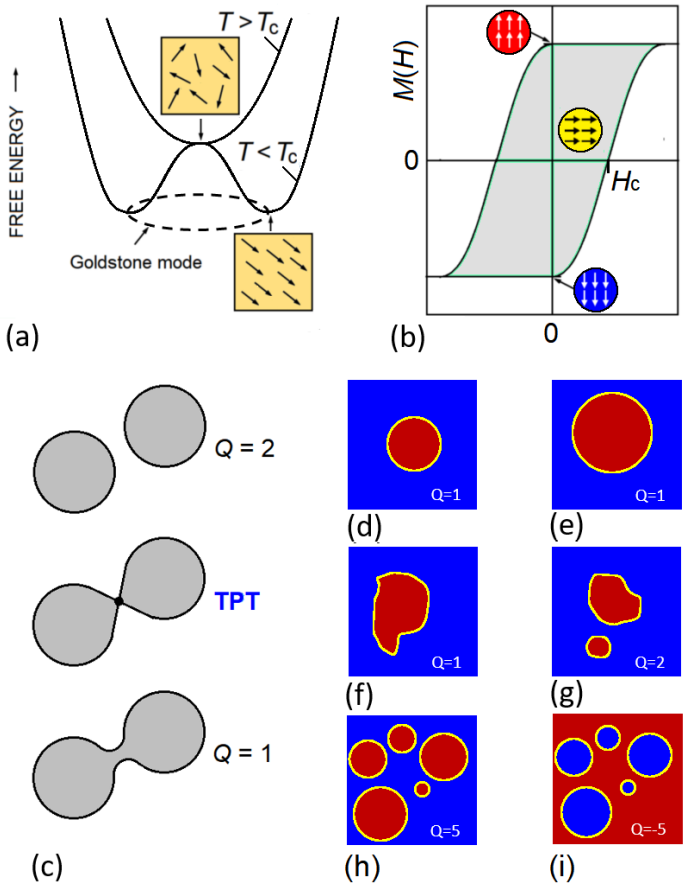

Figure 4.1. Phase transitions: (a) Curie transition (magnetic Landau transition), (b) magnetic hysteresis, (c) Lifshitz transition in metal, and (d-i) topological phase transition in a magnetic thin film with perpendicular anisotropy. In (c), the gray areas denote the *k*-space region occupied by electrons at the Fermi level. In (d-i), red and blue regions indicate positive (↑) and negative (↓) magnetizations with respect to the film plane. Topological phase transitions are characterized by topological numbers *Q*. The topological protection in the micromagnetic case is experimentally established, for example through the "blowing" of skyrmions [14 - 16].

Figures 4.1(d-i) show the magnetic analog of the Lifshitz transition in a thin film. The field *H* is perpendicular to the film and affects ↑ (red) and ↓ (blue) regions separated by domain walls (yellow). The underlying micromagnetism is very similar to that of magnetic skyrmions [31, 32, 33-36] and to XY-model transitions [8]. When an electrical

current flows through the film, then the spins of the conduction electrons exchange-interact with the local magnetization $\boldsymbol{M}(\boldsymbol{r})$ and become, in general, noncoplanar noncollinear. This noncollinearity creates a Berry curvature [5], an emergent magnetic field, and subsequently a Hall-effect contribution known as the topological Hall effect (THE) [5, 33]. These effects are proportional to the *skyrmion density* [31, 33, 37, 38]

$$\Phi = \frac{1}{4\pi}\,\boldsymbol{m}\cdot\left(\frac{\partial \boldsymbol{m}}{\partial x}\times\frac{\partial \boldsymbol{m}}{\partial y}\right) \tag{1}$$

where $\boldsymbol{m} = \boldsymbol{M}(\boldsymbol{r})/M_s$ is the normalized magnetization and the x-y-plane is the film plane. The emergent magnetic flux that corresponds to the THE is equal to $Q\,h/e$, where $Q = \int \Phi\, \mathrm{d}x\mathrm{d}y$ is the skyrmion number and h/e is the magnetic flux quantum. In granular thin films, there are also nonzero derivatives $\partial\boldsymbol{m}/\partial z$. By virtue of measurement geometry, $\partial\boldsymbol{m}/\partial z$ does not contribute to the THE [33], but it is one source of noise [39]. The skyrmion density is nonzero for spins $\boldsymbol{m}(\mathbf{r})$ that are both noncollinear and noncoplanar, and Eq. (1) is actually a continuum version of the triple product or spin chirality $\chi_s = \boldsymbol{m}_i\cdot(\boldsymbol{m}_j \times \boldsymbol{m}_k)$, where $\boldsymbol{m}_i = \boldsymbol{m}(\boldsymbol{R}i)$ describes the atomic spins that cause the conduction electrons to develop their Berry phase.

The topological Hall effect is measured in the film plane (x-y-plane), so that its prediction for a given micromagnetic spin structure $\boldsymbol{M}(\boldsymbol{r})$ requires the integration $Q = \int \Phi\, \mathrm{d}x\, \mathrm{d}y$, where Φ depends on $\partial\boldsymbol{m}/\partial x$ and $\partial\boldsymbol{m}/\partial y$, Eq. (1). There are also nonzero derivatives $\partial m(\boldsymbol{r})/\partial z$, but these do not contribute to the THE due to the measurement geometry. Inside the red and blue regions, the magnetization is therefore constant, so that $\Phi = 0$. We can therefore restrict the evaluation of Figs. 4.1(d-i) to the yellow boundary region. It is

convenient to divide the integration into two parts, namely perpendicular and parallel to the yellow boundary.

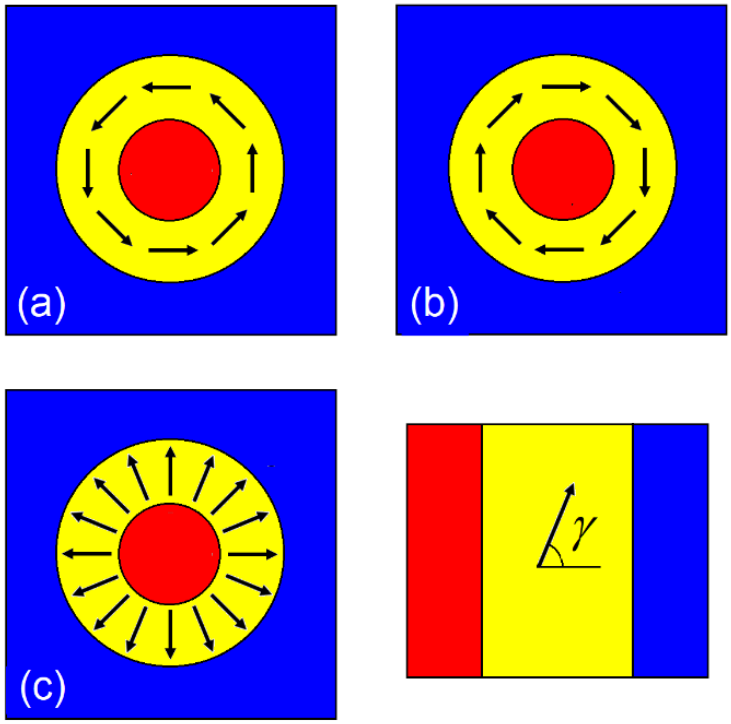

Figure 4.2. Chirality and vorticity: (a) Bloch wall with counterclockwise chirality, (b) Bloch wall with clockwise chirality, (c) Néel wall, and (d) angle γ of the spin direction. The THE depends on the vorticity only (red on blue background or blue on red background) but not on the angle γ, so that (a-c) yield $Q = +1$.

In skyrmionic structures such as those of Figs. 4.1(d-i), the spins inside the red and blue regions are parallel ($m = \pm e_z$), so that $\partial \boldsymbol{m}/\partial x$, $\partial \boldsymbol{m}/\partial y$, and Φ are zero. The integral over Φ therefore reduces to an integral over the yellow domain-boundary regions in Figs. 4.1(d-i). It can be shown that

$$Q = {}^{1}/_{2\pi} \oint \boldsymbol{\kappa} \,.\, \mathrm{d}\boldsymbol{l} \qquad (2)$$

where κ is the curvature of the region's yellow boundary and the integral in Eq. (7) has the value 2π [40]. This integral is equal to ±1 for any area enclosed by a single yellow

boundary [40]. While Eq. (2) is valid for arbitrary domain shapes, it requires domain walls free of internal singularities such as Bloch lines [33, 41]. Mathematically, $\boldsymbol{M}(\boldsymbol{r})$ is a fiber bundle [42] on the base space $\boldsymbol{r}$ and therefore locally flat but globally nontrivial [43]. In fact, Fig. 4.1(d-i) provides a simple example of a bulk-boundary equivalence, a feature that forms a cornerstone of topological physics [22]. The sign of Q depends on the vorticity [44] of the spin structure, that is, on whether the region enclosed by the yellow boundary is red (Q = +1) or blue (Q = -1). In particular, Q is independent of the clockwise or counterclockwise chirality of Bloch walls in the yellow region as shown in extended Fig 4.2.

As discussed above, TPTs do not increase or decrease order parameters but consist of changes in topological numbers. This leads to the question of whether such transitions lead to hysteretic features beyond magnetic hysteresis. This hysteresis was not recognized in earlier research, because available systems had micron-size rather than nanoscale feature sizes, which makes it very difficult to detect the Berry curvature in Hall-effect measurements.

4.2 Methods

4.2.1 Experimental Methods

An inert gas condensation-type cluster-deposition method, schematically shown in Fig: 4.3(a). First, Co nanoparticles were produced by a DC magnetron sputtering using a mixture of argon and helium with a power of 200 W in a gas-aggregation chamber. After the formation, the nanoparticles were extracted towards the deposition chamber and deposited as a dense film on a Si (100) substrate having a Hall bar. The base pressure of the gas-aggregation chamber was 6×10^{-8} Torr and the respective Ar and He flow rates

were maintained at 400 and 100 SCCM (standard cubic centimeter per minute), respectively. The pressure in the cluster-formation chamber during the deposition was 0.7 Torr.

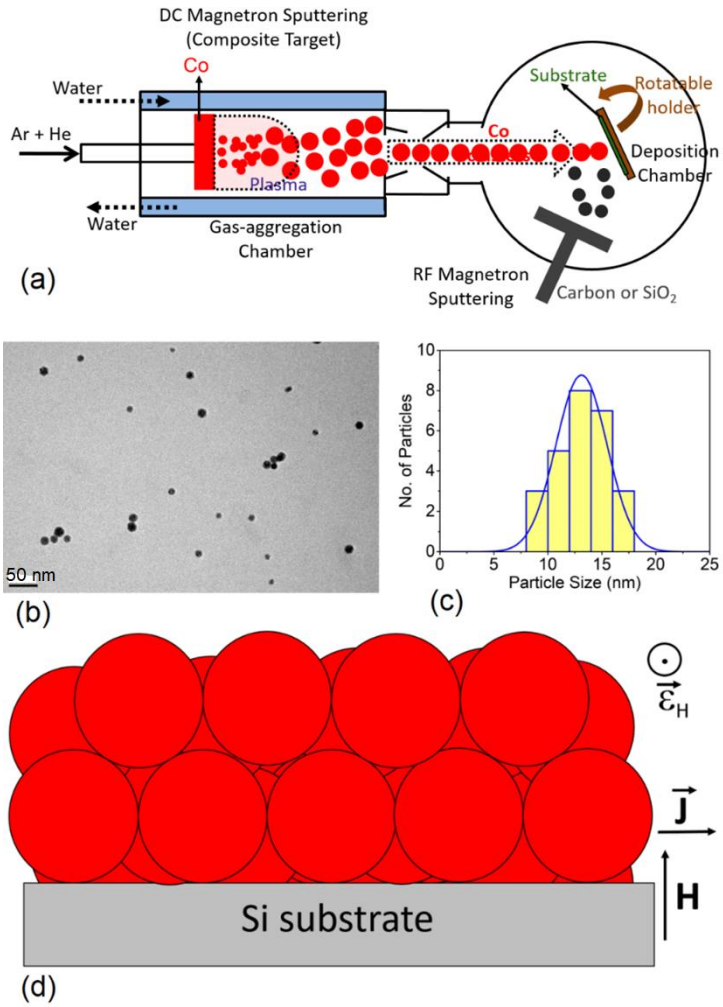

Figure 4.3. (a) A schematic of the cluster-deposition system. (b) Transmission electron microscope image and (c) the corresponding particle-size histogram. The result shows an average particle size d = 13.7 nm and a standard deviation $\sigma/d \approx 0.15$. (d) A schematic of a dense Co nanoparticle film used for magnetic and transport measurements.

The Co nanoparticles were deposited with a low coverage density on a thin carbon film supported by copper grids for transmission-electron-microscopy measurements using an FEI Technai Osiris STEM. For magnetic and electron-transport measurements, the

cluster-deposited nanoparticles were deposited for an extended time as a dense film as discussed in our previous works [45, 46]. The above measurements were performed using a superconducting quantum interference device (SQUID) and physical property measurement system (PPMS), respectively. A schematic of a dense nanoparticle film is shown in Fig 4.3(d), and therefore they are exchange coupled and conducting. The thickness of the Co nanoparticle film is about 270 nm. The conduction channels for the Hall contacts were fabricated before depositing the Co nanoparticles, as described in Ref. 45. For electron-transport measurements, the film of thickness about 270 nm composed of Co nanoparticles having an average particle size of 13.7 nm, schematically shown in Fig. 4.3(d), was used. Therefore, a larger thickness of the film is essential to ensure the conduction through the contact points of nanoparticles (i.e., dense-packed film will have minimum voids).

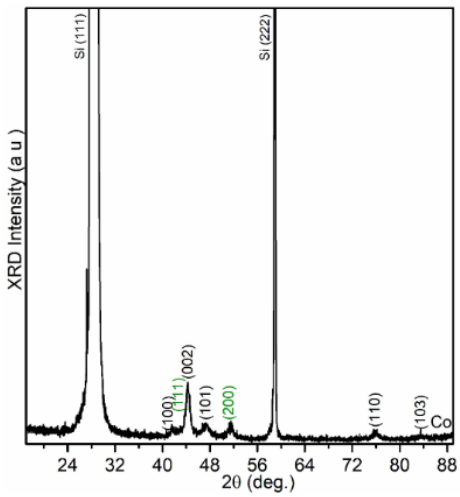

Figure. 4.4. X-ray diffraction pattern of the Co nanoparticle film.

To prevent oxidation upon exposure to air, the Co nanoparticle film was capped with a SiO_2 layer of about 10 nm thickness immediately after deposition, using a radio-frequency magnetron sputtering. The SiO_2 cap layer is thinner (about 10 nm) as compared to the Co nanoparticle film of about 270 nm thickness and is also diamagnetic.

Therefore, the film-SiO_2 interface is not expected to affect the magnetic and transport properties of the Co nanoparticle films. The particles have an average size of 13.7 nm with a narrow size distribution, see Fig 4.3 (b, c) and crystallize in the hcp structure, as shown in Fig. 4.4. A commercial AFM/MFM (Atto AFM/MFM Ixs; Attocube Systems) was used to map the topography and magnetic images at 200K. During the measurement, the MFM was performed in constant height mode (single pass) with PPP-MFMR tip from NANOSENSORS. The lift height is 250 nm and the scan speed is 5μm/s.

4.3 Computational Methods

To numerically model the magnetic and Berry-phase hysteresis, we have performed micromagnetic simulations using *ubermag* supported by OOMMF [47, 48]. We have numerically extracted skyrmion number Q from the spin structure. A densely packed film of 1000 Co nanoparticles has been considered. The Co particles have sizes of about 13.7 nm and the total size of the simulated system, shown in Fig. 4.5, is 240 nm × 240 nm × 60 nm. Figure 4.5(a) is a two-dimensional top view on the normalized magnetization $\boldsymbol{m}(r) = \boldsymbol{M}(r)/M_s$ in the virgin state, whereas Fig. 4.5(b) shows the random anisotropy of the nanoparticles, each color corresponding to a particle specific easy axis $\boldsymbol{n}$.

The cluster-deposition method yields isotropic nanoparticles with random grain orientation and therefore a random orientation of the easy magnetization axes $\boldsymbol{n}$ of the hcp Co particles, obeying $\langle n_x \rangle = \langle n_y \rangle = \langle n_z \rangle = 0$ and $\langle \boldsymbol{n}^2 \rangle = 1$. This randomness in simulations, clearly visible in Fig. 4.5, was implemented by using python np.random.uniform [48]. The particles touch each other as shown in Fig 4.3(d), so that the exchange stiffness A near the contact points is the same as in bulk Co. We have used a computational cell size of 1.8 nm, which is well below the exchange length l_{ex} [12],

coherence radius 5.099 l_{ex} of Co (10 nm) [12], and the domain-wall width (14 nm) of Co [12], and the current particle size. This cell size ensures a reasonable real-space resolution of $\boldsymbol{M}(\boldsymbol{r})$.

Aside from the numerical cell size, our continuum approach is valid on length scales much larger than the Co-Co interatomic distance of 0.25 nm. This makes it possible to consider the thin film as a fiber bundle $\boldsymbol{M}(\boldsymbol{r})$ with the base space $\boldsymbol{r}$, allowing us to define quantities such as the boundary curvature κ. A refined atomistic analysis, not considered here, would yield corrections due to the discrete nature of the atoms at the particle's surfaces and near contact points, see e.g. Sect. 4.5 in Ref. 12.

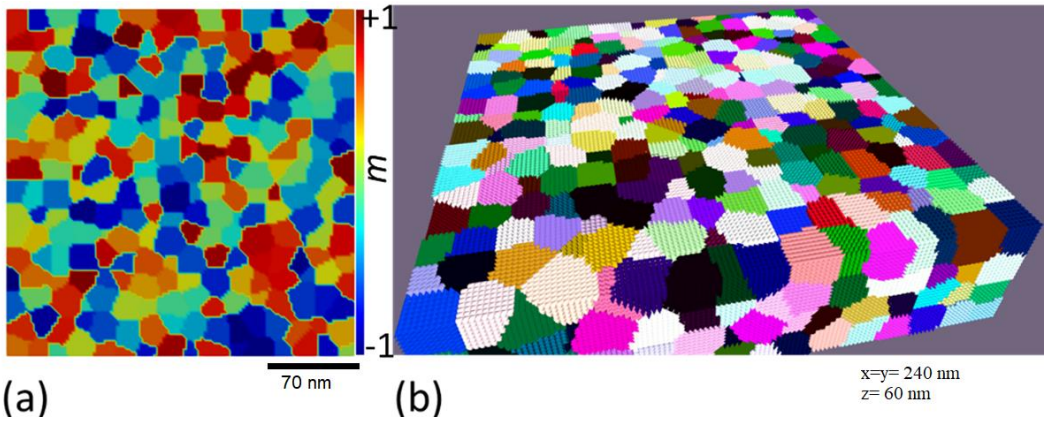

Figure 4.5. Co nanoparticle thin film used in the micromagnetic simulations: (a) two-dimensional image showing the magnetization direction in the virgin state (initial curve at $H = 0$) and (b) three-dimensional image showing the randomness of the particles' magnetocrystalline anisotropies.

Temperature-dependent micromagnetic effects are included in the lowest order, that is, by considering the intrinsic materials parameters M_s, K_1, and A as temperature-dependent. This approach accounts for the atomic spin disorder outlined in Fig. 4.1(a). Other finite-temperature corrections, caused for example by magnetic viscosity [12], have been ignored. In our simulations, we have taken values of M_s = 1300 kA/m, K_1 = 0.58 MJ/m^3, and A = 10.3 pJ/m [12].

4.4 Results and Discussion

4.4.1 Size and Magnetic Properties

Transmission electron microscope and the corresponding particle-size histogram show an average particle size of 13.7 nm with a standard deviation $\sigma/d \approx 0.15$ (Figs. 4.3b and 4.3c) for the Co nanoparticles. We have conducted magnetic, electron-transport, and Hall-effect measurements at temperatures from 10 K to 300 K for the dense Co nanoparticle films as schematically shown in Fig. 4.3(d). The magnetic hysteresis loops are shown in Fig. 4.6, and the measured coercivities are 0.18 T at 10 K and 0.04 T at 300 K.

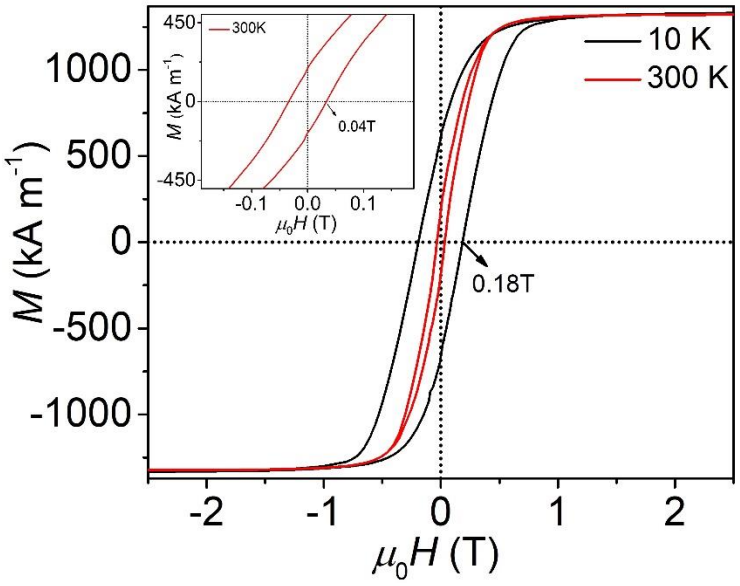

Figure 4.6. Magnetic hysteresis loops measured at 10 K and 300 K. The expanded room-temperature loop with clear coercivity is shown as inset.

4.4.2 Topological Hall Effect

The THE was extracted from the Hall-effect measurements performed using physical property measurement system (PPMS). Figure 4.7(a) shows the experimental curves measured at 300 K used to extract the topological Hall-effect (ρ_{THE}) from the

electron-transport and magnetic data (red curve). The extraction is based on the formula [33, 32]

$$\rho_{xy}(H) = R_0 H + R_s M + \rho_{THE}(H) \quad (3)$$

where ρ_{xy} is the Hall resistivity, R_0H describes the normal Hall effect, and R_sM corresponds to the anomalous Hall effect. R_0 and R_s are the ordinary and anomalous Hall coefficients, respectively. For the approximate character of this equation when applied to inhomogeneous systems, see Ref. [39].

When the magnetization approaches saturation, $\rho_{THE} = 0$ and R_sM becomes constant. Therefore, R_0 and R_s were determined by plotting ρ_{xy}/H vs M/H in the high field region. Using the values of R_0, R_s and M, the $R_0 H$ (blue curve), R_sM (black curve), and $\rho_{xy}-R_0H$ data (pink curve) were determined as a function of H as shown in Fig. 4.7(a). The difference between the R_sM and $\rho_{xy}-R_0H$ curves ideally yield the topological Hall effect contribution (green curve in Fig. 4.7(a)). The topological Hall effect contributions extracted from the experimental Hall data at 300 K and 10 K are shown in Fig. 4.7(b).

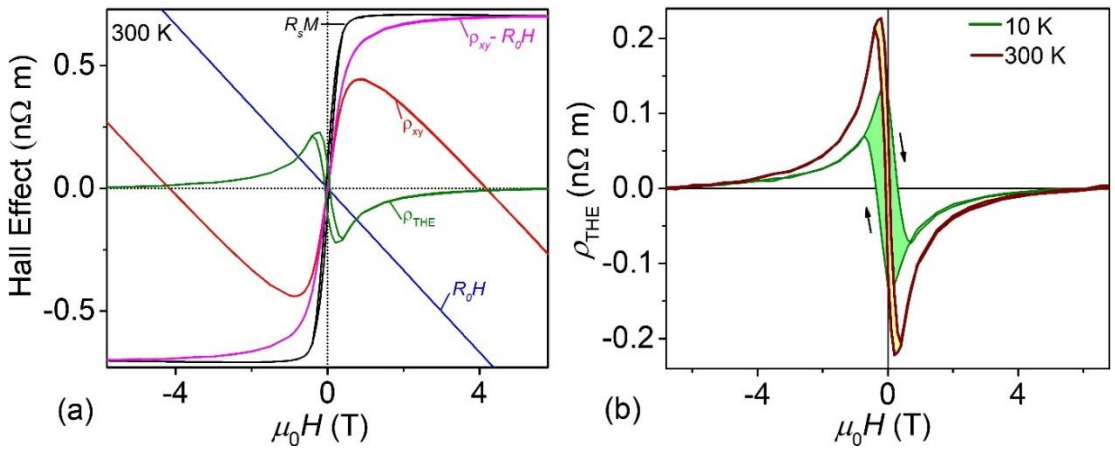

Figure 4.7. ***Hall effect and Topological Hall effect:*** (a) Field dependences of Hall resistivity (red), ordinary Hall effect (blue), AHE contribution (black), Hall resistivity excluding the ordinary Hall effect (pink), and topological Hall effect (green), and (b) topological Hall effect at 300 K and 10 K.

The longitudinal resistivity, Fig. 4.8, shows of the Co nanoparticle thin film slightly increases with temperature, from 0.26 μΩ m at 10 K to 0.32 μΩ m at 300 K (Fig. 4.8). This shows that the film is metallic and that the Co nanoparticles touch each other. This metallic contact is necessary to ensure exchange coupling between the nanoparticles and a noncollinear spin structure like that in Fig. 4.2(c). This ensures a topological Hall effect in case of a noncoplanar spin structure and the interparticle exchange assumed in the micromagnetic simulations. Note that the Bulk resistivity of Co is lower than the Co nanoparticle films because the conduction is only through the contact points of the nanoparticles [45].

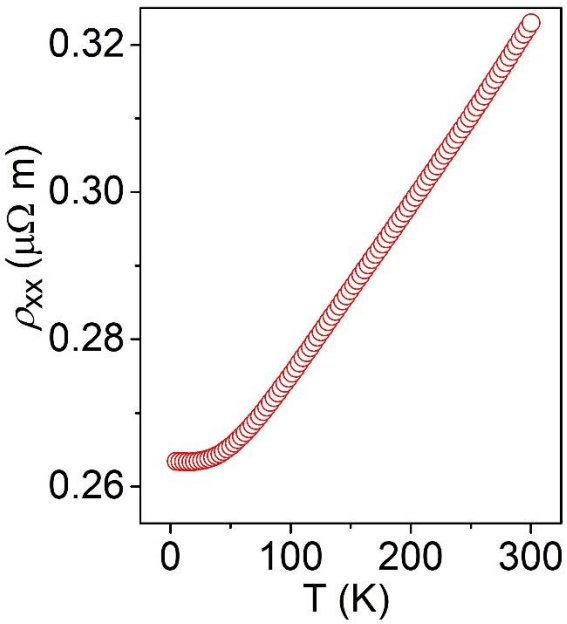

Figure 4.8. Temperature-dependent longitudinal resistivity ρ_{xx} of the Co nanoparticle film.

Figure 4.9 compares the experimental data on a Co nanoparticle thin film (a) with numerical predictions (b). The THE was extracted from Hall-effect measurements as explained in Fig. 4.7. We see that the Berry-phase hysteresis loops (colored) look qualitatively different from the magnetic hysteresis loops (black) and that they are much

broader than the magnetic ones. Figure 4.2(a-b) also shows that Berry-phase hysteresis loops contain more features than magnetic hysteresis loops. There are both mathematical and physical explanations for these differences. Mathematically, Eq. (1) contains derivatives, which amounts to a numerical amplification of details. Physically, Berry-phase hysteresis loops exhibit a more complicated dependence on the spin structure, because Φ is more complicated than $\boldsymbol{m}$.

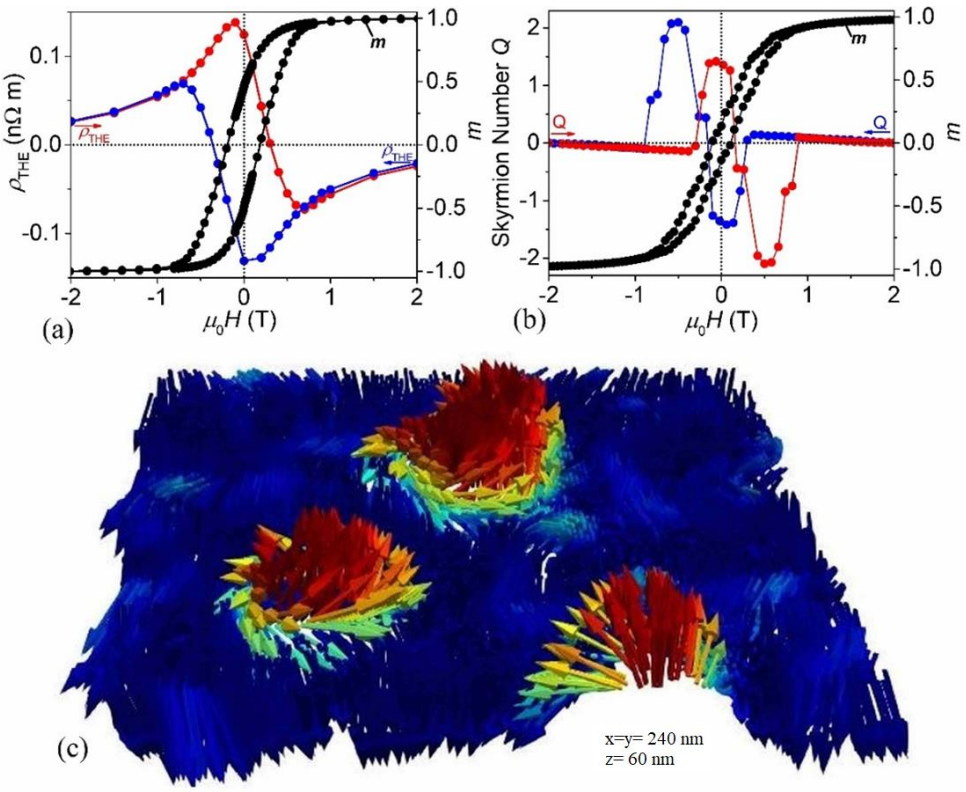

Figure 4.9. Magnetic hysteresis, Berry-phase hysteresis, and spin structure: (a) experiment, (b) simulation, and (c) simulated spin structure in a field of -0.7 T. In (b), Q is the number of skyrmions per unit area (240 nm × 240 nm × 60 nm), and m is the normalized magnetization, M_z/M_s. The origin of the topological Hall effect due to spin texture, namely the noncoplanar spin structure, is visible in (c).

Magnetization reversal in a thin film of nanoparticle magnets is strongly real-structure dependent, which affects the magnetic [12, 49, 50] and, especially, Berry-phase

hysteresis loops. There is an intricate balance between an interatomic exchange, magnetocrystalline anisotropy, and magnetostatic interactions, which result in spin structures such as that in Fig. 4.3(c) at some specific magnetic field. While the real structure leads to loop deformation, it does not affect the key feature of Figs. 4.1(d-i), namely red (or blue) regions in a blue (or red) background. This embedding is the origin of the THE.

Figures 4.10(a-b) illustrate the mathematical effect, by comparing the $M(H)$ curve (black) with its field derivative, the micromagnetic susceptibility $\chi = \mathrm{d}M/\mathrm{d}H$ (purple). While the experimental and theoretical $M(H)$ curves [Fig. 4.10(a) and 4.10(b), respectively] look similar, the derivative greatly enhances the differences. In the present system, the susceptibility peaks are due to Barkhausen jumps [49, 51], which are strongly real-structure dependent. A schematic example of a Barkhausen jump is a fictitious transition from Fig. 4.1(d) to 4.1(f). These transition changes enhance the red area and therefore the magnetization in a jump-like fashion. In fact, there are two types of Barkhausen jumps, which have not yet been distinguished in the literature. When the field changes the domain size and shape only, then Q remains constant, but the Barkhausen-induced creation or merger of domains changes Q like the transition from Fig. 4.1(f) to 4.1(g).

Physically, the topological Hall signal critically depends on details of the magnetization process. Figure 4.10(c) outlines the situation in the present system, by showing how the red and blue areas evolve in a magnetic field. In strongly negative fields, the magnetization is ↓ (blue) everywhere, but with increasing field, the magnetization starts to become noncoplanar noncollinear, and Eq. (1) yields a nonzero

skyrmion density. The red regions grow and finally coalesce. This coalescence does not change the magnetization very much but yields a drastic change in *Q*: red regions in a blue background become blue regions in a red background, which causes the sign of *Q* to switch. Since we investigate inhomogeneous nanoparticle thin film, the switching patterns exhibit considerable randomness, Fig. 4.10(c), but this does not affect the overall topological picture.

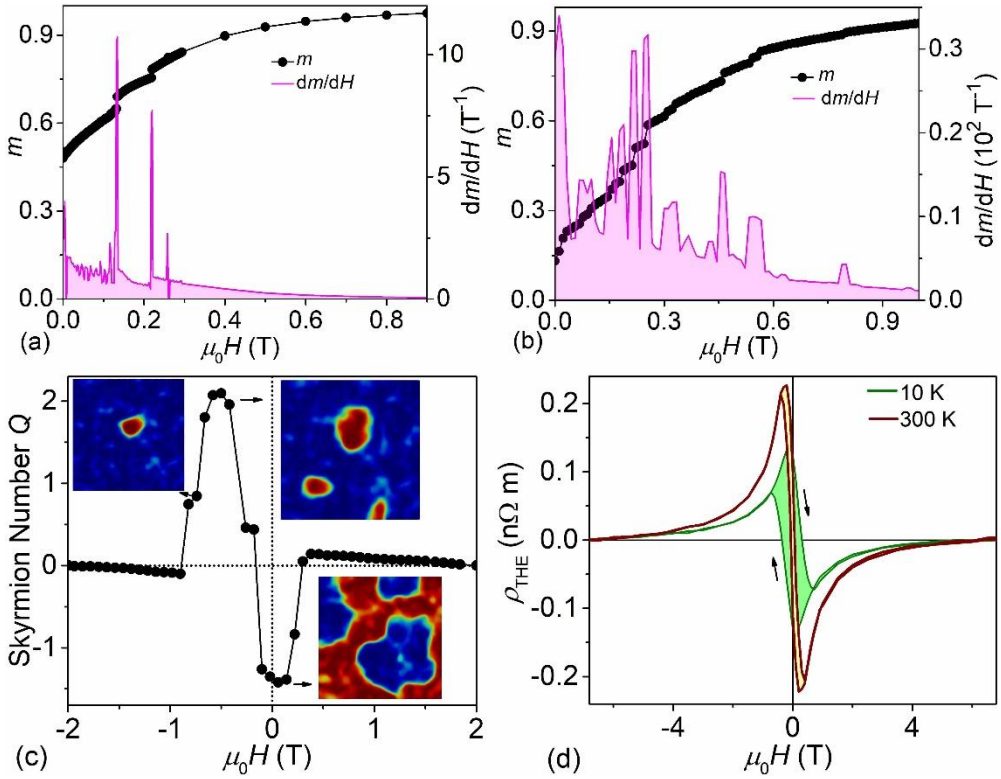

Figure 4.10. Real-structure and temperature effects: (a) experimental magnetization and susceptibility, (b) simulated magnetization and susceptibility, (c) the real-structure origin of the Berry-phase hysteresis, and (d) Berry-phase hysteresis at 10 and 300 K. The susceptibility peaks in (a-b) reflect Barkhausen jumps and are strongly real-structure dependent.

4.4.3 Magnetic Force Microscopy

We also measured the change of magnetic domains of the Co nanoparticle film by magnetic force microscope (MFM) (see Figure 4.11) and the corresponding Atomic

Force Microscopy (AFM) topography images at room temperature. As discussed above, the exchange-coupled nanoparticles involve in cooperative magnetization reversal, and the reversed magnetic domains expand with increasing the magnetic field. This is seen from the phase images of MFM, which show that the individual magnetic domains with closed domain walls appear at around 0.04 T, and their size increases as the magnetic field increases. Our electron-transport data show that the THE has a maximum value in the region -0.02 T to 0.02 T. The MFM in images also shows a comparatively large number of smaller magnetic bubbles around this field region. Note that the bigger magnetic domains may still contain several small domains in the field region -0.02 T to 0.02 T, which could not be visualized due to the low resolution of MFM.

In the MFM images, the positive (negative) phase shift corresponds to the repulsive (attractive) force between the tip and magnetic stray field. When the sample is fully magnetized at a saturated field, the parallel alignment of the magnetic moment for the sample and tip should contribute to the negative phase. However, under lift mode, the severe change of surface roughness may perturb the phase signal, and there exist areas with a positive phase (the yellow region in the uneven surface) that persist even under 5 T. However, in a relatively flat area, the closed magnetic domains with negative phase signals undergo field-driven expanding and subsequent coalescence. Our AFM and MFM images are shown in Figs. 4.11, and 4.12 show that the region in which the field gradient disappear is almost even, while the region where the field gradient does not change has an uneven surface.

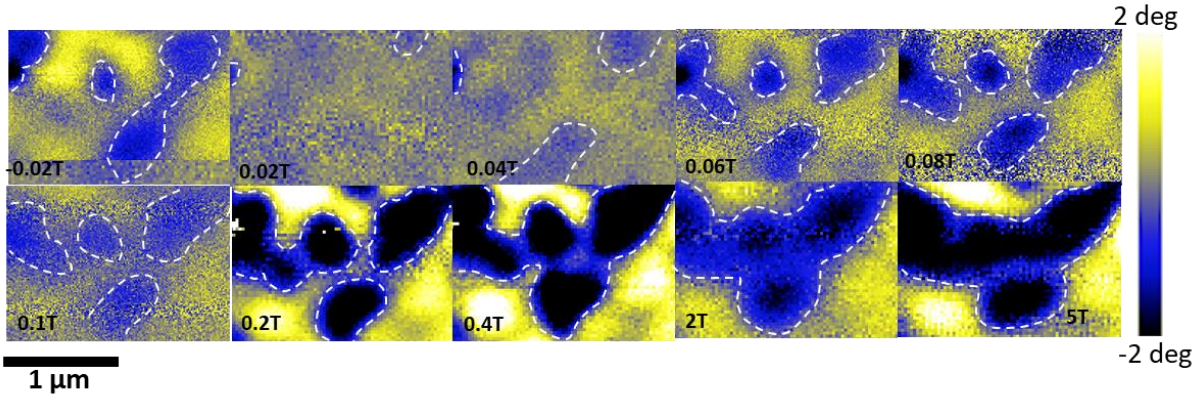

Figure 4.11. MFM image and magnetization reversal: MFM image of magnetization reversal in a region with an even surface (blue region). The magnetization reversal starts randomly making domains at a field of 0.06 T and these domains expand as the field is increased and finally coalescence of the domain occurs at a high field. Note that not only do we have topological contributions due to magnetic domains, but we also have a topological contribution to THE due to chiral spin inhomogeneity, and imaging of those spins is difficult [46, 52].

4.4.4 Cooperative and Non-cooperative Magnetization Reversal

The magnetization and magnetization reversal in the exchange-coupled Co nanoparticle film can be explained using the magnetization reversal process, as schematically shown in Fig. 4.12. A key question is whether the reversal is noncooperative as in Figure 4.12(a), as compared to a cooperative reversal in Figure 4.12(b). It is known that noncooperative reversal dominates in systems with broad switching-field distributions (small values of dM/dH), whereas narrow switching field distributions (large values of dM/dH) favor cooperative reversal [12]. The underlying physical mechanism is that the interatomic exchange proportional to A/R^2, where A is the exchange stiffness, competes against the anisotropy of strength K_1. For very small particles, as well as in very soft magnets (small K_1), the exchange dominates and the

reversal is cooperative. Elemental Co is a prototypical semihard magnet and particle size is fairly small, so we are in an intermediate regime closer to cooperative reversal, Fig. 4.12(b) than to noncooperative reversal, Fig. 4.12(a). The sizes of the cooperative blocks are random, and some of the blocks are fairly large. The switching of such big blocks has the character of Barkhausen jumps.

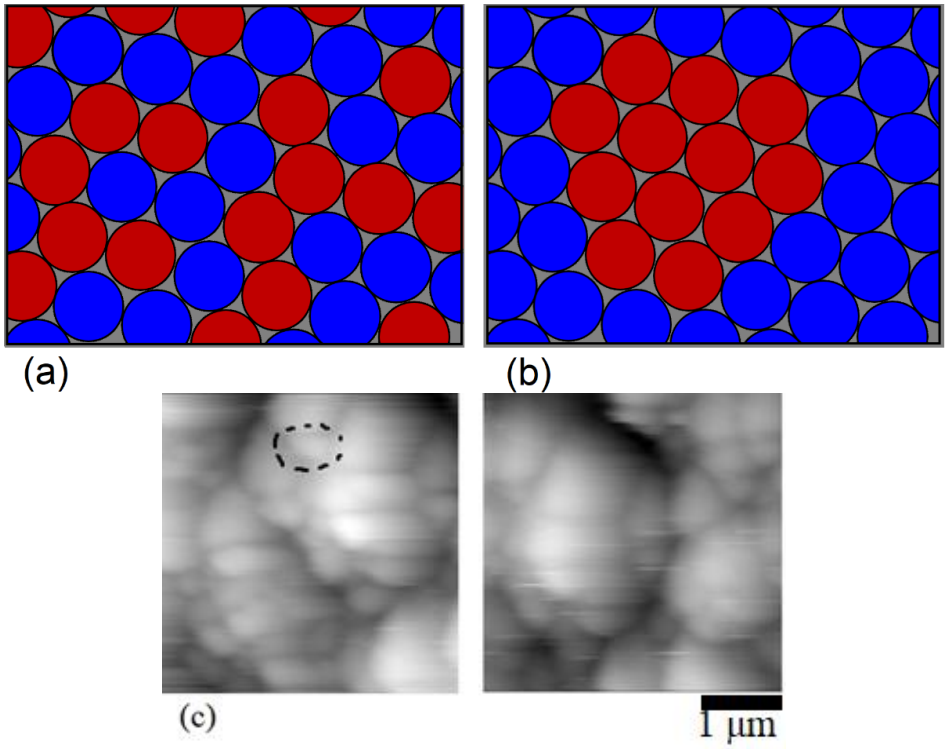

Figure 4.12. Schematic description of the Co nanoparticles: (a) noncooperative reversal, (b) cooperative reversal. The cooperative reversal shown in (b) creates a finite magnetic flux quantum of $\pm h/e$. The cooperative reversal represents the cluster within one region. As the magnetic field increases, it expands and affects the neighboring cluster. (c) Big clusters/regions are made of small grains with visible boundaries, these small clusters are made of small nanoparticles. In cooperative reversal these grains 1st reverse just like in (a) and then this reversal extends to the whole region.

The cooperative and non-cooperative reversal can be explained by considering the magnetization reversal involving the energy function. The energy functional considered

during micromagnetic simulations is [12]:

$$E = \int \left\{ A\left[\nabla\left(\frac{\boldsymbol{M}}{M_s}\right)\right]^2 - K_1 \frac{(\boldsymbol{n}.\boldsymbol{M})^2}{M_s^2} - \mu_o \boldsymbol{M}.\boldsymbol{H} - \frac{\mu_o}{2} \boldsymbol{M}.\boldsymbol{H}_d(\boldsymbol{M}) \right\} dV \tag{4}$$

Here $M_s(\boldsymbol{r})$ is the saturation magnetization, $K_1(\boldsymbol{r})$ denotes the first uniaxial anisotropy constant, $A(\boldsymbol{r})$ is the exchange stiffness, and $\boldsymbol{n}(\boldsymbol{r})$ is the unit vector of the local anisotropy direction. $\boldsymbol{H}$ is the external magnetic field, and $\boldsymbol{H}_d$ is the magnetostatic self-interaction field:

$$\boldsymbol{H}_d(\boldsymbol{r}) = \frac{1}{4\pi} \int \frac{3(\boldsymbol{r}-\boldsymbol{r}')(\boldsymbol{r}-\boldsymbol{r}')\cdot\boldsymbol{M}(\boldsymbol{r}') - |\boldsymbol{r}-\boldsymbol{r}'|^2 \boldsymbol{M}(\boldsymbol{r}')}{|\boldsymbol{r}-\boldsymbol{r}'|^5} dV' \tag{5}$$

For complicated magnets we can use $(3\boldsymbol{rr} - r^2)/r^5 = -\nabla(\mathbf{r}/r^3)$ and $\nabla.(a\mathbf{b}) = a\,\nabla.\,\mathbf{b} + \nabla a.\,\mathbf{b}$. It enable to write eq. 5 in terms of magnetic charge density $\rho_M = -\nabla.\,\mathbf{M}$. The self-interaction then assume the form [53]:

$$\boldsymbol{E}_{ms} = \frac{\mu_o}{4\pi} \int \frac{\rho_M(\mathbf{r})\,\rho_M(\mathbf{r}')}{|\boldsymbol{r}-\boldsymbol{r}'|} dV' \tag{6}$$

Since most magnets are structurally inhomogeneous, so that $\nabla.\,\mathbf{M} \neq 0$ inside the magnet. This leads to relatively high energy. Which is reduced by domain wall formation. Additionally magnetic charge at the surface also leads to relatively high magnetostatic energy. Domain formation and flux closure are very good source to reduce this energy.

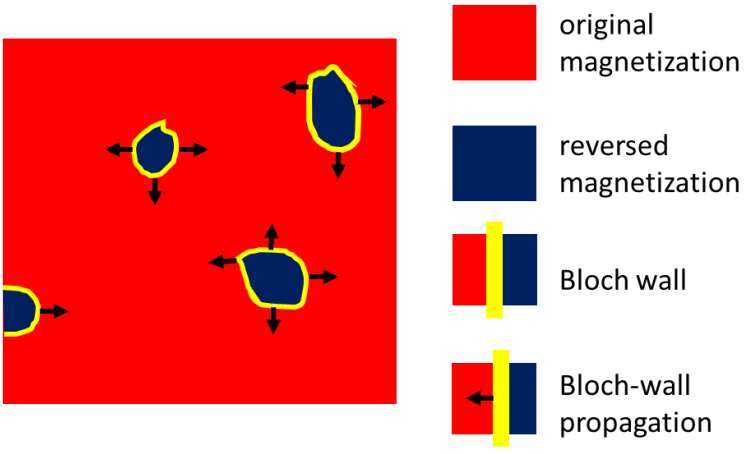

Figure 4.13. Microstructural interpretation of domains, each creating finite magnetic flux quantum of $\pm h/e$.

Figure 4.13 show the formation of the magnetic domain due to the cooperative reversal of the exchanged-coupled nanomagnets. These domains are created during the reversal in order to achieve the lowest energy state. In nanostructure, the multi-domains appear due to the charge avoidance principle [54]. Our Co nanoparticle thin film is inhomogeneous, giving finite magnetic charge density $\rho_M = -\nabla . \mathbf{M}$. The minimization requires that the magnetization within the film must have little divergence in order to avoid finite $\rho_M = -\nabla . \mathbf{M}$. Therefore, the magnetization reversal is initiated in a small volume around inhomogeneity. During the reversal, bubble-like domain appears with core magnetization surrounded by the Bloch wall. The domain expands under the action of the reverse field, and the cylindrical Bloch domain wall subsequently forms spin texture like magnetic bubbles [55]. These type of domains are type 1 bubbles in which the core is uniformly magnetized surrounded by the Bloch type domain wall that circulate either in a clockwise or anticlockwise direction as described in Fig. 4.2. These bubbles are mainly stabilized by dipole-dipole interactions rather than a strong Dzyaloshinskii-Moriya interaction and have the same topology of Bloch skyrmion, creating magnetic flux quantum of $\pm h/e$ and giving rise to finite THE [56].

4.4.5 Effect OF Temperature on Magnetization Reversal

Another intriguing aspect is an increase in the topological Hall effect with increasing temperature. As mentioned above, the Co nanoparticles are exchanged coupled, which exhibit cooperative magnetization reversal and subsequently gives rise to the chiral domains with chiral domain walls i.e yellow boundary enclosing the region with uniform magnetization (Figure 4.2). As temperature increases, the exchange stiffness constant decreases in Co [54,57,58].

$$A_{ex} = \frac{k_B T_c S}{\sqrt{2}\, a\,(S+1)} \quad (7)$$

The spin quantum number S is related to saturation magnetization by $M_s = g\mu_B S/V$ [57]. g = 2 and V is the volume. Using saturation magnetization at 10 K and 300 K in Eq. (3) gives A_{ex} = 10.3 pJ/m at 10 K and 10.1 pJ/m at 300 K. This shows that the exchange constant decreases with temperature as observed in Ref. [58].

Second, at elevated temperatures, the reversal is not only accompanied by nucleation but also by the thermal fluctuation of spins i.e., the probability of flipping of spins increases as temperature increases because of a small increase in thermal energy (Ref. 54, Ch. 6). These two factors cause the magnetization reversal easier and lead to an increase in the number of individual domains with the noncoplanar spin structures. Therefore, an increase in temperature is expected to increase the intensity of the topological Hall effect as observed in the case of exchange-coupled Co nanoparticle film. This feature, linked to the high Curie temperature of Co, is an advantage because the non-coplanar spin texture with finite skyrmion number caused by B20 Dzyaloshinskii-Moriya interactions requires considerable effort at high temperatures [38]. It is worth noting that the chiral domains reported in this study are only quantified in terms of skyrmion numbers and are not traditional skyrmions caused by Dzyaloshinskii–Moriya interaction (DMI) in B20-type materials and interfacial DMI in multi-layered thin films.

4.4.6 Berry Phase Hysteresis

Magnetic hysteresis loops are typically plotted by showing the magnetization M as a function of the magnetic field H. Figures 4.9 and 4.10 show that this is also possible for Berry-phase hysteresis. However, such plots convolute magnetic and topological properties, because the field generally changes both $\boldsymbol{M}$ and its gradient $\nabla\boldsymbol{M}$. To remove

this field effect, we introduce a new plot showing Q as a function of $m = M/M_s$ (Fig. 4.14). In this parametric Q-M plot, each field corresponds to one point in Q-M space, but this field is not shown explicitly unless each point of the curve is explicitly labeled by its field value.

The Q-M plot provides not only an entirely new view of Berry-phase hysteresis but also simplifies the analysis. In particular, $m = -1$ and $m = +1$ correspond to homogeneous magnetization states, so that $Q\ (m = \pm 1) = 0$. Berry-phase hysteresis occurs for intermediate values of m, and Fig. 4.14(a) shows that this hysteresis is accompanied by a topological remanence Q_o. Approximating the $Q(m)$ by a cubic polynomial [59] yields

$$Q = (Q_o + Q_1\, m)\,(1 - m^2) \tag{8}$$

A cubic polynomial contains four parameters, but only two of them, namely Q_o and the magnitude-parameter Q_1, are adjustable. The remaining two parameters are implicitly fixed by the boundary conditions at $m = \pm 1$. While Eq. (8) is a rather crude approximation, it works surprisingly well for the present system, as evidenced by the comparison with experiment in Fig. 4.14(b).

Figures 14(c-g) show how the Berry-phase hysteresis evolves in a simple exactly solvable model. Circular red domains are arranged on a triangular lattice (c) and grow in the external field (c). At the phase-transition point, the domains touch and start to overlap, so that the background changes from blue to red and the THE changes sign. Figure 14(g) shows the Q-m plot for the model of (c-d). The transition is triggered by an external magnetic field, but near the transition point, there is only a trivially small magnetization change. We also note that the transition (c→d) occurs at a point where most of the area is red (↑) already, at a magnetization of $\pi/\sqrt{3} - 1 \approx 0.814\ M_s$. This is the

reason for the striking width of the green topological hysteresis loop in Fig. 4.14(g). The light blue and light red areas in Fig. 14(g) are model-specific and related to the duality of the assumed skyrmion lattice. Figures 4.14(c) and 4.14(d) correspond to triangular and honeycomb lattices, respectively, which are dual but have different numbers of sites per honeycomb unit cell (3 and 6). By comparison, square lattices are self-dual, which causes the bright areas to disappear. In the light of this model analysis, the difference between the red/blue curves in Figs. 4.9(a) and (b) is not surprising, but a comprehensive explanation of the duality effect is a challenge to future mathematical and physical research. The domain structures with domain-wall chirality of Figs. 4.14(e-f) are topologically but not micromagnetically equivalent to (c-d) and yield a real-structure dependent smoothing of the rectangular loop parts in (g).

It is interesting to note that domain structures like those in Figs. 4.1 and 4.5 have been around for decades [49, 60], as it has the recognition of features such as domain-wall chirality [60, 61]. However, at that time, neither the Berry phase nor the topological Hall effect was widely aware [5, 32, 37]. Furthermore, the initial research focused on bubble domains of fairly large sizes L, typically micron-sized. Each reverse domain contributes one flux quantum to the THE, so that the net effect scales a $1/L^2$. Even today, such small effects are nontrivial to detect without the help of Dzyaloshinski-Moriya (DM) interactions [17], and this is the main reason for our consideration of Co nanoparticle thin films, where L a few 10 nm.

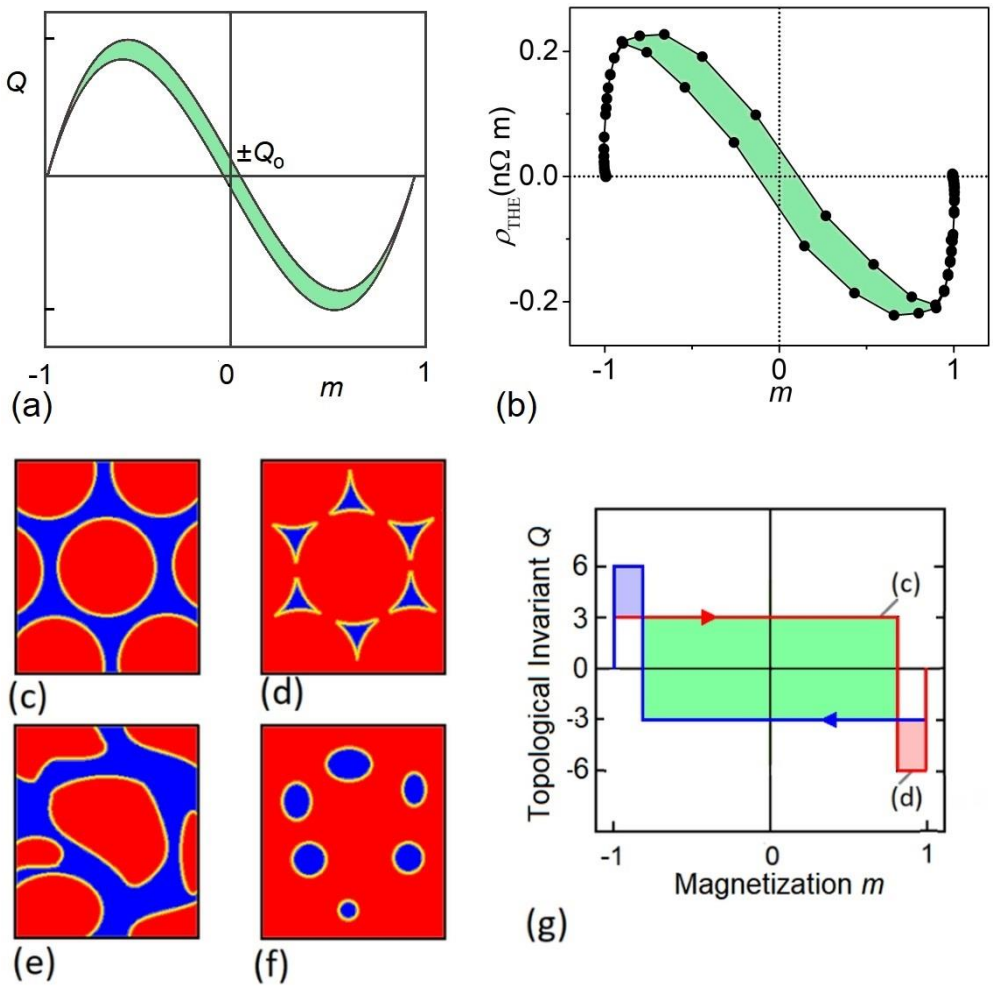

Figure 4.14. ***Analytical modeling of Berry-phase hysteresis*:** (a) most general cubic plot of skyrmion number Q as a function of magnetization, (b) experimental Q-M plot, (c-d) topological phase transition (TPT) in a simple circular-domain model, (e-f) topologically equivalent version of the same model, and (g) Berry-phase hysteresis loop for the model of (c-d). The transitions from (c) to (d) and from (e) to (f) are triggered by a magnetic field increase and accompanied by an incremental magnetization increase only. In (g), the transition occurs at a fairly high value of $M_z = \pm 0.814\ M_s$. At $M_z = \pm M_s$, Q jumps to zero, because the residual domains are annihilated at saturation. The light-blue and light-red areas in (g) are a duality effect caused by the triangular skyrmion lattice assumed in (a-b). As in other parts of the paper, m is the normalized magnetization ($m = M_z/M_s$).

Future applications of Berry-phase hysteresis in spin electronics and beyond [62, 63, 64] are difficult to judge. The low skyrmion mobility in the present nanoparticle

system will probably prevent applications such as racetrack memories [62], but three arguments speak in favor of the potential technological usefulness of Berry-phase hysteresis. First, the small feature size addresses miniaturization requirements in spin electronics. Second, Co has a very high Curie temperature, which facilitates the measurement and practical exploitation of its THE. In fact, Fig. 4.10(d) shows that the effect actually *increases* with temperature. By contrast, noncentrosymmetric materials tend to have rather low magnetic ordering temperatures, requiring considerable effort to drive the systems beyond room temperature [23, 38]. Third, the effect has a very high field sensitivity, as one can see from Fig. 10(d), and by comparing the maximum slopes of the red, blue, and black curves in Fig. 4.9(b).

4.5 Conclusion

The starting point and first main finding in this paper is the recognition that the thin-film magnetization reversal has the character of a topological phase transition. The transition is accompanied by Berry-phase hysteresis, a phenomenon very different from ordinary magnetic hysteresis and exhibiting features such as topological remanence and micromagnetic duality. The new concept has led to the development of a topology-specific plot showing the skyrmion number as a function of magnetization rather than the field. In our Co nanoparticle system, the Berry-phase hysteresis is realized on a nanoscale, increases with temperature, and exhibits a high field sensitivity. Several interdisciplinary challenges emerge from the present work. For example, it is intriguing to see which other systems investigated in the past, presence, and future exhibit Berry phase hysteresis and how it is realized.

References

[1] J. M. Kosterlitz, Rev. Mod. Phys. **89**, 040501-1-7 (2017).

[2] Ch. Lin, M. Ochi, R. Noguchi, K. Kuroda, M. Sakoda, A. Nomura, M. Tsubota, P. Zhang, C. Bareille, K. Kurokawa, Y. Arai, K. Kawaguchi, H. Tanaka, K. Yaji, A. Harasawa, M. Hashimoto, D. Lu , Sh. Shin, R. Arita, S. Tanda, and T. Kondo, Nat. Mater. **20**, 1093-1099 (2021).

[3] M. Levin and X.-G. Wen, Phys. Rev. Lett. **96**, 110405-1-4 (2006).

[4] X.-G. Wen, *Quantum-Field Theory of Many-Body Systems*, University Press, Oxford 2004.

[5] D. Xiao, M.-Ch. Chang, and Q. Niu, Rev. Mod. Phys. **82**, 1959–2007 (2010).

[6] B. A. Bernevig, T. L. Hughes, and S.-C. Zhang, Science **314**, 1757-1761 (2006).

[7] I. M. Lifshitz, Sov. Phys. JETP **11,** 1130-1135 (1960).

[8] J. M. Kosterlitz and D. J. Thouless, J. Phys. C **6**, 1181-1203 (1973).

[9] H. Huang and F. Liu, AAAS Research **2020**, 7832610-1-7 (2020).

[10] E. Warburg, Ann. Phys. (Leipzig) **249**, 141-164 (1881).

[11] M. Dörries, Hist. Stud. Nat. Sci. **22**, 25–55 (1991).

[12] R. Skomski, J. Phys.: Condens. Matter. **15**, R841-896 (2003).

[13] L. D. Barron, "An introduction to Chirality at the Nanoscale", in: *Chirality at the Nanoscale*, Ed. D. B. Amabilino, Wiley, New York 2009, p. 1-27.

[14] W. Jiang, P. Upadhyaya, W. Zhang, G. Yu, M. B. Jungfleisch, F. Y. Fradin, J. E. Pearson, Y. Tserkovnyak, K. L. Wang, O. Heinonen, S. G. E. te Velthuis, and A. Hoffmann, Science **349**, p. 283-286 (2015).

[15] M. Lonsky and A. Hoffmann, Phys. Rev. B **102**, 104403-1-11 (2020).

[16] S.-G. Je, H.-S. Han, S. K. Kim, S. A. Montoya, W. Chao, I.-S. Hong, E. E. Fullerton, K.-S. Lee, K.-J. Lee, M.-Y. Im, and J.-I. Hong, ACS Nano **14**, 3251-3258 (2020).

[17] W. Zhang, B. Balamurugan, A. Ullah, R. Pahari, X. Li, L. Yue, S. R. Valloppilly, A. Sokolov, R. Skomski, and D. J. Sellmyer, Appl. Phys. Lett. **115**, 172404-1-4 (2019).

[18] W. Wang, Y.-F. Zhao, F. Wang, M. W. Daniels, C.-Z. Chang, J. Zang, D. Xiao, and W. Wu, Nano Lett. **21**, 1108-1114 (2021).

[19] P. Li, J. Ding, S. S.-L. Zhang, J. Kally, T. Pillsbury, O. G. Heinonen, G. Rimal, Ch. Bi, A. DeMann, S. B. Field, W. Wang, J. Tang, J. S. Jiang, A. Hoffmann, N. Samarth, and M. Wu, Nano Lett. **21**, 84-90 (2021).

[20] E. Y. Vedmedenko, R. K. Kawakami, D. D. Sheka, P. Gambardella, A. Kirilyuk, A. Hirohata, C. Binek, O. Chubykalo-Fesenko, S. Sanvito, J. Grollier, K. Everschor-Sitte, T Kampfrath, C.-Y. You, and A Berger, J. Phys. D: Appl. Phys. **53**, 453001-1-44 (2020).

[21] Y. Taguchi, Y. Oohara, H. Yoshizawa, N. Nagaosa, and Y. Tokura, Science **291,** 2573-2576 (2001).

[22] M. Z. Hasan and C. L. Kane, Rev. Mod. Phys. **82**, 3045-3067 (2010).

[23] Y. Tokunaga, X. Z. Yu, J. S.White, H. M. Rønnow, D. Morikawa, Y. Taguchi, and Y. Tokura, Nat. Commun. **6**. 7638-1-13 (2015).

[24] K. G. Rana, O. Meshcheriakova, J. Kübler, B. Ernst, J. Karel, R Hillebrand, E. Pippel, P. Werner, A. K. Nayak, C. Felser, and S. S. P. Parkin, New J. Phys. **18**, 085007 (2016).

[25] A. Soumyanarayanan, N. Reyren, A. Fert, and Ch. Panagopoulos, Nature **539**, 509-517 (2016).

[26] D. S. Sanchez, I. Belopolski, T. A. Cochran, X. Xu, J.-X. Yin, G. Chang, W. Xie, K. Manna, V. Süß, Ch.-Y. Huang, N. Alidoust, D. Multer, S. S. Zhang, N. Shumiya, X. Wang,

G.-Q. Wang, T.-R. Chang, C. Felser, S.-Y. Xu, Sh. Jia, H. Lin, and M. Z. Hasan, Nature **567**, 500-499 (2019).

[27] M. Raju, A. Yagil, A. Soumyanarayanan, A. K. C. Tan, A. Almoalem, Fusheng Ma, O. M. Auslaender, and C. Panagopoulos, Nat. Commun. **10**, 696-1-7 (2019).

[28] A. K. Sharma, J. Jena, K. G. Rana, A. Markou, H. L. Meyerheim, K. Mohseni, A. K. Srivastava, I. Kostanoskiy, C. Felser, and S. S. P. Parkin, Adv. Mater., 33, 2101323 (2021).

[29] M. Tomé and H. D. Rosales, Phys. Rev. B **103**, L020403-1-5 (2021).

[30] J. P. Pekola, K. Torizuka, A. J. Manninen, J. M. Kyynäräinen, and G. E. Volovik, Phys. Rev. Lett. **65**, 3293-3296 (1990).

[31] N. Nagaosa and Y. Tokura, Nat. Nanotechnol. **8**, 899-911 (2013).

[32] A. Neubauer, C. Pfleiderer, B. Binz, A. Rosch, R. Ritz, P. G. Niklowitz, and P. Böni, Phys. Rev. Lett. **102**, 186602-1-4 (2009).

[33] S. Seki and M. Mochizuki, "Skyrmions in magnetic materials", Springer International, Cham (2016).

[34] Y. Fujishiro, N. Kanazawa, T. Nakajima, X.Z. Yu, K. Ohishi, Y. Kawamura, K. Kakurai, T. Arima, H. Mitamura, A. Miyake, K. Akiba, M. Tokunaga, A. Matsuo, K. Kindo, T. Koretsune, R. Arita, and Y. Tokura, Nat. Commun. **10**, 1059 1-8 (2019).

[35] L. Pierobon, Ch. Moutafis, Y. Li, and J. F. Löffler, Sci. Rep. **8**, 16675-1-9 (2018).

[36] S. Das, Z. Hong, V. A. Stoica, M. A. P. Gonçalves, Y. T. Shao, E. Parsonnet, E. J. Marksz, S. Saremi, M. R. McCarter, A. Reynoso, C. J. Long, A. M. Hagerstrom, D. Meyers, V. Ravi, B. Prasad, H. Zhou, Z. Zhang, H. Wen, F. Gómez-Ortiz, P. García-Fernández, J. Bokor, J. Íñiguez, J. W. Freeland, N. D. Orloff, J. Junquera, L. Q. Chen, S. Salahuddin, D. A. Muller, L. W. Martin, and R. Ramesh, Nat. Mater. **20**, 194-201 (2021).

[37] M. V. Berry, Proc. R. Soc. Lond. A **392**, 45-57 (1984).

[38] B. Balasubramanian, P. Manchanda, R. Pahari, Z. Chen, W. Zhang, S. R. Valloppilly, X. Li, A. Sarella, L. Yue, A. Ullah, P. Dev, D. A. Muller, R. Skomski, G. C. Hadjipanayis, and D.J. Sellmyer, Phys. Rev. Lett. **124**, 057201-1-6 (2020).

[39] R. Skomski, B. Balasubramanian, A. Ullah, C. Binek, and D. J. Sellmyer, AIP Adv., **12**, 035341 (2022).

[40] W. Fenchel, "Über Krümmung and Windung geschlossner Raumkurven", Math. Ann. **101**, 238-252 (1929).

[41] Y. He, T. Helm , I. Soldatov , S. Schneider , D. Pohl, A. K. Srivastava, A. K. Sharma, J. Kroder, W. Schnelle, R. Schaefer, B. Rellinghaus, G. H. Fecher, S. S. P. Parkin, and C. Felser, Phys. Rev. B **105**, 064426-1-8 (2022)

[42] H. Seifert, "Topologie dreidimensionaler gefaserter Räume", Acta Math. **60**, 147–238 (1933).

[43] J. W. Zwanziger, M. Koenig, and A. Pines, "Berry's Phase", Annu. Rev. Phys. Chern. **41**, 601-646 (1990).

[44] B. Ding, J. Zhang, H. Li, S. Zhang, E. Liu, G. Wu, X. Zhang, and W. Wang, Appl. Phys. Lett. **116**, 132402-1-5 (2020).

[45] B. Balasubramanian, T. A. George, P. Manchanda, R. Pahari, A. Ullah, R. Skomski, and D. J. Sellmyer, Phys. Rev. Mater. **5**, 024402-1-9 (2021).

[46] R. Pahari, B. Balasubramanian, A. Ullah, P. Manchanda, H. Komuro, R. Streubel, C. Klewe, Shah R. Valloppilly, P. Shafer, P. Dev, R. Skomski, and David J. Sellmyer, Phys. Rev. Mater. **5**, 124418 (2021).

[47] M. Beg, R. A. Pepper, and H. Fangohr. AIP Advances **7**, 56025 (2017), M. Beg, R. A. Pepper, T. Kluyver, J. Mulkers, J. Leliaert, and H. Fangohr. ubermag: Meta package for Ubermag project. DOI: 10.5281/zenodo.3539496 (2021).

[48] Our code is publically available: https://github.com/ubermag/help/issues/110#issuecomment-970591821

[49] A. Hubert and R. Schäfer, *Magnetic Domains*, Springer-Verlag, Berlin (1998).

[50] L. Exl, D. Suess, and T. Schrefl, "Micromagnetism", in: *Handbook of Magnetism and Magnetic Materials*, Eds. J. M. D. Coey and S. S. Parkin, Springer, Cham, p. 347-390.

[51] H. Barkhausen, "Zwei mit Hilfe der Neuen Verstärker entdeckte Erscheinungen", Phys. Z. **20**, 401-403 (1919).

[52] Haohan Wang, Balamurugan Balasubramanian, Rabindra Pahari, Ralph Skomski, Yaohua Liu, Ashfia Huq, D. J. Sellmyer, and Xiaoshan Xu Phys. Rev. Mater. **3**, 064403 (2019).

[53] A. A. Thiele, Bell Syst. Tech. J. **48**, 3287 (1969).

[54] J. M. D. Coey, Magnetism and Magnetic Materials (Cambridge University Press, New York, 2010), R. Skomski and J. M. D. Coey, Permanent Magnetism (Institute of Physics, Bristol, 1999).

[55] J. Jiang, D. Xiao, F. Wang, J.-H. Shin, D. Andreoli, J. Zhang, R. Xiao, Y.-F. Zhao, M. Kayyalha, L. Zhang, K. Wang, J. Zang, C. Liu, N. Samarth, M. H. W. Chan, and C.-Z. Chang, Nat. Mater. 19, 732 (2020).

[56] W. Koshibae, N. Nagaosa, New J. Phys. **18** 045007 (2016).

[57] H. Kronmüller and M. Fähnle, Micromagnetism and the Microstructure of Ferromagnetic Solids (University Press, Cambridge 2003).

[58] R. Moreno, R. F. L. Evans, S. Khmelevskyi, M. C. Munoz, R. W. Chantrell, and O. Chubykalo-Fesenko Phys. Rev. B **94**, 104433 (2016).

[59] W. Zhang, B, Balasubramanian, Y. Sun, A. Ullah, R. Skomski, R. Pahari, S. R. Valloppilly, X.-Zh. Li, C.-Zh. Wang, K.-M. Ho, and D. J. Sellmyer, J. Magn. Magn. Mater. **537**, 168104 (2021).

[60] P. J. Grundy and S. R. Herd phys. stat. sol. (a) **20**, 295-307 (1973).

[61] G. Kimbell, P. M. Sass, B. Woltjes, E. K. Ko, T. W. Noh, W. Wu, and J. W. A. Robinson, Phys. Rev. Mater. **4**, 054414 (2020).

[62] S. S. P. Parkin, M. Hayashi, and L. Thomas, Science **320**, 190-194 (2008).

[63] A. Fert, N. Reyren, and V. Cros, Nat. Rev. Mater. **2**, 17031-1-15 (2017).

[64] C. Back, V. Cros, H. Ebert, K. Everschor-Sitte, A. Fert, M. Garst, T. Ma, S. Mankovsky, T. L. Monchesky, M. Mostovoy, N. Nagaosa, and S. S. P. Parkin, J. Phys. D **53**, 363001-1-37 (2020).

Chapter 5 Topological Hall Effect due to Chiral Spin Texture

5.1 Introduction

In the previous chapter, the real space Berry phase is described in nanoparticles, which were either non-interacting nanodots or exchange-coupled nanomagnets. In this chapter, we will discuss the topological Hall effect due to non-coplanar and non-collinear spin textures. The finite value of the skyrmion number in the magnetic states describes the degree of noncoplanarity. With the increase, the nonuniformity in $\boldsymbol{M}(\boldsymbol{r}, H)$ increases skyrmion density. These spin textures can give a contribution to the anomalous Hall Effect known as the Berry phase topological Hall effect (THE) due to the presence of small inhomogeneous magnetization $\boldsymbol{M}(\boldsymbol{r}, H)$ [1, 2].

Figure 5.1 summarizes the origin of the Berry phase due to inhomogeneous spins $\boldsymbol{M}(\boldsymbol{r}, H)$. As recognized by Berry [3, 4], a rotation in spin space Figure 5.1 creates a well-defined quantum-mechanical phase γ in the wave function $e^{i\gamma}\psi$. A nonzero Berry phase corresponds to a nonzero triple product:

$$\chi_c = \boldsymbol{S}_1 \cdot (\boldsymbol{S}_2 \times \boldsymbol{S}_3), \tag{1}$$

also called spin chirality [1,2], where $\boldsymbol{S} = \boldsymbol{M}/|\boldsymbol{M}|$ and $\boldsymbol{S}_i = \boldsymbol{S}(\boldsymbol{R}_i)$ describes the atomic spins that cause the conduction electrons to develop their Berry phase [2].

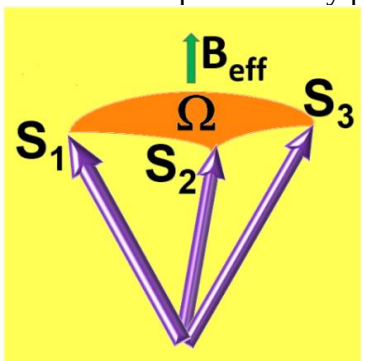

Figure 5.1. Emergent magnetic field due to noncoplanar spins in a nanostructure [1, 2].

When the three vectors are symmetrically arranged and form an angle Θ with the symmetry axis, gives rise to finite spin chirality χ_c.

Conduction electrons moving through and interacting with localized spins $\boldsymbol{s}(\boldsymbol{r})$ acquire a Berry phase through adiabatic rotation so that $\boldsymbol{S}_1$, $\boldsymbol{S}_2$, and $\boldsymbol{S}_3$ can be interpreted as time-ordered sequences $t_1 < t_2 < t_3$. To have a nonzero Berry-phase effect, the spin $\boldsymbol{S}_i = \boldsymbol{S}(\boldsymbol{R}_i)$ must be noncoplanar on the trajectory $\boldsymbol{R}_i \rightarrow \boldsymbol{R}_j \rightarrow \boldsymbol{R}_k$, that is, the so-called spin chirality $\chi_c = \boldsymbol{S}_i \cdot (\boldsymbol{S}_j \times \boldsymbol{S}_k)$ must be nonzero. For example, if the spin direction remains *coplanar*, then $\chi_c = 0$ in Fig. 5.1. When this spin structure is not only noncollinear but also noncoplanar then the triple product is nonzero and the conduction electrons develop a Berry phase. The kinetic energy of the conduction electron is proportional to $(1/2m)\ \hbar^2 \nabla^2$, and applied to $e^{i\gamma}\psi$, the ∇^2 operator yields an additional term proportional to $\nabla\gamma$. This term has the form of a magnetic vector potential and gives rise to an emergent magnetic field that contributes, for example, to the anomalous Hall effect [4]. This contribution is commonly referred to as the *topological Hall effect* (THE). The emergent magnetic field is proportional to the triple product $\chi_c = \boldsymbol{S}_i \cdot (\boldsymbol{S}_j \times \boldsymbol{S}_k)$, whose continuum is called skyrmion density,

$$\Phi = \frac{1}{4\pi}\, \boldsymbol{S} \cdot \left(\frac{\partial \boldsymbol{S}}{\partial x} \times \frac{\partial \boldsymbol{S}}{\partial y} \right). \tag{2}$$

The skyrmion density is nonzero for spins $\boldsymbol{S}(\boldsymbol{r})$ that are both noncollinear and noncoplanar, and Eq. (2) is actually a continuum version of the triple product or spin chirality $\chi_c = \boldsymbol{S}_i \cdot (\boldsymbol{S}_j \times \boldsymbol{S}_k)$. Using S(r + dr) = S(r) + dr·∇s to convert the 'spin chirality' $\chi_c = \boldsymbol{S}_i \cdot (\boldsymbol{S}_j \times \boldsymbol{S}_k)$ into a continuum form yields equations of the type (Eq. 2) and provides a link between Berry phase and skyrmion density. The integral $\int \Phi\, dx dy$ is equal to the emergent magnetic flux (skyrmion number) Q measured in units of the flux quantum h/e (topological Hall effect). The quantity Φ is known as the *skyrmion density* [8, 26], but it

is important to keep in mind that Φ is generally different from the number of skyrmions per unit area. The THE is obtained by areal integration $Q = \int \Phi \, \mathrm{d}x \, \mathrm{d}y$, and this integral is quantized (Q = ±1) for skyrmions but not for other skyrmionic spin structures [5] that may be termed partial skyrmions or 'paraskyrmions'. The equation for Φ means that the THE is a functional of the local magnetization $\boldsymbol{M}(\boldsymbol{r})$, that is, the THE is determined by the local magnetization and its gradient, which is strongly influenced by the exchange and DM interactions.

In this chapter the THE effect contribution due to finite spin chirality triple product $\chi_c = \boldsymbol{S}_i \cdot (\boldsymbol{S}_j \times \boldsymbol{S}_k)$ will be discussed [1, 2]. Since these chiral spin textures appear in the system which shows inhomogeneity in $\boldsymbol{M}(\boldsymbol{r}, H)$, therefore the magnetic nanoclusters of B-20 CoSi, nanocomposite of the hard and soft magnet of MnBi: FeCo and Antiferromagnetic Ru_2MnSn-based Heusler compounds with non-collinear and non-coplanar spin texture shows significant topological Hall effect.

5.2 Peripheral Chiral Spin Textures and Topological Hall Effect in Exchanged Coupled CoSi Nanoparticles

B-20 compounds such as $T_{50}X_{50}$ (T = Fe, Co, Mn and X = Ge, Si) are promising spintronics materials, because their noncentrosymmetric and chiral crystal structure leads to scalar DM interactions, which create spin spirals with well-defined helicity in the bulk [5,6,7,8] and skyrmions in homogeneous thin films. Nano-structuring can be used to achieve room-temperature skyrmions with sizes of about 17 nm through exchange engineering in a B-20type bulk $Co_{1.043}Si_{.0957}$ [8]. The skyrmion density Φ can be enhanced by exploiting the scalar DM interaction in B-20 CoSi [7, 8].

5.2.1 Magnetism in CoSi Nanoparticles

To understand the nanocluster magnetism, the density-functional-theory (DFT) calculations for the CoSi nanoparticle were performed, which has 286 atoms [7]. The DFT calculations shows that the calculated spin polarization, that is, the difference between the local ↑ and ↓ densities of states, is virtually zero in the cluster core, whereas the nanocluster surface exhibits a large magnetic magnetization of m′ = 0.88 μB per Co atom [7]. The calculated average magnetic moments for the core is 0.02 μB/Co. The schematic of the nanoparticle shown in Fig. 5.2 represents the spin configuration of a thin film of CoSi nanoparticles. The yellow region represents the zero magnetization in the core and the large magnetization at the surface coupled nanomagnets.

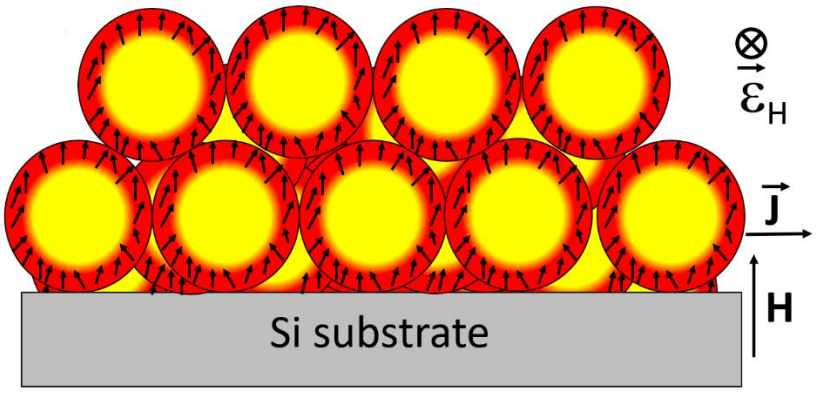

Figure 5.2. Spin structure of CoSi: schematic nanoscale geometry and spin structure, where **H**, **J**, and **ε** correspond to applied magnetic field, current density, and Hall emf, respectively. The spin textures are non-collinear and non-coplanar due to DM interactions.

5.2.2 Topological Hall Effect in CoSi Nanomagnets

To determine the THE due to non-coplanar and non collinear spin textures in CoSi, the Hall resistivity equation is used [5,6].

$$\rho_{yx} = R_0 H + R_s M + \rho_{THE} \quad (3)$$

Here ρ_{yx} is the measured Hall resistivity, R_0H is the ordinary Hall effect, R_sM is the conventional contribution to the anomalous Hall effect, and ρ_{THE} is the Berry-phase contribution to the anomalous Hall effect, or simply the topological Hall effect. When the magnetization approaches saturation, R_sM_s becomes a constant, R_0 and R_s can be determined by plotting ρ_{yx}/H *vs.* M/H in the high-field region (20-50 kOe), and $R_0 H + R_s M$ can then be subtracted from ρ_{yx} to yield ρ_{THE} [7]. The THE of CoSi nanoclusters film for different temperatures and in magnetic fields of up to 50 kOe, were applied perpendicular to the film plane. Figure 5.3 shows a ρ_{THE} (experimental) typical THE analysis, namely at 320 K, The details related to field and temperature dependence of the corresponding THE is shown in Ref. [7].

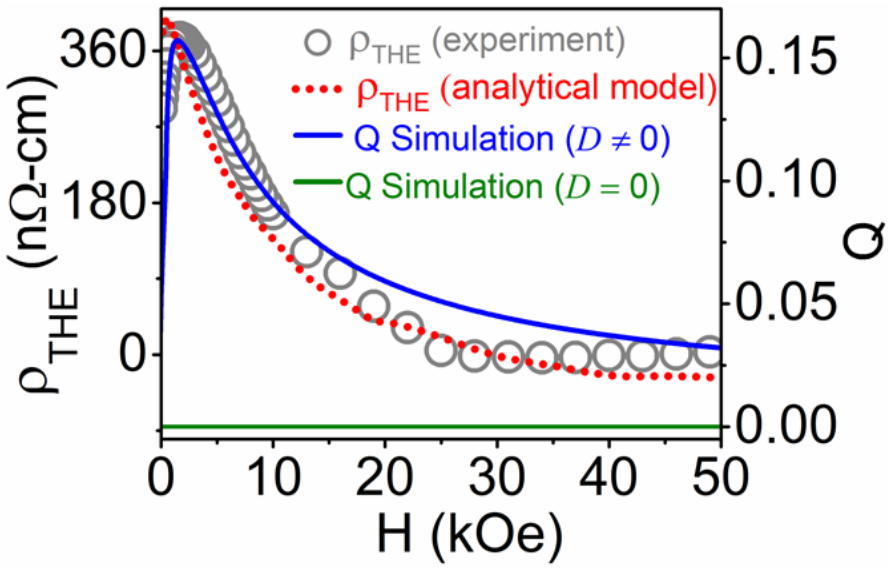

Figure 5.3. Hall resistivity and dc susceptibility of the CoSi nanocluster film: THE ρ_{THE} (experimental) analysis at 320 K, (comparison of experimental and theoretical field dependences of the THE and skyrmion number (Q).

5.2.3 Analytical Model for the Study of Topological Hall effect in CoSi Nanocluster Film

Figure 5.3 compares the experimental THE measured at 10 K (open circle) with theoretical calculations. The dotted red curve in Fig. 5.3 has been obtained by solving an analytical model yielding $\chi_{TP} = \boldsymbol{M}_1 \cdot (\boldsymbol{M}_2 \times \boldsymbol{M}_3)$. The calculation assumes three spins forming an angle θ with the film plane, Fig. 5.1. The spins are subjected to an easy-plane uniaxial anisotropy of magnetostatic origin, which tries to keep the magnetizations in the film plane ($\theta = 90^o$). For such a configuration, the response to an external field is well known, name a straight line $M_z = M_s \cos\theta \sim H$. The evaluation of the corresponding triple product is straightforward and yields

$$\chi_c = 3\sqrt{3}/2\, M_s^3\, f(\theta), \tag{4}$$

where $f(\theta) = \cos\theta \sin^2\theta$. In terms of the normalized magnetization $m = M_z/M_s$, we obtain $f(m) = m\,(1 - m^2)$, which is the dotted red curve in Fig. 5.3.

5.2.4 Micromagnetic Simulations

While transport properties, analytical results Fig. 5.3 are an indication of THE, a proof requires analysis of $\boldsymbol{M}(\boldsymbol{r})$ and $\Phi(\boldsymbol{r})$. To obtain explicit information, we have used MuMax3 and carried out micromagnetic simulations using experimental parameters. For these simulations, the clusters, which touch each other, similar to those in the experimental sample were considered. The cluster has a size of 11.6 nm and is considered to have a spin-polarized shell of thickness of about 2 nm and a non-magnetic core. The magnetic shell was divided into a cell size of 0.25nm during the simulations. We have used K_1 value measured at 10 K is 1.25 Merg/cm^3 (or 0.125 MJ/m^3), M_s = 102 emu/cm^3, A_{ex} = 0.0838 μerg/cm (or 0.838 pJ/m). and D is detrmined to be 0.72 ergs/cm^2

(or 0.72 mJ/m^2) at 10 K. Figures 5.4 shows the spin structure obtained in our simulations. Without loss of generality, the figure is limited to three nanoclusters in contact with each other.

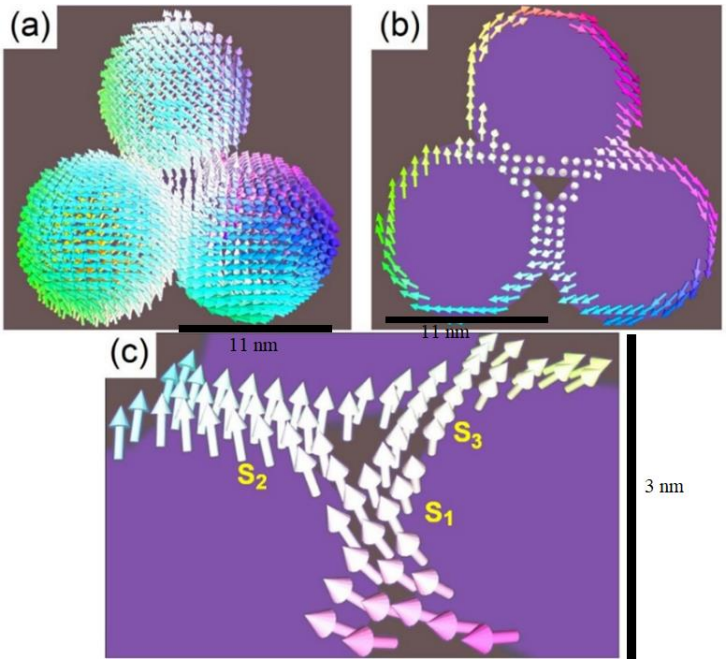

Figure. 5.4. Simulated spin structures in CoSi nanoclusters: (a) three-dimensional view on magnetic shell, (b) Two-dimensional cross-section view on the equator plane, and (c) spin structure in the vicinity of the contact points (c). In this figure, the field was taken as 1.6 kOe, roughly corresponding to the THE maximum, and a nonzero *D* has been used, as appropriate for B20 materials. Note the poles of the spin structures in (a), which are distantly related to bobbers.

We have also investigated many-cluster systems, where the spin structure is very similar to Fig. 5.4 but difficult to visualize. The subfigures show the spin distribution in the magnetic shell (a), the corresponding equatorial cross-section view (b), and the spin structure in the vicinity of the contact points (c). The three spins $\mathbf{S}_1$, $\mathbf{S}_2$ and $\mathbf{S}_3$ are clearly noncoplanar and forms chiral spin textures (similar to Fig. 5.1), causing the conduction electrons to accumulate a Berry phase and to contribute to the Hall effect. The presence of B20-type scalar DM interactions (*D*) is essential for the formation of the noncoplanar

spin structure in the present sample (blue curve in Fig. 5.3); By choosing $D = 0$, the simulations cause the THE to collapse (green line in Fig. 5.3). Note that magnetocrystalline anisotropy of the CoSi clusters is small and does not affect the spin structures according to our simulations.

The total THE contribution corresponds to $Q \approx 0.15$ per nanocluster, as estimated by numerical integration over Φ. Along the surface and through the contact points, the feature or 'paraskyrmion' size, deduced from the magnetization gradient in Φ, is of the order of 10 nm. Figure 5.4(c) visualizes the filigree nature of the CoSi paraskyrmions. Note that both intra- and inter-cluster exchange interactions are involved in the nanoscale confinement of $\boldsymbol{M}(\boldsymbol{r})$ and $\Phi(\mathbf{r})$.

Above-outlined experimental and theoretical findings prove the existence of paraskyrmions (tilted spin textures) in CoSi nanocluster films. While the spin structure of Fig. 5.4 unambiguously yields THE signatures such as those in Fig. 5.3, there may be other contributions. One mechanism is thermal spin-chirality fluctuations, which exist, for example, in thin films with perpendicular magnetic anisotropy. The chiral spin fluctuations may cause or contribute to sign changes in the Hall effect [9-11], a feature we also see in our data THE above 210 K, Fig. 5.3. In terms of Fig. 5.4(c), these fluctuations would correspond to a thermally activated noncoplanarity of the spins. However, they are limited to the vicinity of T_c [9-11], while our CoSi nanocluster film exhibits a THE down to 10 K, far below T_c Ref. [7]. In addition, the nanocluster film also exhibits a metal to semiconductor-like transition in the longitudinal resistivity data. Therefore, a comprehensive explanation of the temperature-dependence of the Hall

transport in core-shell structures close to the Stoner transition (and generally in B20 magnets) is a major challenge to future research.

5.3 Interfacial Magnetic Vortex Formation in Exchange-Coupled Hard-Soft Magnetic Bilayers

The out-of-plane magnetization reversal process of the exchange-coupled MnBi:CoFe bilayers structure Fig. 5.5(a) involves formation of a curling-type twisting of the magnetization in the film plane at low or intermediate reversal fields [12,13]. The PNR experiments [12,13] have shown that an applied magnetic field causes the magnetization to continuously rotate from out-of-plane in the MnBi layer to in-plane in the CoFe layer. The reversal involves a curling-type twisting of the magnetization in the film plane. This curling is reminiscent of chiral spin structures establishes a new type of skyrmionic spin structure. Perpendicularly exchange-coupled MnBi: FeCo thin films, where MnBi is the hard phase and FeCo is the soft phase, are suitable for this purpose. The configurations such as the MnBi/CoFe two-phase system of Fig. 5.5(a), which are investigated by room-temperature X-ray magnetic circular dichroism (XMCD) and polarized neutron reflectometry (PNR) and by micromagnetic simulations [12,13].

MnBi shows a high coercive field of 2 T at 450K, and the magnetic anisotropy increases from 1.2MJ m^{-3} to 2.4 MJ m^{-3} as the temperature rises from 300K to 450K [14]. The simulation for three cases were performed. All these cases are done for different values of magnetic anisotropy which depends on temperature.

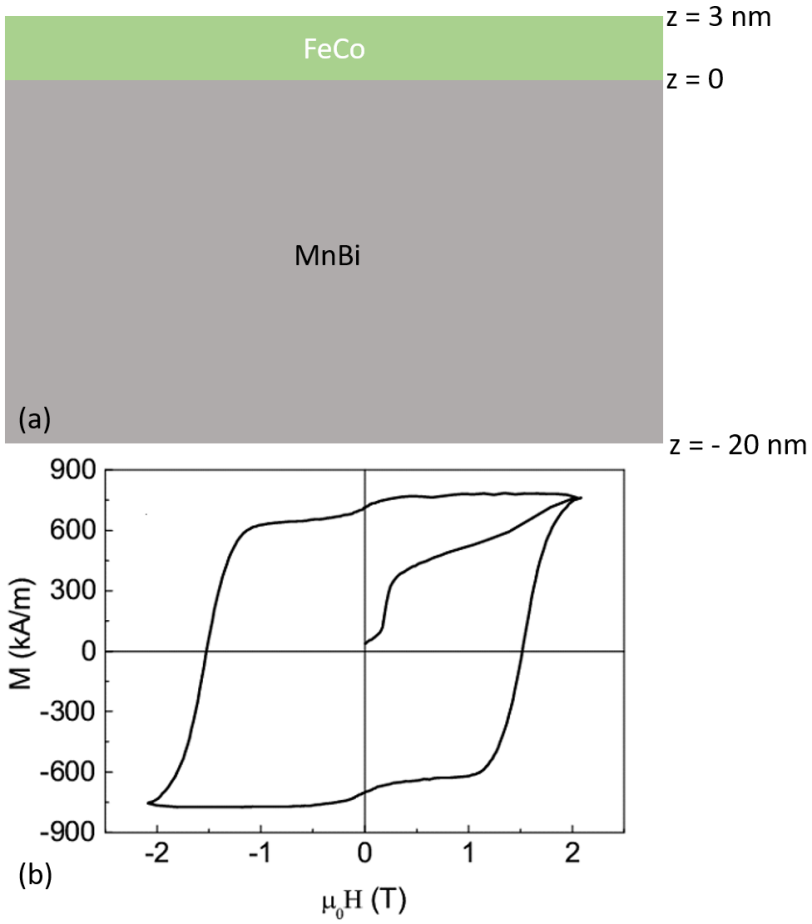

Figure 5.5. (a) MnBi: FeCo bilayer schematic with interface mentioned at z = 0 where both layers are exchange coupled (b) Typical hysteresis loop of a MnBi (20 nm)/FeCo(3 nm) bilayer structure at room temperature. The figure is taken from reference [12,13].

5.3.1 Case 1: K_1=0.9MJ/m^3 in MnBi

For case 1 relatively small value of magnetic anisotropy in MnBi. The simulations parameters for saturation magnetization M_s, exchange stiffness A, and uniaxial anisotropy constant K_1 are: M_s = 0.58 MA m^{-1} (0.73 T), A = 8 pJ m^{-1}, K_1 = 0.9 MJ m^{-3} (hard MnBi phase) [12,13] and M_s = 1.91 MA m^{-1} (2.4 T), A = 10 pJ m^{-1} , K_1 = 0 (soft FeCo phase) [12,13]. The results of simulations are shown below in Fig. 5.6. The cell size

considered is $2 \times 2 \times 1nm^3$. All these values are less than exchange length. The interlayer exchange interaction between MnBi and FeCo is considered as 9 pJ m^{-1}.

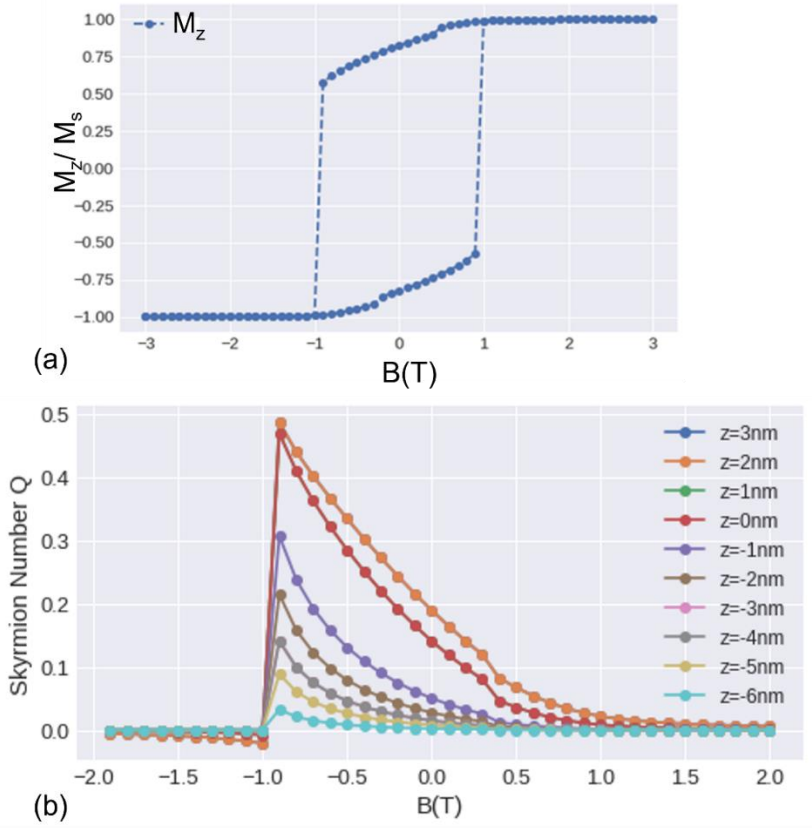

Figure 5.6. (a) Hysterics for the case 1 at low temperature showing low H_c. (b)Layer dependent skyrmion number for case 1 (Low magnetic anisotropy in MnBi). At low temperature the curling mode penetrate deep inside MnBi because of the low anisotropy.

5.3.2 Case 2: K_1=1.2MJ/m^3 in MnBi

Now since the experiment in Fig. 5.5(b) in Ref. [12,13], was done at room temperature. So the simulation for the value of K_1 for MnBi at room temperature are performed and found that coercive field H_c increases and similar to experimentally measured values.

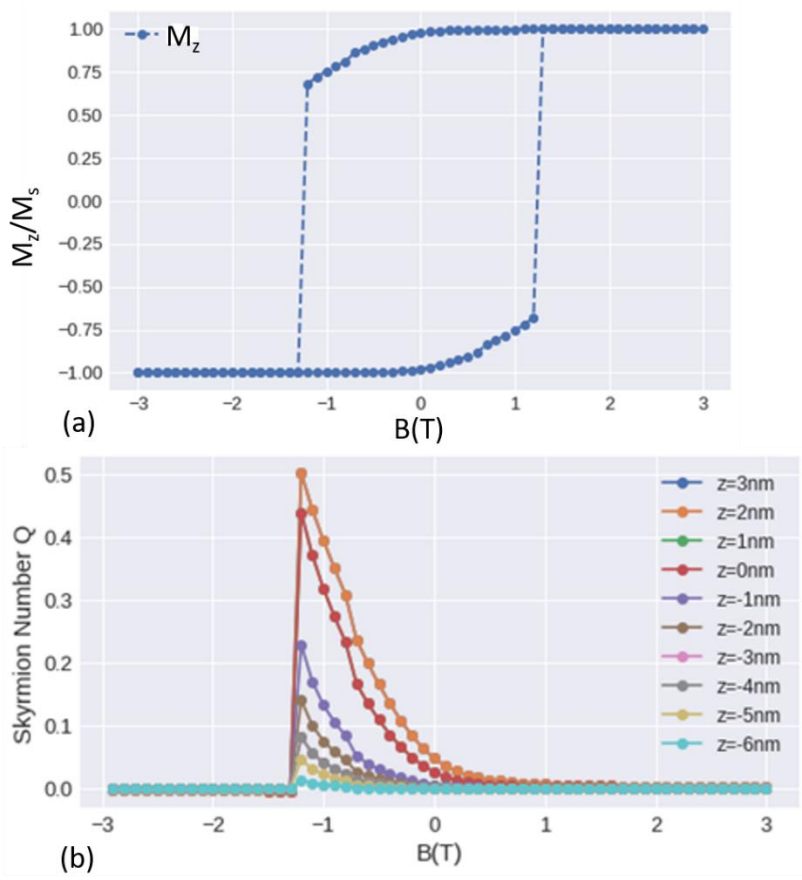

Figure 5.7. (a) Hysterics for case 2 at room temperature showed moderate H_c. (b) Layer-dependent skyrmion number for case 2 (moderately high magnetic anisotropy in MnBi). At room temperature, the curling mode penetration inside MnBi slightly decreases as compared to low temperature because of the slight increase in anisotropy.

5.3.3 Case 3: K_1=2.4MJ/m^3 in MnBi

For 3rd case, at high temperature, the magnetic anisotropy is 2.4MJ/m^3. One can clearly expect an increase in the coercive field as shown in Fig. 5.8. Since its very high temperature and high K_1 so one can expect a very low penetration depth of curling mode in MnBi i.e. spins in MnBi will prefer to align in the direction of anisotropy.

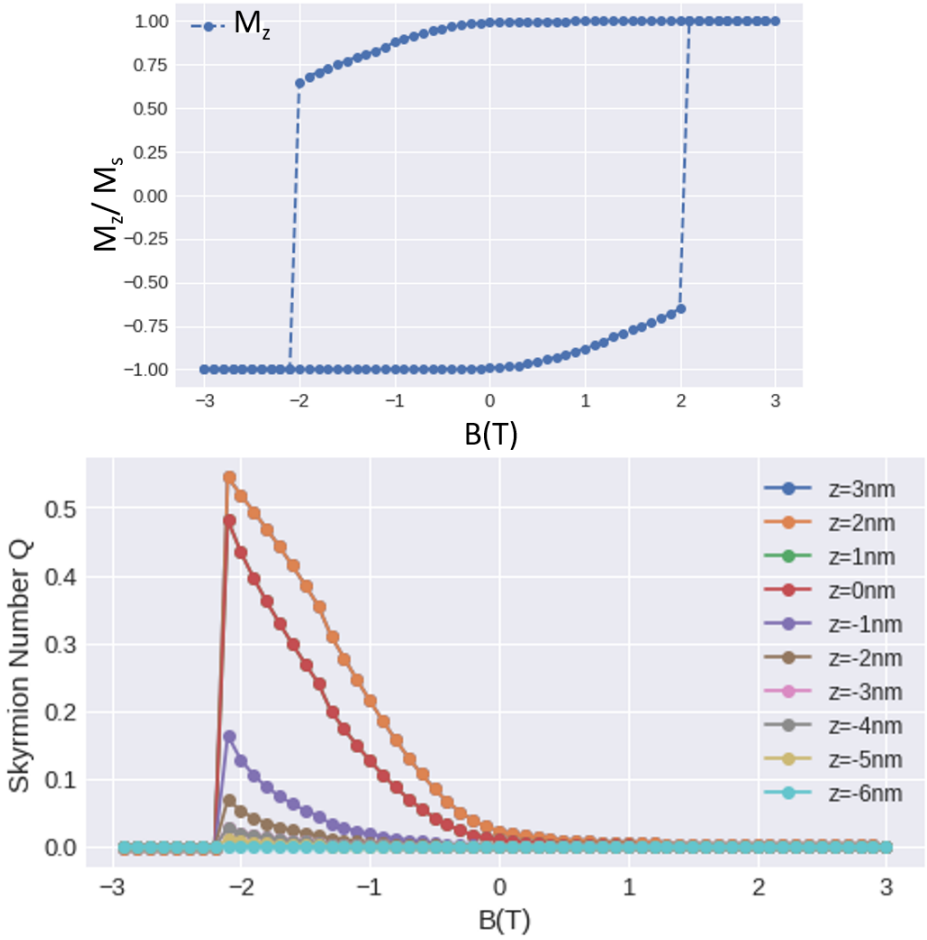

Figure 5.8. (a) Hysterics for case 3 at high temperature showing large H_c. (b) Layer-dependent skyrmion number for case 3 (high magnetic anisotropy in MnBi). At high temperature, the curling mode penetration inside MnBi decreases significantly because of the slight increase in anisotropy.

5.3.4 Discussion

The curling mode $\boldsymbol{M} = M_s(z, \rho)\,(\cos\phi\,\mathbf{e}_y - \sin\phi\,\mathbf{e}_x)$ originates from the competition between exchange energy and magnetostatic self-interaction interaction [15, 16, 17, 18, 19]. The former favors coherent rotation, and the latter favors the partial flux closure inherent in the curling mode but costs exchange energy. Since exact solutions are available for simple systems only, it is convenient to use micromagnetic simulations. Figures 5.6(b), 5.7(b), 5.8(b), and 5.9, shows the curling-type spin structure for a MnBi

(20 nm)/FeCo(3 nm) thin-film patch, obtained using micromagnetic simulations. The field is perpendicular to the film, and the spin-configuration snapshot $\boldsymbol{M}(\boldsymbol{r}, H_z)$ has been made close to coercivity.

Figures 5.6(b), 5.7(b), 5.8(b) and 5.9 confirm shows in-plane (or *x*-*y*) magnetization components. The figure also shows that the spin structure is of the interfacial magnetic vortex. The curling intensity decays exponentially in the hard phase as shown in Fig. 5.9 and by calculation of width-dependent skyrmion number calculations in Figures 5.6(b), 5.7(b), 5.8(b). The decay length of soft-into-hard penetration is generally of the order of $\delta_0 = \sqrt{K_1/A}$ [19], that is, about 3 nm for MnBi.

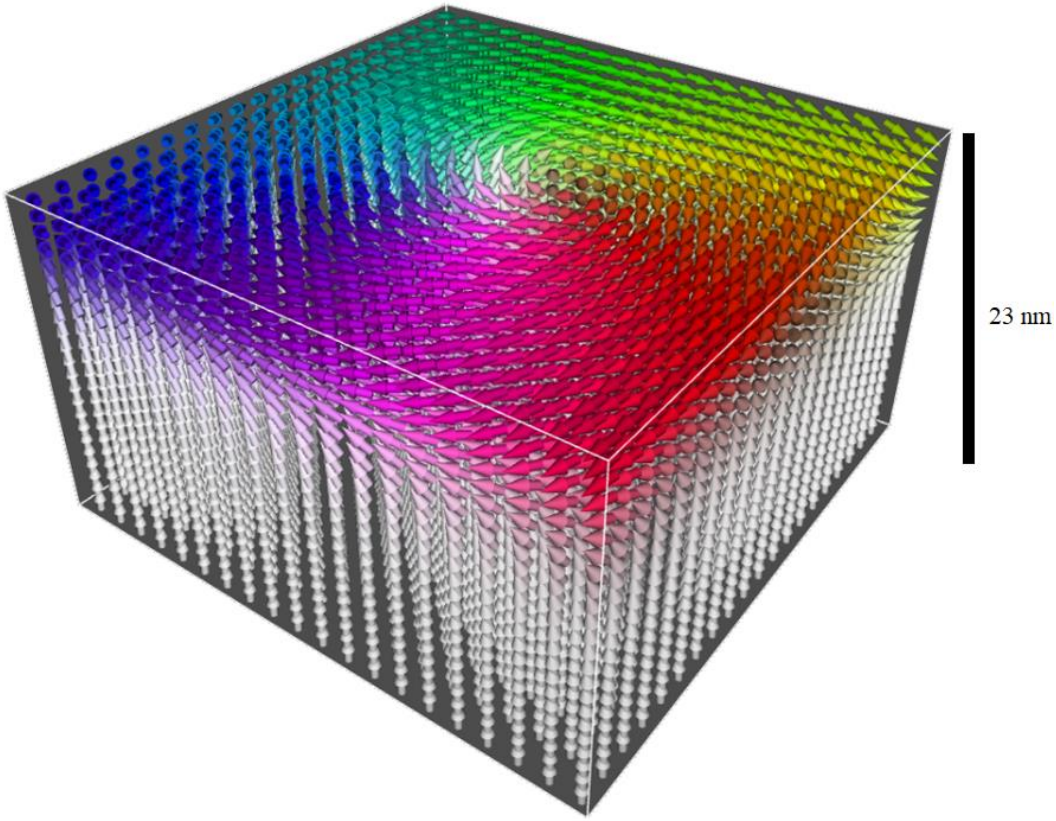

Figure 5.9. Magnetization curling in MnBi(20 nm)/FeCo(3 nm).

The topological charge Q reflects the skyrmion-like noncollinearity of the spin structure and is obtained by integration over the skyrmion density: $\Phi = \boldsymbol{M}\cdot(\partial\boldsymbol{M}/\partial x \;\; \partial\boldsymbol{M}/\partial y)/4\pi M_s^3$ [6]. The charge is field-dependent and reaches a sharp maximum near coercivity, where the noncollinearities are most pronounced Figures 5.6(b), 5.7(b), 5.8(b). In very high fields, $Q = 0$, because all spins are parallel and $\Phi = 0$. The spin texture are not limited to low temperatures, due to the high T_c values of MnBi and FeCo.

5.4 Chiral Spin Texture and Topological Hall Effect in Antiferromagnetic Materials

Antiferromagnets can host non-collinear spin structures and a Néel temperature T_N above room temperature [20]. A noncoplanar spin structure can give rise to topological Hall effect contribution in the room-temperature Hall resistivity data, which is realized in antiferromagnets like $Ru_2Mn_{0.8}Sn_{1.2}$. Strong topological Hall effect in the $Ru_2Mn_{0.8}Sn_{1.2}$ alloy physically originates from a noncoplanar antiferromagnetic scissor mode, which creates a small net magnetization in a magnetic field and subsequently yields a Berry curvature [21].

Figure 5.10 show the field dependence of the Hall resistivity $\rho_{xy}(B_0)$ at 300 K (open squares) with $B_0 = H$ in kG (cgs) or $\mu_0 H$ in T (SI) is an external magnetic field in antiferromagnets like $Ru_2Mn_{0.8}Sn_{1.2}$. The Hall resistivity is often expressed as $\rho_{xy} = \rho_{OH} + \rho_{AH} + \rho_{THE,}$ where $\rho_{OH} = R_0 B_0$, $\rho_{AH} = 4\pi M R_s$, and ρ_{THE} are the ordinary, anomalous and topological Hall-effect contributions, respectively. In these equations, R_0 is the ordinary Hall coefficient and R_s is the anomalous one.

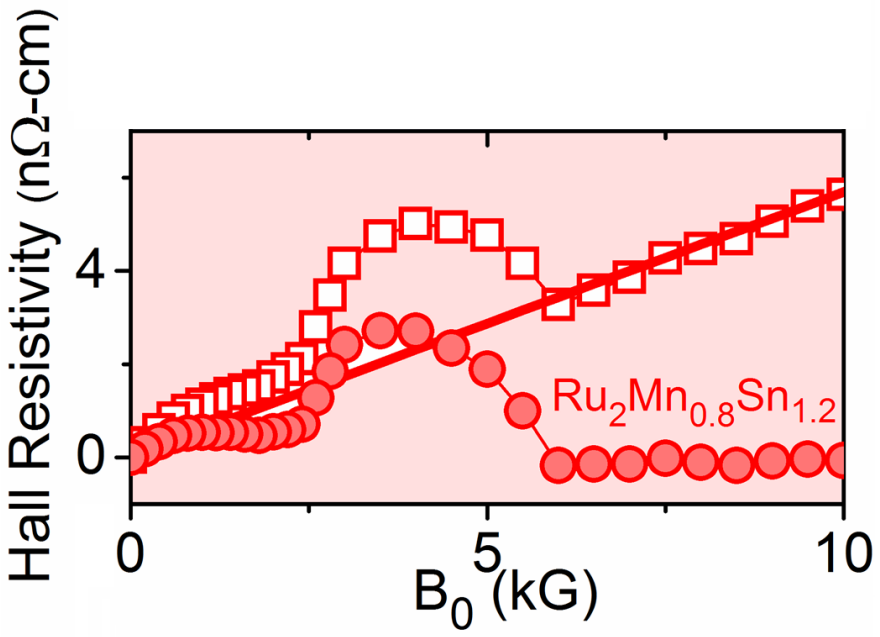

Fig. 5.10. Hall effect at 300 K: field dependences of the Hall resistivity ρ_{xy} (open squares) and of the topological Hall effect (filled circles) as a function of external magnetic field $B_0 = H$ in kG (cgs) or $\mu_0 H$ in T (SI). The solid curves are the Hall resistivity without the topological Hall-effect term. The figure is taken from reference [21].

Following the standard procedure from the literature [6], R_o and R_s have been determined from the high-field $\rho_{xy}(B_0)$ data and used to extract the THE contribution $\rho_{THE} = \rho_{xy} - \rho_{OH} - \rho_{AH}$ (filled circles in Fig. 5.10). The bumps in the Hall-effect and THE curves are characteristic of the topological Hall effect caused by the Berry curvature. This curvature is realized in noncoplanar spin structures, which are common in skyrmionic thin films [6]. Pictorially, conduction electrons (or holes) change their spin direction due to the exchange interaction with the lattice spins, and the corresponding spin rotation translates into a Berry curvature and into an emergent magnetic field that contributes to the Hall effect.

The $Ru_2Mn_{0.8}Sn_{1.2}$ sample exhibits a particularly big THE (red curve in Fig. 5.10), which requires a physical explanation. The topological Hall effect in ordinary

antiferromagnets is expected to be virtually zero, as is the case for antiferomagnetic Ru_2MnSn [21]. It is well-known that certain noncoplanar atomic-scale noncollinearities give rise to a substantial THE in the absence of a magnetic field, but there is no evidence for such spin configurations in the present system, and the zero-field THE is zero. In other words, a small external magnetic field of about 5 kG [0.5 T] is sufficient to create a substantial THE, which cannot be explained as an atomic phenomenon involving the electronic structure.

The explanation for THE in antiferromagnetic $Ru_2Mn_{0.8}Sn_{1.2}$ involves scissor mode (or canted spin textures), which is schematically shown in Fig. 5.11(b). The propeller mode of Fig. 5.11(a), which amounts to a rotation of the Néel vector $\boldsymbol{N} = \boldsymbol{M}_A - \boldsymbol{M}_B$, is easy to create, for example by the random anisotropy associated with the polycrystallinity of the samples. Conduction electrons of a given spin interact differently with the ↑ (blue) and ↓ (red) spins of the propeller mode, which gives rise to a substantial *spin* Hall effect [4], but the net spin polarization of an antiferromagnet is zero, so that the propeller mode does not contribute to the THE.

The scissor mode, explained in Fig. 5.11(b), is well-known to exist in antiferromagnets and creates a small net magnetization $\boldsymbol{M} = \boldsymbol{M}_A + \boldsymbol{M}_B$, as schematically shown in Fig. 5.11(c). Any spatial variation of this mode yields a Berry curvature similar to that created by ferromagnets. The corresponding integral Berry curvature or 'topological Hall effect' is of the well-known type [6]

$$Q = \frac{1}{4\pi}\int \boldsymbol{M}\cdot\left(\frac{\partial \boldsymbol{M}}{\partial x}\times\frac{\partial \boldsymbol{M}}{\partial y}\right) dV. \qquad (5)$$

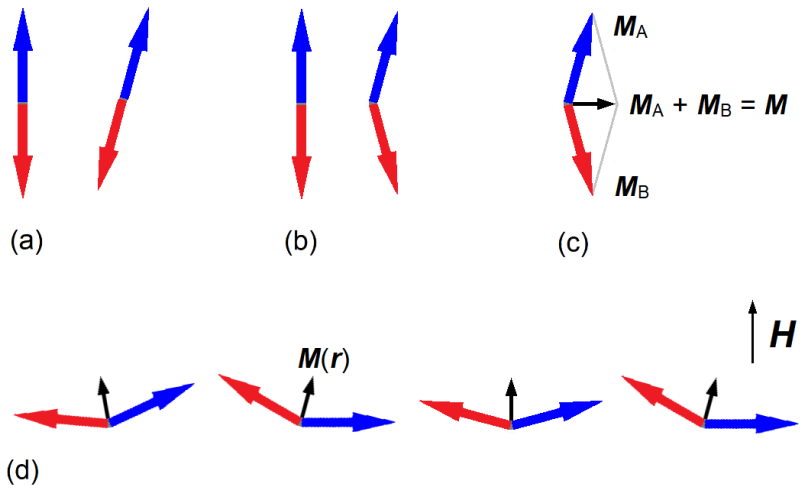

Figure 5.11. Antiferromagnetic (AFM) magnetization modes: (a) propeller mode, (b) scissor mode, (c) net magnetization, and (d) schematic situation in a random-anisotropy antiferromagnets subjected to a magnetic field. The field $\boldsymbol{H}$ is perpendicular to the film plane and the angle between $\boldsymbol{H}$ and $\boldsymbol{M}$ is θ. The noncoplanarity of $\boldsymbol{M}(\mathbf{r})$, which gives rise to the THE, means that the scissor configurations shown in this figure are not confined to the paper plane but that $\boldsymbol{M}(\boldsymbol{r})$ has also a component perpendicular to the paper plane (not shown in the figure).

The question is why the THE is big in the Sn-rich alloy but small in the stoichiometric alloy, both being antiferromagnets. The answer is provided by the magnitude of the net magnetization, $|\boldsymbol{M}| \ll M_s$, where $M_s = |\boldsymbol{M}_A| = |\boldsymbol{M}_B|$ is the sublattice magnetization. The magnitude scales as $\mu_o\mu_B H/\mathcal{J}^*$, where $\mathcal{J}^* = |\mathcal{J}_{AB}|$ is the antiferromagnetic intersublattice exchange. Exchange fields ($\mathcal{J}^*/\mu_B$) are typically of the order of several 100 T and therefore much higher than typical applied fields, for example $\mu_o H \leq 1$ T ($B_0 = 10$ kG) in Fig. 5.10. As a consequence, the antiferromagnetic THE is expected to be rather small.

We assume that the crystallite or grain size is much larger than $(A/K)^{1/2}$, so that the zero-field spin structure is determined by $\boldsymbol{n}$, which obeys $|\boldsymbol{n}| = 1$. Let us consider the quasiclassical model Hamiltonian

$$\mathcal{H} = -\mu_o \boldsymbol{M}_A \cdot \boldsymbol{H} - \mu_o \boldsymbol{M}_B \cdot \boldsymbol{H} - \frac{K}{M_s^2}[(\boldsymbol{M}_A \cdot \boldsymbol{n})^2 + (\boldsymbol{M}_B \cdot \boldsymbol{n})^2] + \mathcal{J}^* \boldsymbol{M}_A \cdot \boldsymbol{M}_B \qquad (6)$$

Since $\boldsymbol{M}_A = ½(\boldsymbol{M} + \boldsymbol{N})$ and $\boldsymbol{M}_B = ½(\boldsymbol{M} - \boldsymbol{N})$ yield $\boldsymbol{M}_A \cdot \boldsymbol{M}_B = ½\boldsymbol{M}^2 - M_s^2$ and

$$M^2 + N^2 = 4 M_s^2 \qquad (7)$$

Eq. (6) simplifies to

$$\mathcal{H} = -\mu_o \boldsymbol{M} \cdot \boldsymbol{H} - \frac{K}{2M_s^2}[(\boldsymbol{M} \cdot \boldsymbol{n})^2 + (\boldsymbol{N} \cdot \boldsymbol{n})^2] + ½\mathcal{J}^* (M^2 - 2M_s^2) \qquad (8)$$

Let us apply a field in the *z*-direction and consider a grain or crystallite with arbitrary easy-axis direction **n**. By rotating the coordinate frame in the *x*-*y* plane (rotation angle ψ), we can move the easy axis into the *x*-*z*-plane, or paper plane in Fig. 5.11. The easy-axis vector is then $\boldsymbol{n} = \cos\chi\, \boldsymbol{e}_z + \sin\chi\, \boldsymbol{e}_x$, where χ is the angle between easy axis and film normal. This means that the net magnetization is also in the *x*-*z*-plane, $\boldsymbol{M} = M(\sin\theta\, \boldsymbol{e}_x + \cos\theta\, \boldsymbol{e}_z)$ and that the Néel vector, which is perpendicular to $\boldsymbol{M}$, obeys $\boldsymbol{N} = N(\cos\theta\, \boldsymbol{e}_x - \sin\theta\, \boldsymbol{e}_z)$.

Equation (8) contains two independent variables, and it is convenient to choose the magnitude M and the angle θ of the net magnetization; the length N of the Néel vector is not independent but implicitly given by Eq. (7). Equation (8) then becomes

$$\mathcal{H} = -\mu_o H M \cos\theta + K\cos(2\theta - 2\chi) + \mathcal{J}^* M^2 \qquad (9)$$

where we have ignored a physical unimportant zero-point energy and taken into account that $M \ll M_s$

Minimization of Eq. (8) with respect to M and θ yields the magnitude of the net magnetization

$$M = \frac{\mu_o \mu_B H}{\mathcal{J}^*}\cos(\theta) \qquad (10)$$

and the nonlinear equation

$$\frac{\mu_o^2 H^2}{4 K \mathcal{J}^*} \sin(2\theta) = \sin(2\theta - 2\chi) \tag{11}$$

This equation has two solutions, namely

$$\theta = -\frac{1}{2} \operatorname{atan}\left(\frac{\sin(2\chi)}{(H/H_{SF})^2 - \cos(2\chi)}\right) \tag{12a}$$

and

$$\theta = \frac{\pi}{2} - \frac{1}{2} \operatorname{atan}\left(\frac{\sin(2\chi)}{(H/H_{SF})^2 - \cos(2\chi)}\right). \tag{12b}$$

Here $H_{SF} = (4K\mathcal{J}^*)^{1/2}/\mu_o$ is the spin-flop field. In term of Fig. 5.11, these transitions amount to rotation of the two spin sublattices by 90º, from (b) to (d). The present scenario, schematically shown in Fig. 5.11(d), is described by Eq. (12a). In the high-field limit, the angle θ is small and obeys

$$\theta(\boldsymbol{r}) = -\frac{H_{SF}^2}{2 H^2} \sin(2\chi(\boldsymbol{r})) \tag{13}$$

By symmetry, θ is zero for $\chi = 0$ (easy axis parallel to external field) and for $\chi = 90^o$ (easy axis perpendicular to external field). The angle θ reaches a maximum at $\chi = 45^o$ and ensemble-averaging over all random easy-axis directions yields $\langle \sin^2(2\chi) \rangle = 8/15$, corresponding to $\langle \theta \rangle = 0.3651\ H_{SF}^2/H^2$. For $\chi = 45^o$, Eq. (12a) simplifies to $\theta = -\frac{1}{2} \operatorname{atan}(H_{SF}^2/H^2)$; this function is shown in Fig. 5.12 (dashed line).

Equation (5) shows that the THE scales as M^3. However, this is not the only consideration. In very high fields, Eq. (13) predicts $\theta \approx 0$ for all easy-axis misalignments, so that all spins are oriented in field direction and the gradients in Eq. (5) vanish. Furthermore, the spins must be not only noncollinear but also noncoplanar. Equation (5) is a continuum version of the requirement to have local magnetizations $\boldsymbol{M}_1$, $\boldsymbol{M}_2$, and $\boldsymbol{M}_3$ so

that $\boldsymbol{M}_1 \cdot (\boldsymbol{M}_2 \times \boldsymbol{M}_3) \neq 0$. Random anisotropy satisfies this requirement because the in-plane rotation angle ψ is different for each grain. The magnetization distribution in the grains is not known, but in fair approximation, we can consider three spins characterized by common values of M and θ while having $\psi_1 = 0^\circ$, $\psi_2 = 120^\circ$, and $\psi_3 = 240^\circ$, respectively. Evaluation of the cross-product shows that the THE is proportional to

$$\boldsymbol{M}_1 \cdot (\boldsymbol{M}_2 \times \boldsymbol{M}_3) = \frac{3\sqrt{3}}{2} M^3 \cos\theta \sin^2\theta \tag{15}$$

where M is given by Eq. (10) and θ by Eq. (12a). The solid line in Fig. 5.12 shows the field dependence of this expression for $\chi = 45^\circ$.

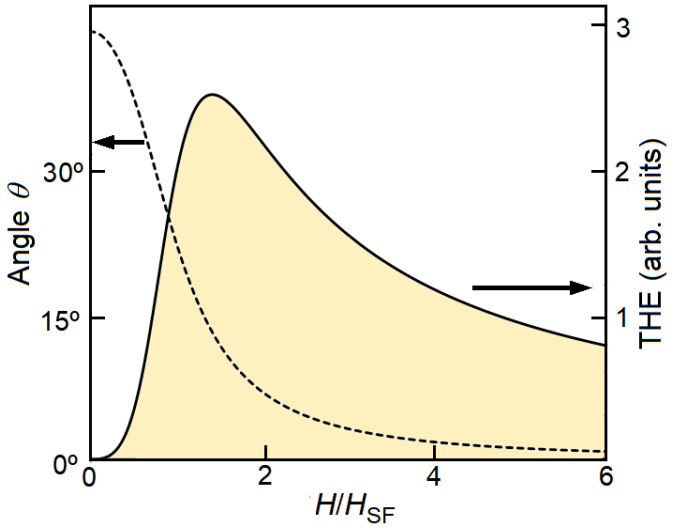

Figure. 5.12. Misalignment angle and topological Hall Effect.

The above model provides a basic explanation of THE but is only semiquantitative. First, the precise spin structure of the sample is largely unknown, except that there is very likely (almost certainly) a spin inhomogeneity of the type shown in Fig. 5.11(d). The THE signal is very clear, especially in $Ru_2Mn_{0.8}Sn_{1.2}$, and explained by a scissor mode. The THE increases with the net magnetization $\boldsymbol{M}(\boldsymbol{r})$, Fig. 5.11(d), and this magnetization is created by the magnetic field.

5.5 Conclusion

In this chapter, the topological Hall effect and Berry phase due to noncollinear and noncoplanar spin texture are discussed. Conventionally it was known that the topological Hall effect usually arises from the skyrmion spin texture with a skyrmion number of Q = 1. But the example in this thesis and this chapter shows that the topological Hall effect can also arise due to spin texture with partial values of Skyrmion number Q. The noncolinear and noncoplanar spin texture in CoSi and antiferromagnetic $Ru_2Mn_{0.8}Sn_{1.2}$ give the topological Hall effect with very large magnitude. Similarly, the interfacial vortex state with a finite skyrmion number can be used for device application at room temperature.

References

[1] Y. Taguchi, Y. Oohara, H. Yoshizawa, N. Nagaosa, and Y. Tokura, Science **291**, 2573 (2001).

[2] W. Wang, M. W. Daniels, Z. Liao, Y. Zhao, J. Wang, G. Koster, G. Rijnders, C.-Z. Chang, D. Xiao, and W. Wu, Nat. Mater. **18**, 1054 (2019).

[3] M. V. Berry, Proc. R. Soc. Lond. A **392**, 45-57 (1984).

[4] D. Xiao, M.-Ch. Chang, and Q. Niu, "Berry phase effects on electronic properties", Rev. Mod. Phys. **82**, 1959 (2010).

[5] N. Nagaosa and Y. Tokura, *Nature Nanotech*. **8**, 899 (2013).

[6] S. Seki and M. Mochizuki, Skyrmions in Magnetic Materials, Springer International, Cham (2016).

[7] R. Pahari, B. Balasubramanian, A. Ullah, P. Manchanda, H. Komuro, R. Streubel, C. Klewe, S. R. Valloppilly, P. Shafer, P. Dev, R. Skomski, and D. J. Sellmyer Phys. Rev. Materials **5**, 124418 (2021).

[8] B. Balasubramanian, P. Manchanda, R. Pahari, Z. Chen, W. Zhang, S. R. Valloppilly, X. Li, A. Sarella, L. Yue, A. Ullah, P. Dev, D. A. Muller, R. Skomski, G. C. Hadjipanayis, and D. J. Sellmyer, Phys. Rev. Lett. **124**, 057201 (2020).

[9] N. Kanazawa, Y. Onose, T. Arima, D. Okuyama, K. Ohoyama, S. Wakimoto, K. Kakurai, S. Ishiwata, and Y. Tokura, Phys. Rev. Lett. **106**, 156603 (2011).

[10] W. Wang, M.W. Daniels, Z. Liao, Y. Zhao, J. Wang, G. Koster, G. Rijinders, C.-Z. Chang, D. Xiao, and W. Wu, Nat. Mater. **18**, 1054 (2019).

[11] Y. Fujishiro, N. Kanazawa, T. Nakajima, X.Z. Yu, K. Ohishi, Y. Kawamura, K. Kakurai, T. Arima, H. Mitamura, A. Miyake, K. Akiba, M. Tokunaga, A. Matsuo, K. Kindo, T. Koretsune, R. Arita, and Y. Tokura, Nat. Commun. **10**, 1059 (2019).

[12] X. H. Zhang, T. R. Gao, L. Fang, S. Fackler, J. A. Borchers, B. J. Kirby, B. B. Maranville, S. E. Lofland, A. T. N'Diaye, E. Arenholz, A. Ullah, J. Cui, R. Skomski, I. Takeuchi J. Magn. Magn. Mater. 560, 169627 (2022).

[13]T. R. Gao, L. Fang, S. Fackler, S. Maruyama, X. H. Zhang, L. L. Wang, T. Rana, P. Manchanda, A. Kashyap, K. Janicka, A. L. Wysocki, A. T. N'Diaye, E. Arenholz, J. A. Borchers, B. J. Kirby, B. B. Maranville, K. W. Sun, M. J. Kramer, V. P. Antropov, D. D. Johnson, R. Skomski, J. Cui, and I. Takeuchi, *Large energy product enhancement in perpendicularly coupled MnBi/CoFe magnetic bilayers*, Phys. Rev. B **94**, 060411(R) (2016).

[14] H. Kronmüller, J. B. Yang and D. Goll, J. Phys.: Condens. Matter **26** 064210 (2014).

[15] W. F. Brown, *Criterion for uniform micromagnetization*, Phys. Rev. **105**, 1479 (1957) and *Virtues and weaknesses of the domain concept*, Rev. Mod. Phys. **17**, 15 (1945).

[16] A. Aharoni, *Introduction to the Theory of Ferromagnetism*, University Press, Oxford 1996.

[17] R. Skomski, P. Manchanda, I. Takeuchi, and J. Cui, *Geometry dependence of magnetization reversal in nanocomposite alloys*, JOM **66**, 1144 (2014).

[18] T. H. Rana, P. Manchanda, B. Balamurugan, A. Kashyap, T. R. Gao, I. Takeuchi, J. Cui, S. Biswas, R. F. Sabirianov, D. J. Sellmyer, *Micromagnetism of MnBi:FeCo thin films*., J. Phys. D: Appl. Phys. **49**, 075003 (2016).

[19] R. Skomski, "Nanomagentics", J. Phys.: Condens. Matter 15, R841 (2003).

[20] Jae Ho Jeon, Hong Ryeol Na, Heeju Kim, Sunghun Lee, Sehwan Song, Jiwoong Kim, Sungkyun Park, Jeong Kim, Hwayong Noh, Gunn Kim, Sahng-Kyoon Jerng*, and Seung-Hyun Chun, ACS Nano, **16**, 8974−8982 (2022).

[21] W. Zhang, B. Balasubramanian, Y. Sun, A. Ullah, R. Skomski, R. Pahari, S. R. Valloppilly, X.-Zh. Li, C.-Zh. Wang, K.-M. Ho, and D. J. Sellmyer, J. Magn. Magn. Mater. **537**, 168104 (2021).